



HAL
open science

Scanning gate investigations of quantum transport phenomena

Hermann Sellier

► **To cite this version:**

Hermann Sellier. Scanning gate investigations of quantum transport phenomena. Mesoscopic Systems and Quantum Hall Effect [cond-mat.mes-hall]. Université Grenoble Alpes, 2021. tel-03276154

HAL Id: tel-03276154

<https://theses.hal.science/tel-03276154v1>

Submitted on 1 Jul 2021

HAL is a multi-disciplinary open access archive for the deposit and dissemination of scientific research documents, whether they are published or not. The documents may come from teaching and research institutions in France or abroad, or from public or private research centers.

L'archive ouverte pluridisciplinaire **HAL**, est destinée au dépôt et à la diffusion de documents scientifiques de niveau recherche, publiés ou non, émanant des établissements d'enseignement et de recherche français ou étrangers, des laboratoires publics ou privés.

Mémoire

Présenté pour obtenir le diplôme d'

HABILITATION À DIRIGER DES RECHERCHES DE L'UNIVERSITÉ GRENOBLE ALPES

Spécialité : Physique

Arrêté ministériel : 23 novembre 1988

Présentée par

Hermann SELLIER

Docteur

préparé au sein de l'**Institut Néel**
dans l'**École Doctorale de Physique**

Scanning gate investigations of quantum transport phenomena

HDR soutenue publiquement le **21 Mai 2021**,
devant le jury composé de :

Sophie GUERON

Directrice de Recherche, LPS, Orsay, Rapportrice

Bruno GRANDIDIER

Directeur de Recherche, IEMN, Lille, Rapporteur

Dietmar WEINMANN

Directeur de Recherche, IPCMS, Strasbourg, Rapporteur

Franck BALESTRO

Professeur, UGA et Institut Néel, Grenoble, Examineur

Claude CHAPELIER

Chercheur, CEA / PHELIQS, Grenoble, Examineur

Christopher BAUERLE

Directeur de Recherche, Institut Néel, Grenoble, Président



Contents

Introduction	5
1 Scanning probes for semiconductor devices	11
1.1 Presentation of Scanning Gate Microscopy	13
1.2 Other scanning probes for 2DEG investigations	18
1.3 Instrumental aspects of SGM	21
2 Local potential change induced by the SGM tip	27
2.1 Screening of the applied potential	28
2.2 SGM tip modeled by a point charge	29
2.3 Potential in the quantum capacitance model	32
2.4 SGM tips with realistic shapes	34
2.5 Amplitude of the energy change in the 2DEG	39
2.6 Numerical simulations of the tip-induced potential	40
3 SGM investigations of InGaAs quantum rings	43
3.1 Device properties	45
3.2 Aharonov-Bohm effect	47
3.3 Local density of state	49
3.4 Coulomb islands in the quantum Hall regime	51
3.5 Mesoscopic Braess paradox	54
3.6 Localization at low charge density	56
4 SGM investigations of GaAs quantum point contacts	59
4.1 Interactions and conductance anomalies in QPCs	61
4.2 Originality of the experimental approach	63
4.3 Overview of the experiments	65
4.4 QPC with patterned interferometers	66
4.5 SGM tuning of a 1D Wigner crystal	68
4.6 Kondo phase shift probed by SGM interferometry	70
4.7 Thermoelectric scanning gate interferometry	72
4.8 Perspectives	74

5	Projects on GaAs devices	75
5.1	Spontaneous charge localization in quantum point contacts	76
5.2	Kondo-cloud extension around quantum dots	81
6	Projects on graphene devices	93
6.1	Electron optics in ballistic graphene	95
6.2	Quantum Hall interferometers in graphene	100
	Bibliography	105

Introduction

This document describes my research activities on quantum transport in electronic devices using a specific experimental technique called Scanning Gate Microscopy (SGM). This technique allows us to obtain spatial information on electron density and electron flow in buried two-dimensional electron gases (2DEG) or to modify these quantities at specific positions in the 2DEG. We use III/V heterostructures, like GaAs/AlGaAs or InGaAs/InAlAs, because their 2DEGs show very high electron mobility. At low temperature, the elastic mean free path is several microns and the electron transport is fully ballistic in the nano-scale devices patterned by electron beam lithography. Since the transport is also phase coherent and the electron wavelength is large, quantum effects can be easily detected in various nanostructures forming constrictions, rings, cavities, etc... These effects are usually probed by transport or optical spectroscopy which give mainly access to the energy levels. The spatial distribution of the quantum states can however not be observed *directly* in these buried nanostructures, as opposed to surface electronic systems where scanning tunneling microscopy (STM) can measure the local density of states. The aim of the SGM technique is to probe *indirectly* this spatial distribution by recording the effect of a local electrostatic perturbation on the transport properties of the nanostructure. The sharp tip of an atomic force microscope (AFM) is used as a local gate which is positioned at any place above the surface. The voltage applied on the tip with respect to the 2DEG induces a local change of the electrostatic potential in the 2DEG which affects the electron states, and modifies the device conductance if these states are involved in the transport through the device. With this technique, the dream would be to image directly the wave function in any kind of nanostructure, but the resolution is unfortunately limited by the relatively large distance between the tip and the 2DEG, which is buried several tens of nanometers below the surface. On the other hand, the SGM technique provides very detailed images of conductance changes, with very small features, because the quantum states are very sensitive to the potential landscape and thus to very small displacements of the tip.

In this document, I will review the various SGM experiments that we have done in our group in Grenoble, and in collaboration with the group in Louvain-la-Neuve in Belgium. I will then present a few research projects that I want to develop in the future. Below, I quickly tell the history of the SGM activity in the group, its origin and its evolution from 2005 to now. I give the name and contribution of the different people involved, explaining the various collaborations around the different projects. I also mention my research work on

the Casimir force from 2005 to 2010, a work which is now stopped and is not presented in the manuscript.

My research activity on Scanning Gate Microscopy

The SGM activity has been initiated in 2005 by Serge Huant at Spectro Lab (University Joseph Fourier, Grenoble) in collaboration with Vincent Bayot (invited researcher from Louvain-la-Neuve). At that time, the team was also composed of Benoît Hackens (post-doc, former PhD student of Vincent Bayot), Frederico Martins (PhD student), Thierry Ouisse (researcher), and Jean-François Motte (engineer). I joined this team as assistant professor at the University of Grenoble in September 2005, a few months after the beginning of the SGM activity. I could quickly participate to this work since my previous research activities were also in the field of quantum transport and mesoscopic physics : during my PhD at the CEA-Grenoble from 1999 to 2002, I studied quantum transport in superconducting junctions with magnetic barriers and in particular the existence of the π -junction [1, 2, 3], and during my postdoc in Delft from 2002 to 2005, I studied quantum transport in etched silicon nanowires and in particular the tunneling through a single dopant atom [4, 5]. This new research topic on quantum nanostructures in semiconductor 2DEGs was therefore in the continuity with my previous works, although extending my knowledge to the physics of 2D electron systems in III/V heterostructures, including ballistic transport and quantum Hall effect. Regarding the SGM technique, I was already familiar with the STM technique that I used during my postdoc to investigate silicon nanostructures, and I could quickly turn to the AFM technique involved in SGM experiments.

In 2005, we did our first SGM experiments on quantum rings to investigate the Aharonov-Bohm effect in the real space. The InGaAs/InAlAs heterostructures were fabricated by Xavier Wallart and Ludovic Desplanque at IEMN in Lille and the devices were patterned by Benoît Hackens using the clean-room in Louvain-la-Neuve. These first SGM experiments were reported in two papers [6, 7] and complemented by numerical simulations [8, 9] done by Marco Pala at IMEP in Grenoble. Based on this work, we also wrote a popularisation article [10], a review article [11], and a book chapter [12].

In 2006, after his postdoc in Grenoble, Benoît Hackens got a position in Louvain-la-Neuve and developed SGM experiments at lower temperature in his laboratory (UCL/IMCN/NAPS). Together with Frederico Martins who also moved there for a postdoc, they did a series of experiments on quantum rings in the quantum Hall regime at very low temperature, which have been reported in three papers [13, 14, 15] co-signed with our group in Grenoble.

In 2007, the team of Serge Huant moved to the CNRS campus to join the new Néel Institute and form the Near-field team together with other colleagues specialists of scanning probe microscopy. When Thierry Ouisse moved to Grenoble-INP in 2008, I became the main contributor to the SGM experiments, but still working in close interaction with Serge Huant. From 2008 to 2011, I supervised the PhD thesis of Peng Liu [16], as co-director, together with Vincent Bayot who hold a part-time research position in Grenoble, funded by the

Nanosciences Foundation. During this period, our SGM activities were funded by the ANR project MICATEC (2008-2010). We characterized new kinds of heterostructures fabricated at IEMN [17]. We investigated different device geometries, in particular asymmetric double-rings, where we demonstrated the existence of a counter-intuitive effect in the electronic transport, called the mesoscopic Braess paradox [18, 19]. The SGM experiments have been first performed in Grenoble, and then continued in Louvain-la-Neuve [20]. We also used the SGM technique to investigate the formation of quantum dots in etched nanowires due to spatial fluctuations in the potential landscape [21].

In 2010, I started a new collaborative project on electron interactions in quantum point contacts (QPC) and was the coordinator of the ANR project ITEM-EXP (2010-2014). This work involves experimental collaborations with Ulf Gennser and Dominique Mailly at LPN in Marcoussis, Marc Sanquer at CEA-INAC in Grenoble, Benoît Hackens and Vincent Bayot in Louvain-la-Neuve. It also involves theoretical collaborations with Jean-Louis-Pichard at CEA-SPEC in Saclay, Dietmar Weinmann and Rodolfo Jalabert at IPCMS in Strasbourg, Pascal Simon at LPS in Orsay, and Bartłomiej Szafran from Krakow in Poland. The GaAs/AlGaAs heterostructures and the QPC devices are fabricated by the LPN. From 2011 to 2014, I supervised the PhD thesis of Boris Brun [22], as co-director, together with Marc Sanquer. Important results on the conductance anomalies in QPCs have been obtained thanks to SGM experiments at very low temperature performed in Louvain-la-Neuve by Boris with the help of Frederico Martins and Sébastien Faniel (postdocs) [23, 24]. The conductance-based SGM experiments have also been extended to thermoelectric measurements and called TSGM [25]. Other SGM experiments have been done by Boris in Grenoble, but with limited results since the microscope temperature was not low enough for a detailed study. A theoretical analysis of these results has been carried out by Krzysztof Kolasinski, a PhD student from Krakow, during a short stay in Grenoble [26] including spin-orbit effects [27, 28].

A direct continuation of this study was submitted to the ANR in 2014 and 2015, with the objective to investigate the properties of the spontaneously localized states revealed by our experiments. In this project, we included an optimization of the tuning-fork-based force sensor to reach the single-electron-charge sensitivity and possibly detect the presence of these localized states. Unfortunately this project was not funded, but since some of the proposed experiments may be performed in the future, I will briefly describe it in chapter 5. We then decided to move to a different topic and to investigate the spatial extension of the Kondo cloud around semiconductor quantum dots using both transport and SGM experiments. This ANR project KONEX was submitted to the ANR in 2016 and 2017, and was finally selected for funding in December 2018. It has started in June 2019 and will be discussed extensively in chapter 5.

In 2015, I started working on graphene physics, in collaboration with Benjamin Sacépé from the same QuNES team, who initiated an important research activity on this topic. High-impact results have been obtained by Katrin Zimmermann (PhD) and Louis Veyrat (postdoc) on split-gated graphene devices in the quantum Hall regime [29, 30, 31] and more

recently by Corentin Deprez (PhD) [32]. These transport experiments are complemented by scanning probe experiments, including STM with Alexis Coissard (PhD) and SGM with Marco Guerra (PhD). When graphene is encapsulated into a BN/graphene/BN heterostructure to fabricate a high-mobility device, STM cannot be used anymore and SGM becomes the most appropriate scanning probe. Two projects using SGM are currently running on graphene, one on the negative refraction at a pn interface, and one on the quantum Hall effect. They will be described in the last chapter 6.

My past research activity on Casimir force

From 2005 to 2011, in parallel with my work on quantum transport, I also worked on the Casimir force by doing experiments at low temperature. This research project had been initiated by Joël Chevrier a few years before and was at the origin of my position as assistant professor at the University of Grenoble. The objective of the project was to measure quantitatively the Casimir force between materials with specific dielectric properties or patterning, and to compare the results with theoretical calculations made at the LKB in Paris. Since the effects of the material properties on the force appear at relatively large distances where the force is very small, such a project required the development of a very sensitive force detection system.

During the PhD thesis of Justine Laurent [33], we developed a cryogenic AFM at 4.2 K in order to reduce the thermal noise of the cantilever, which was the limiting noise source in the force measurement. Using this setup, we studied back-action effects of the interferometric detection on the cantilever [34] and hydrodynamic effects at low pressure in confined geometries [35]. We also obtained quantitative Casimir force measurements on a silicon surface which was compared with theoretical calculations [36]. This research activity on low-force detection is not presented in the manuscript, but I will use this knowledge to develop new force sensing experiments on quantum electronic devices.

Thanks to this research activity which made me familiar with the various AFM-based force detection techniques, I could participate to the effort (initiated by Joël Chevrier, Florence Marchi, Hervé Courtois, and others) in teaching scanning probe microscopy in the Masters of the Grenoble University. Part of my teaching activities has been to giving AFM and STM practicals, at Master UGA an Nanotech of G-INP and at the European school ESONN. Related to this teaching activity, I have been in charge of the *Nanomonde* platform located at the CIME-Nanotech from 2008 to 2016. During this period, I have also participated to the *Nano@School* program for teenagers and to the *Fête de la Science* organized every year on the platform.

Content of the manuscript

In chapter 1, I explain the working principle of the scanning gate technique and give an overview of the various quantum phenomena that have been studied with this technique by only few groups in the world. I also present briefly the other scanning probe techniques that can be used to investigate quantum effects in two-dimensional electron gas and nanostructures. In the last section, I describe the instrumental aspects of the technique related to the building of a cryogenic scanning probe microscope compatible with transport measurements.

In chapter 2, I present a detailed analysis of the potential perturbation applied by the tip in the 2DEG. Such a discussion is not present in the literature and could be interesting for the community. This analysis explains how to combine the finite screening effect of the 2DEG with the local capacitance effect of the tip/surface system, first through analytical expressions and then with simulations based on finite element calculations.

In chapter 3, I describe our SGM investigations of mesoscopic effects in quantum rings and other nanostructures patterned in InGaAs 2DEGs. They include experiments at zero or low magnetic field, and experiments in the quantum Hall regime.

In chapter 4, I describe our detailed study of the conductance anomalies in GaAs quantum point contacts. We used SGM to tune the 0.7 and zero-bias anomalies, to perform scanning gate interferometry, and to probe thermoelectric effects.

In chapter 5, I present the new research projects on GaAs devices that have been started recently, and others that could be performed in the future. This includes some continuations of past research works, such as on the conductance anomalies in quantum point contacts, and new topics like measuring the extension of the Kondo cloud around quantum dots.

In chapter 6, I describe my research activity on graphene physics and present my projects in this field. A project is currently running on the SGM imaging of the ballistic refraction in a graphene p-n junction, and another project deals with the manipulation of quantum Hall edge channels in graphene to perform interferometers.

Chapter 1

Scanning probes for semiconductor devices

Quantum phenomena in mesoscopic devices correspond to modifications of the local electronic properties due to the wave-like nature of the particles in a particular geometric configuration. When the electronic system resides at the free surface of the sample, the local electronic properties can be *directly* measured by scanning tunneling microscopy (STM) using a metallic tip polarized with respect to the sample, the tunneling current being proportional to the local density of states at the energy corresponding to the tip voltage. On the other hand, when the electronic system is buried in an otherwise insulating heterostructure, the tunneling current at low bias is exponentially suppressed and the STM technique can not be applied.

The SGM technique has been introduced to investigate the quantum transport phenomena, where not only the density but also the transmission is important. As opposed to STM, SGM is an *indirect* method to probe the local electronic properties, since it uses a local gate effect to modify the spatial distribution of electron wave functions and record the consequence of this local perturbation on the device conductance. The main field of application of this technique concerns the quantum transport phenomena in III-V semiconductor heterostructures forming high-mobility 2D electron gases (2DEG) as illustrated in Fig. 1.1. The objective of the first part is to present the working principle of SGM and to briefly review the main results obtained by other groups with this technique.

Other scanning probe techniques have been used to obtain spatial information on the electronic properties of buried systems, such as the electrostatic force microscopy or the scanning single-electron transistor, that measure the local potential and the presence of discrete charges, or the scanning capacitance microscopy, that uses a high-frequency capacitive current to access the local density and conductivity. The second part of the chapter presents briefly these techniques, which provide interesting and complementary information on quantum phenomena in 2DEGs.

The last part describes several technical aspects related to the SGM technique. It em-

phasizes the difficulties encountered when trying to combine transport in mesoscopic devices with scanning probe experiments. It explains the different elements that constitute an SGM microscope, from a general point of view, and in the particular case of the instrument developed in our laboratory. The crucial aspects related to the tip and the force sensor are discussed, and the solutions used by the different groups are given.

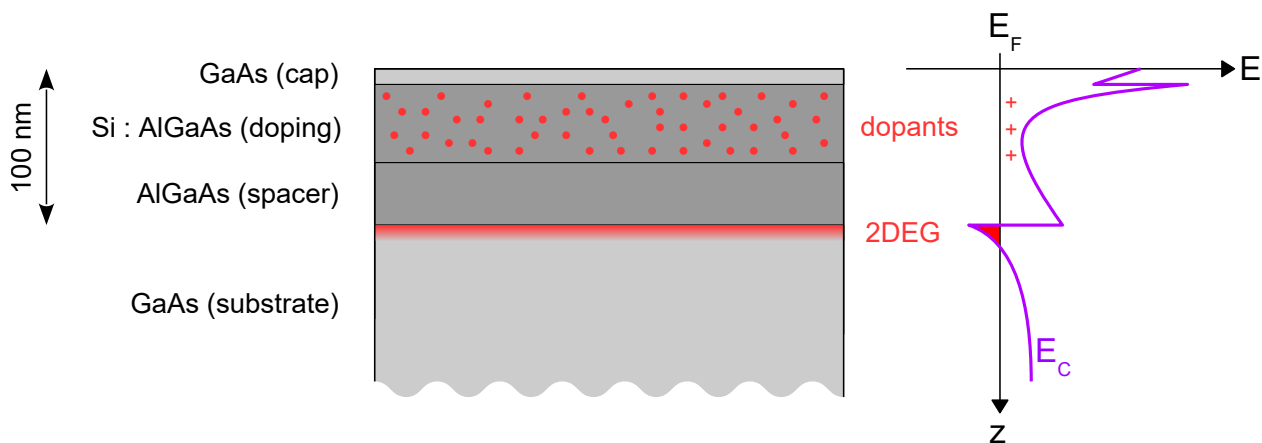


Figure 1.1: Semiconductor heterostructure grown by molecular beam epitaxy. Charge transfer from the doped layer creates a high-mobility 2D electron gas (2DEG) at the interface below the spacer layer. At low temperature, the doped layer does not contribute to transport since dopants are frozen. In the studied GaAs/AlGaAs heterostructures, the 2DEG is located 100 nm below the surface. This large distance is required to obtain a high electron mobility.

1.1 Presentation of Scanning Gate Microscopy

Working principle of SGM

An SGM experiment is based on a standard transport experiment in which the conductance of a mesoscopic device is measured as a function of several parameters like bias voltage, gate voltages, magnetic field, temperature. Most of the time, the quantum phenomena are already visible in these transport measurements. The purpose of SGM is to add a control parameter in order to probe or tune the quantum phenomena in the real space. A metallic tip is positioned with piezoelectric actuators at a position close to the device and is connected to a voltage source. The tip voltage induces a local potential change for the electrons in the device, with controllable amplitude and position, as illustrated in Fig. 1.2. The tip therefore acts as a local movable gate, a sort of *flying* gate.

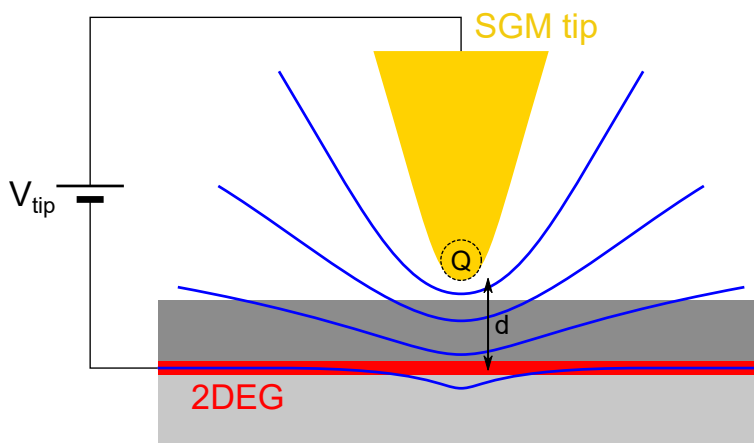


Figure 1.2: Schematics of the isopotential lines between the scanning gate and the 2DEG when a voltage is applied to the local gate. The sharpness of the tip makes this capacitor equivalent to the situation of a point charge Q whose value depends on the tip voltage V_{tip} and tip distance d . Due to imperfect screening by the 2DEG, the tip potential penetrates into the 2DEG in a small region below the tip.

After cooling down and electrical characterization of the device, the first step of any SGM experiment is to determine the position of the device with respect to the tip coordinates. Since the surface of the semiconductor heterostructure is insulating (STM can not be used), the tip is mounted on a force sensor (see details in 1.3) which feels the mechanical contact of the tip on the surface. The position of the device is recorded by standard AFM topography, either by imaging the device itself, or by imaging markers placed around it in order to avoid possible damage or contamination of the active part of the device.

After locating the device position, the tip is lifted at a finite height above the surface and polarized at a given voltage (usually negative) with respect to the 2DEG. Because of

imperfect screening by semiconductor 2DEGs (as opposed to metals with larger electron densities), the electrostatic potential in the 2DEG is modified below the tip (see details in 2) and this potential change affects the electron transport at the Fermi level. By raster scanning the tip above the surface, it is possible to record maps of conductance changes that contain spatial information on the electron transport in the device (see Fig. 1.3).

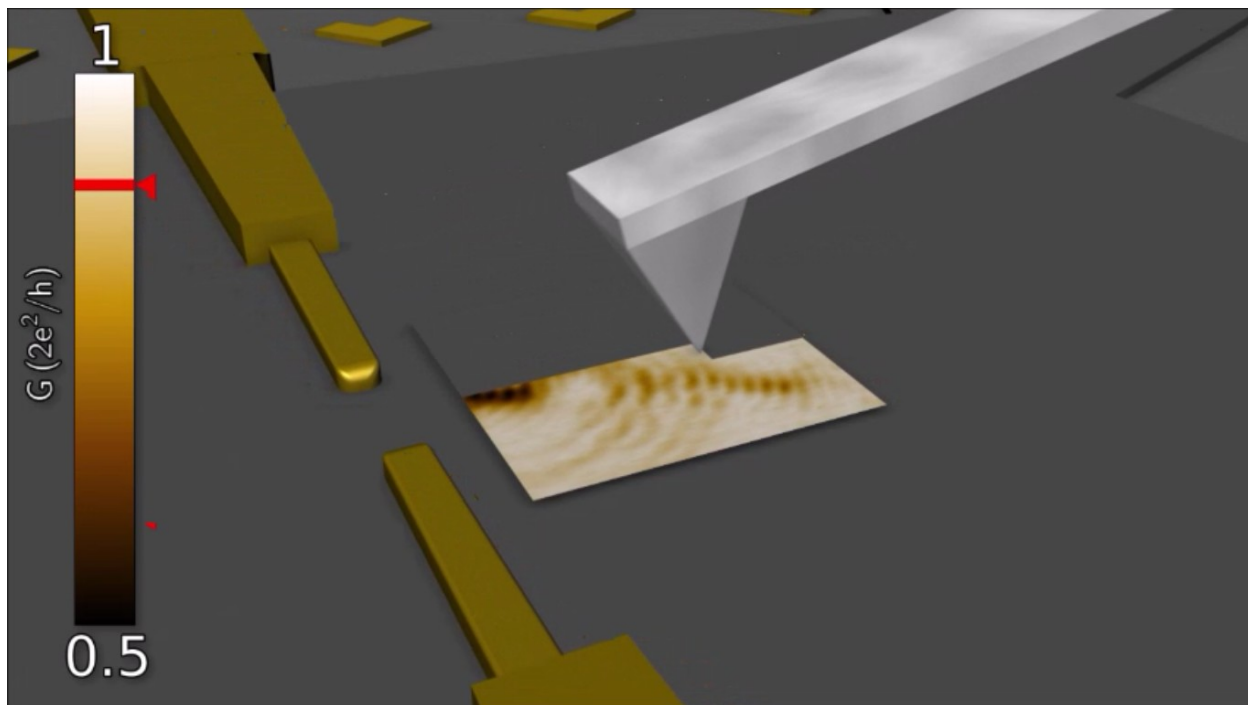


Figure 1.3: Artistic view of an SGM experiment on a QPC device (extracted from a video animation produced by Boris Brun during his PhD thesis). The polarized tip is raster scanned above the 2DEG in front of the split-gate electrodes and the QPC conductance is recorded as a function of the tip position. This operation produces a map of tip-induced conductance changes that reveals the branched electron flow in the 2DEG and the tip-induced interference fringes.

The SGM technique can be used for two different purposes : (i) to probe the spatial distribution of the electron flow or electron density in a mesoscopic device, or (ii) to tune its quantum properties by changing locally the potential landscape. In fact, these two effects are always combined during the same experiment because the probing effect is obtained by a local tuning of the potential. In this sense, SGM is an indirect probe of the electronic properties based on a controlled perturbation. For this reason, it is sometimes criticized by non-expert people who compare it with the STM technique which directly measures the local density of state. STM can however not be used on buried 2DEGs, and the SGM technique has been developed precisely to circumvent this problem. SGM being an indirect probe, it

is nonetheless true that quantitative analysis of SGM data require numerical simulations of quantum transport through the device in presence of the tip-induced potential perturbation. On the other hand, SGM provides very high resolution images of quantum phenomena controlled by the tip position. Since this position is controlled with nanometer precision, details of such a size could be seen in SGM images, for example in case of tip-induced interference effects.

Review of experimental works on SGM

The objective of this part is to give an overview of the nanostructures that have been studied by SGM during the 20 years of existence of the technique and to list the very few groups which are involved in these SGM experiments.

The use of the SGM technique has been reported for the first time in 1996 by the group of R. Westervelt at Harvard University (USA). They studied different phenomena, including the electron flow through QPCs [37], the conductance quantization in QPCs [38], the branched electron flow in 2DEGs [39], the interference effect between QPCs and mirror gates [40], the ballistic transport between two QPCs in magnetic focusing conditions [41], the Coulomb blockade effect in 2DEG-based QDs [42], and the formation of QDs in InAs nanowires [43]. In graphene devices, they studied conductance fluctuations [44], magnetic focusing and collimation [45, 46] and Andreev reflection at superconducting contacts [47]. All these experiments have been performed in a liquid helium cryostat at 1.7 or 4.2 K.

The group of D. Goldhaber-Gordon at Stanford University (USA) started its SGM activity by extending the pioneering work done in Harvard. They worked in detail on the interference effect in SGM images outside QPCs and revealed the crucial role played by the residual impurities in the 2DEG [48], the effect of the temperature down to 350 mK [49] and the effect of a finite excitation energy on the coherence [50]. They also studied the potential inhomogeneities in graphene constrictions [51] and the edge-state transport in topological insulators [52]. Most of these experiments have been performed between 1.7 and 4.2 K.

The group of D. Ritchie from the Cavendish Laboratory in Cambridge (UK) started its SGM experiments around 2000, soon after the group from Harvard. They studied the collimation of the electron beam flowing outside a QPC [53], the ballistic trajectories between two series QPCs under perpendicular magnetic field [54], and the conductance fluctuations in chaotic cavities [55]. They developed a technique of erasable electrostatic lithography to build nanostructures in 2DEG *in-situ* at low temperature [56], that they applied on the investigation of the conductance anomalies in QPCs [57]. They also studied the inhomogeneities of the charge neutrality point in graphene devices [58, 59] and imaged the ballistic trajectories in high-mobility graphene by magnetic focusing experiments [60]. Several of these experiments have been performed at very low temperature in a dilution fridge.

The group of K. Ensslin at ETH in Zürich (Switzerland) worked initially on devices patterned by local anodic oxidation of the GaAs heterostructures. They studied QDs [61] and QPCs [62], revealing the presence of charge traps near the 2DEG [63] and showing the

importance of the tip quality on the induced potential [64]. They also studied graphene devices patterned into QDs [65]. Then, they have been working on ballistic nanostructures defined by metallic top gates on the GaAs heterostructures. They studied the lateral shift of the channel in clean QPCs [66], the control of a QPC transmission by the tip-induced potential [67], the creation of an Aharonov-Bohm ring in a cavity by the tip-induced potential [68], the branching of the electron flow in the 2DEG outside QPCs [69], its dependence on the QPC transmission mode [70], the lateral confinement of electron transport in a long channel [71], the scattering states in an open circular resonator [72], and gate-defined bilayer graphene devices [73]. All these experiments have been performed down to 300 mK in an ^3He cryostat. In the quantum Hall regime, they studied the transition between plateaus in Hall bars [74], the formation of resonant states around the tip-induced potential [75], and the transmission of fractional quantum Hall edge channels through QPCs [76]. The last two experiments have been performed at very low temperature in a dilution fridge. They also evidenced viscous electron transport properties in a large temperature range down to 30 mK [77].

The group of S. Heun at NEST in Pisa (Italy) studied the equilibration process between quantum Hall edge channels [78], the transmission of fractional quantum Hall edge channels in QPCs [79], the origin of the 0.7 anomaly in QPCs [80], and backscattering of quantum Hall edge channels in graphene Hall bars [81]. These experiments have been performed down to 300 mK in an ^3He cryostat.

The group of Y. Ochiai at Chiba University (Japan) studied constrictions patterned by etching in InGaAs heterostructures. They observed images of the disorder potential [82], edge state transport in the quantum Hall regime [83], and conductance fluctuations induced by quantum interference [84]. More recently, they studied open quantum dots in GaAs heterostructures [85] and weak-localization effects in graphene constrictions [86]. These experiments have been performed down to 300 mK in an ^3He cryostat.

The group of Y. Hirayama at Tohoku University (Japan) studied the breakdown of the topological quantum Hall protection under non-equilibrium conditions [87] at 300 mK.

The group of P. McEuen, first in Berkeley, and later in Cornell (USA), used SGM to study the back-scattering between quantum Hall edge channels [88] and a combined SGM-EFM technique to probe the formation of QDs in carbon nanotubes [89]. These experiments were performed down to 600 mK in an ^3He cryostat.

For completeness of this review, I summarize briefly here the work done by our group in Grenoble (France) and in collaboration with Benoît Hackens in Louvain-la-Neuve (Belgium). The details will be given in the following chapters. We worked initially on nanostructures patterned by etching in InGaAs heterostructures, and then on QPCs defined by metallic top gates in GaAs heterostructures. In Grenoble, we studied interference effects in quantum rings [6, 7], the mesoscopic Braess paradox in double-rings [18], and the formation of QDs in narrow wires [21], using a liquid helium cryostat at 4.2 K. In Louvain-la-Neuve, we studied Coulomb blockade effects in quantum rings in the quantum Hall regime [13, 14, 15] and the conductance anomalies in QPCs [23, 24, 25], using a dilution fridge down to 30 mK. Recently,

the group in Louvain-la-Neuve also studied coherent transport in graphene quantum rings [90] and tip-induced refraction in graphene constrictions [91].

Review of theoretical works on SGM

Since SGM is a perturbation technique where the influence of the tip on the 2DEG is at the origin of the information extracted on the system, it is fundamental to analyze theoretically the connection between the measured SGM signal and the 2DEG properties in absence of the tip. Several groups have worked on this question continuously along the years to help experimentalist in the data analysis or to propose new SGM experiments to investigate other physical phenomena. Other theoreticians have occasionally reported works based on the SGM technique but will not be listed here to keep it short.

The group of E. Heller at Harvard University (USA) studied the properties of the branched electron flow revealed by the SGM experiments, the interference effects [92] and the pattern stability [93]. He also highlighted the similarities with the propagation of surface waves in the oceans [94].

The group of M. Pala at IMEP in Grenoble (France) worked in close collaboration with us to interpret our experiments and predict new effects. They studied the relation between the SGM signal and the local density of states [8], the influence of defects and magnetic field in SGM images recorded on quantum rings [9], and they demonstrated the existence of a counter-intuitive effect in double-ring nanostructures called the mesoscopic Braess effect [18].

The group of J-L. Pichard at CEA/SPEC in Saclay (France) studied the influence of electron interactions in QPCs on the SGM-tip-induced interference patterns [95], and this work has been at the origin of our experimental work on the QPC conductance anomalies. They also studied the effect of temperature on the interference visibility [96] and the effect of spin splitting under parallel magnetic field [97].

The group of R. Jalabert and D. Weinmann at IPCMS in Strasbourg (France) has been working on interaction effects in QPCs, in collaboration with J-L. Pichard, and then studied the general relation between the SGM signal and the unperturbed electronic properties [98, 99], including the effect of a finite bias [100]. Recently, they studied the origin of the SGM signal in chaotic cavities in order to interpret experiments in collaboration with the group of K. Ensslin [101].

The group of B. Szafran in Krakow (Poland) studied the application of SGM on quantum rings [102, 103], quantum dots [104], QPCs in the quantum Hall regime [105], double-slit interferometers [106], and 2DEGs with disorder [26]. They also worked on the use of SGM technique to investigate graphene devices, such as the formation of tip-induced quantum Hall interferometers [107] and the imaging of snake orbits in p-n junctions [108].

The group of F. Peeters in Antwerp (Belgium) worked on the interpretation of the SGM maps on 2DEG quantum rings [109] and studied the SGM imaging of magnetic focusing in graphene devices [110].

1.2 Other scanning probes for 2DEG investigations

Electrostatic force microscopy

While AFM in contact mode is dominated by the topography of the surface, AFM operated in non-contact mode is sensitive to long-range electromagnetic forces, and therefore to both the surface and the bulk of the material. Electrostatic force microscopy (EFM) corresponds to measurements of the electrostatic properties of a material using a metallic tip at a controlled potential. Measurements of surface potentials are obtained with a specific technique called Kelvin force microscopy (KFM) in which an AC voltage is also applied to the tip at the resonant frequency of the cantilever such as to induce an oscillation proportional to the potential difference between the tip and the surface. The surface potential is then found by adjusting the DC voltage on the tip such that the oscillation is suppressed.

In semiconductor heterostructures, the surface potential depends not only on the work function of the top surface, but on the entire potential profile throughout the heterostructure, as a result of the band-gap offsets between the layers, the presence of charges in the doped layer or at the surface, and the formation of a 2DEG at the interface. The presence of a 2DEG can therefore be studied by EFM or KFM measurements, as reported by the Ensslin's group using tuning-fork-based AFM at low temperature [111, 112]. A large negative voltage is applied on the tip in order to locally deplete the 2DEG (as often done in the SGM technique), this depletion threshold is detected by a sudden change in the tip-sample capacitance governing the electrostatic force, and the corresponding voltage can be used to extract the electron density in the 2DEG.

At first sight, force detection experiments do not appear particularly suitable for investigations of quantum transport phenomena in 2DEGs. In confined regions where electrons build interference patterns, a force detection would measure the total charge density below the tip, involving the electrons at all energies (and not only those at the Fermi level as in transport experiment), with a superposition of the energy-dependent interference patterns. In addition, the poor spatial resolution of a local probe located about 100 nm above the 2DEG would make it difficult to resolve interference fringes spaced by half the Fermi wave length.

For this reason, the only force detection experiments that have been reported in the context of mesoscopic physics are related to single-electron charging effects in quantum dots. A single elementary charge on an insulating surface can be easily detected by EFM, even at room temperature, as demonstrated in 1990 by C. Schönberger [113]. Coulomb blockade at low temperature has been observed by EFM and SGM in carbon nanotubes by P. McEuen [89], revealing disorder-induced potential barriers along the nanotubes. Coulomb blockade has also been detected by EFM in self-assembled InAs quantum dots, located at the surface and tunnel-coupled to a buried 2DEG, by P. Grutter [114]. In these two experiments, the tip also acts as a scanning gate and ejects the electrons one by one from the trapping potential when it approaches the dots. Interestingly, these experiments not only measured

the frequency shift induced by the force gradient, but also the mechanical dissipation induced by the finite tunneling rate of the electrons. To reach high sensitivity and detect single charges, these experiments used cantilevers as force sensors, with piezoresistive sensing [89] or infrared optical detection [114] to avoid excitation of charge carriers by the visible light of traditional cantilever detections.

Surprisingly, force detection of Coulomb blockaded charges has not been reported so far in quantum dots of buried 2DEGs, neither patterned by etching, nor defined by surface gates. In the latter case, the high voltages applied on the gate electrodes surrounding the quantum dots represent dangerous objects for tips attached to soft cantilevers, and stiffer sensors such as piezoelectric tuning forks might be more suitable for this application, despite their lower intrinsic sensitivity. Developing such an experiment would be a very interesting project which is briefly discussed in section 5.1.

Scanning capacitance microscopy

For 2DEGs buried about 100 nm below the surface, low-energy electron tunneling is not possible between the 2DEG and the tip, but an AC capacitive current can flow in response to a high-frequency AC voltage on the tip. In this technique called scanning capacitance microscopy (SCM), the AC electron flow reflects the local conductivity in the 2DEG, as opposed to the local density of state probed by STM.

This technique has been initially developed by R. Ashoori at the Massachusetts Institute of Technology [115, 116, 117, 118], and continued by S. Tessmer (a previous co-worker) at Michigan State University [119, 120, 121]. Instead of SCM, they call their technique subsurface charge accumulation (SCA) in order to differentiate it from standard room temperature scanning probe characterization of semiconductor devices based on capacitance measurements. Their microscope is a modified STM in an ^3He cryostat with a cryogenic charge amplifier attached to the tip. This amplifier reaches a sensitivity of $0.01 \text{ electron}/\sqrt{\text{Hz}}$ at the working frequency of 100 kHz. Tip positioning with respect to the surface is achieved in STM mode at high tip voltage (larger than 4 V) to overcome the potential barrier of the heterostructure.

Another low temperature SCM microscope has been developed by C. Mellor at the University of Nottingham [122, 123]. This microscope uses a quartz tuning fork as force sensor for topography and works down to 1.6 K in an ^4He cryostat. The capacitance detection uses a low-temperature RLC circuit with 100 MHz resonant frequency and including the small tip-sample capacitance to be measured. The resonance is probed by excitation and pick-up coils inductively coupled to the resonant circuit. This high-frequency technique allows a faster detection, which is more suitable for scanning, than the charge detection approach of the above SCA technique.

The SCM technique has been used to probe the spatial variations of the electron compressibility in the quantum Hall regime. When the magnetic field or the charge density is adjusted such as to be at integer filling factor, the bulk of the 2DEG is insulating and no

AC current can flow in the tip, except on the edges of the sample where compressible stripes are present and forms the so-called edge channels [117, 123]. When the filling factor is tuned slightly off an integer value, the spatial variations of the potential lead to the appearance of local compressible regions in the almost insulating bulk of the 2DEG [115]. The position of these compressible regions reveal the spatial inhomogeneities of the electrostatic potential induced by disorder in the charge distribution, either in the doping plane or at the surface.

The SCM technique has also been used at zero magnetic field to image the position of dopants in GaAs-based and Si-based heterostructures [120, 121] by detecting capacitively the tunneling conductance between the 2DEG and the dopants. The spatial resolution was not sufficient to separate individual Si dopants in GaAs devices, but individual B dopants could be imaged in Si devices.

Scanning single-electron transistor

The spatial distribution of the charge carriers in the 2DEG can be imaged by placing a very sensitive electrometer at the apex of a sharpened glass fiber that forms the tip of the scanning probe microscope. Single-electron transistors (SET) have the sensitivity to detect 0.01 electron in the SET island and about 0.1 electron placed at 25 nm from the SET island. This instrument has been developed by A. Yacoby at the Bell Laboratories, then at the Weizmann Institute, and now at Harvard University. It has been applied to 2DEGs to measure charges [124] and localized states in the integer [125, 126] and fractional [127] quantum Hall regimes. We can also mention that this technique has been applied to graphene (surface 2DEG), showing electron-hole puddles at the charge neutrality point [128] and localized states in the quantum Hall regime [129].

1.3 Instrumental aspects of SGM

Challenge of combining transport with scanning probe

An SGM experiment is the combination of an electronic transport measurement of a micron-size device at low temperature and a scanning probe microscopy experiment on this device. The specific difficulty of the SGM technique is to manage having both experiments working at the same time. This statement looks trivial, but in practice this matching situation is not so easily obtained.

Due to their very small size, mesoscopic samples are unique and not always working properly. Intrinsic microscopic details vary from sample to sample, such as the random distribution of dopants in the semiconductor heterostructure, making two apparently identical devices different regarding their electrical properties. In addition, their fabrication process is not perfectly reproducible due to defects during the lithography, dust particles on the wafer, lift-off residues, non-constant wet etching rate, polycrystalline metallic grains, sensitive diffusion of ohmic contacts, etc..., and some devices simply do not work.

In the case of SGM, this difficulty typical of mesoscopic physics experiments adds to a second difficulty which is to position the tip of the microscope in close proximity with the device, at low temperature, without inducing irreversible changes. This locating operation is required by the significant thermal drift occurring during the cooling down to liquid helium temperatures and can be very difficult to do for large drifts due to the absence of optical access. These topography measurements present the risk to physically damage the structure, and the tip, if the feedback parameters are not carefully adjusted, especially with stiff force sensors such as quartz tuning forks (see following section). Scanning the tip on the surface can also contaminate the tip with a dust particle, which would then affect the potential induced by the tip in an uncontrolled manner. It is therefore important to keep the sample surface very clean and exempt of dust particles.

In addition, mesoscopic devices are very sensitive to contamination of the surface or charging of the semiconductor structure. Even a single charge trapped close to a point contact can change its conductance. Scanning the tip in contact with the active part of the device can irreversibly change the electrostatic environment. Only thermal cycling close to room temperature would fully restore the initial state. For this reason, a few guiding marks patterned on the sample, far from the active part of the device, are imaged in topography mode to determine the position of the device.

When these preliminary operations are achieved successfully and the sample is working, the SGM measurements are carried out with the tip lifted by about ten nanometers above the surface. In this lift mode, measurements can be performed during very long periods of time (typically one day) because the microscope is mechanically very stable at liquid helium temperature, and the relative position of the tip and the sample does not drift. Note however that the experiment must be stopped every two or three days when the cryostat needs to be refilled with liquid helium. During this operation, the tip is retracted a few microns away

from the surface for safety reason.

Unfortunate events can also occur during the SGM operation and put an end to the experiment. If disturbances of the power network create voltage spikes in the electrical wiring of the microscope, the tip may crash on the surface. Small electrical perturbations can also shift the tip position, and the tip can then touch a metallic top gate, immediately blowing up the device, due to the large voltage difference (a few Volts) between the tip and the gate. For this reason, the scanning area is usually kept at a minimum safety distance from surface gates.

Technical description of the instrument

An SGM microscope is a cryogenic AFM microscope equipped with electrical wiring for transport measurements. The quality of measurement wiring influences the lowest electronic temperature that can be reached. In liquid helium cryostats, the two essential features are (i) the electrical filtering of the high-frequency noise using RC or LC filters at the top of the low-temperature insert and (ii) the thermal anchoring of the wires on a metallic plate at low temperature in order to reduce the electron temperature from 300 K to 4 K before going to the device. In dilution fridges, the wires should be again thermalized at each lower temperature stage and filtered against high-frequency excitations using stainless steel coaxial cables or copper powder filters.

The sample is either mounted on the microscope actuators (and the tip is fixed), or fixed on the coldest part of the fridge to reach the lowest temperature (and the tip is moving). The actuators are made of piezoelectric elements working in continuous mode for scanning purposes and in pulsed mode for inertial displacements over large distances. Compact non-magnetic actuators are commercially available (e.g. from the Attocube company) with integrated position sensors that can be used for closed loop operation. The XYZ scanner is either a piezoelectric tube with five electrodes, or made of three independent piezoelectric stacks acting in orthogonal directions. Ideally, the microscope wiring should also be filtered against the high-frequency noise of the room, in order to avoid their radiation on the device in the sample space, especially for measurements at very low temperatures. The pulsed operation of the inertial actuators requires however a large bandwidth and the cut-off frequency of the filters should be chosen with care.

The body of the microscope should be very rigid to avoid deformations during the loading into the cryostat, and symmetric to minimize drifts of the tip position due to differential contractions during the cooling down. The first version of our microscope developed at Spectro Lab in 2005 was made of four tubes fixed by screws between two stages. This structure was not sufficiently rigid and was replaced by a metallic body in the current version of the microscope built in 2012 at Néel Institute (Fig. 1.4). This microscope is fitted into a 2-inch diameter tube and thermalized at the temperature of the cryostat by a small pressure of helium gas in the tube. Note that microscopes in He3 or dilution fridges are placed in a vacuum environment, and the actuators made of insulating piezoelectric ceramics should be

thermalized with a soft copper braid.

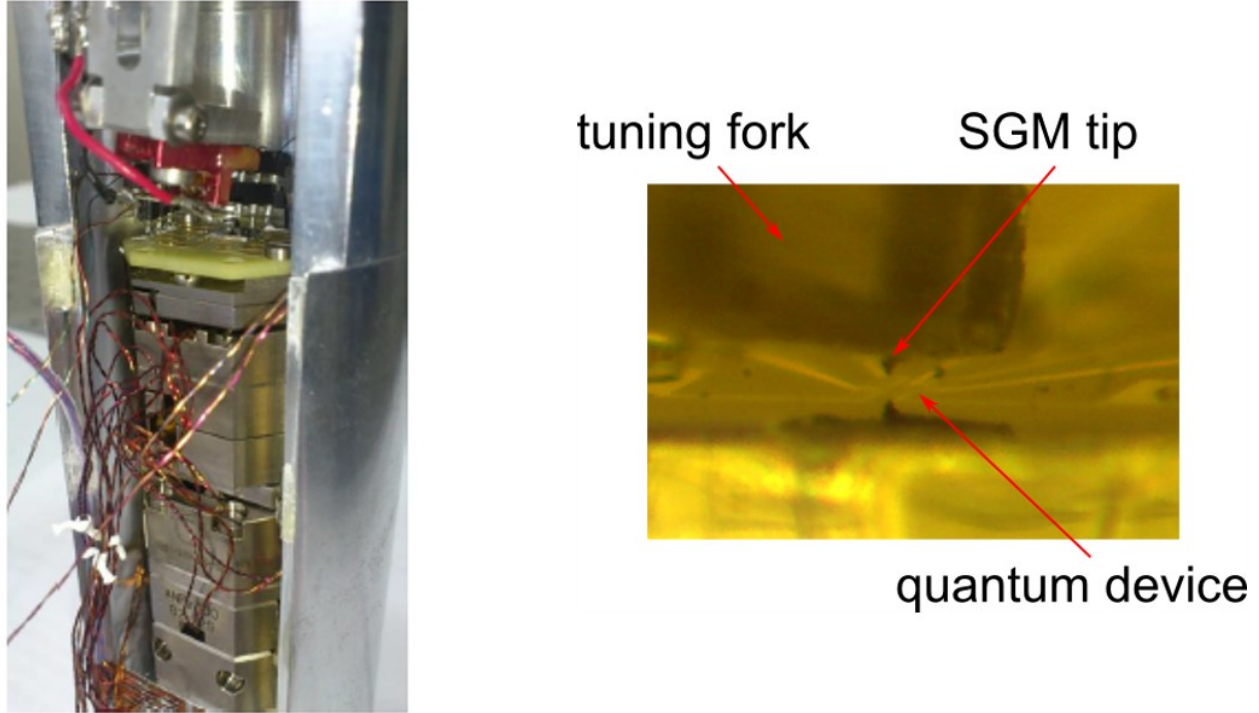


Figure 1.4: (left) SGM microscope built at Néel Institute and used in a liquid helium cryostat. (right) Preparation of the SGM experiment by positioning the tip close to the device.

The last but essential part of the system is the SGM tip which is attached to a force sensor to detect the position of the surface (in Z) and the location of the device (in X and Y). In AFM, the force sensor is usually a soft cantilever whose deflection is measured by the deflection of a laser beam. To obtain a more compact AFM microscope that can be fitted into a cryostat with a superconducting magnet, the deflection is preferably measured by the interferometric signal of an optical cavity formed between the cantilever and the end of an optical fiber. At the beginning of our work, we were using this type of force detection, but it presents two important drawbacks. The first one is related the drift of the optical fiber with respect to the cantilever during the cooling down from 300 to 4 K due to differential thermal contractions of the setup. The second one is the excitation of charges in the heterostructure by the visible light of the laser beam during topography, with a different charge configuration after each topography and with very long relaxation times.

For these reasons, it is better to use an all-electrical force detection to carry out SGM experiments on 2DEGs at low temperature. Several groups are using piezoresistive cantilevers made of doped silicon layers, and patterned in such a way that a current can circulate through the cantilever and its resistance can be measured. Unfortunately, these cantilevers

are not any more commercially available and require in-house manufacturing or collaboration with specific companies. We are now using another widely used force sensor, which is the piezoelectric quartz tuning fork (TF), made of two parallel beams covered with two metallic electrodes. A small AC voltage is applied to the electrodes at the nominal resonance frequency of 32768 Hz to excite the first vibration mode of the TF, and the piezoelectric current proportional to the amplitude of vibration is measured with a current-to-voltage amplifier. Despite its large mass and size compared to cantilevers, the TF response is very sensitive to an external force applied to a tip fixed on one beam of the TF, and this sensitivity is used to feel the contact of the tip on the surface.

The high stiffness of the TF (about 10000 N/m) is useful to avoid the jump-to-contact phenomenon encountered with soft cantilevers, in particular when the tip is close to a metallic top gate, where the tip-to-sample voltage generates a large attractive force. On the other hand, this high stiffness implies that very large forces are applied to the tip if the Z feedback is not properly tuned. Compared to atomically flat surfaces where TFs work well and are commonly used, measuring the topography of an electronic device with about 100 nm step height is much more difficult. In practice, the scan speed during topography measurements has to be very slow to preserve the tip from being damaged. In addition, TFs have quality factors larger than 100000 at low temperature, corresponding to a time response of a few seconds, which is too long for allowing a Z feedback to be done on the vibration amplitude. TFs thus require the Z feedback to be done on the much faster phase response, or better, on the shift of the excitation frequency applied in real time by phase-lock loop (PLL) to cancel the phase changes. This frequency shift is indeed proportional to the applied force over a much larger range of force than the phase response at fixed excitation frequency (which is linear only for small force gradients with frequency shifts smaller than the width of the resonance peak). In this operation mode called frequency modulation feedback, the set-point of the Z feedback is a value of frequency shift, positive for a repulsive average interaction, negative for an attractive one. The attractive regime is very delicate to handle and works only on flat surfaces. For topography of electronic devices, one should use a positive frequency shift (typically 200 mHz) to have a stable feedback.

Contrary to AFM cantilevers which already have a sharp tip at the end, the use of TFs requires the preparation of a tip, either by electrochemical etching of a thin metallic wire, or by transferring a commercial AFM cantilever with its tip (Fig. 1.5). This second approach gives sharper and more reproducible tips, thus providing a better control of the tip-induced potential during SGM experiments. These crystalline silicon tips are coated with a metallic layer made of Cr and PtIr (25 nm thick for tips from Nanosensors), giving a radius of curvature at the apex of about 30 nm. In comparison, etching metallic wires (tungsten or platinum/iridium) give bigger tips and are used preferentially for STM/AFM applications on flat surfaces where the overall shape of the tip is less important. Fixing a cantilever on a TF is a delicate operation which is executed with micro-manipulators under a binocular microscope. A thin layer of silver epoxy glue is deposited at the extremity of the TF, on the insulating quartz region, but extending up to the metallic TF electrode that will be used to

1.3. Instrumental aspects of SGM

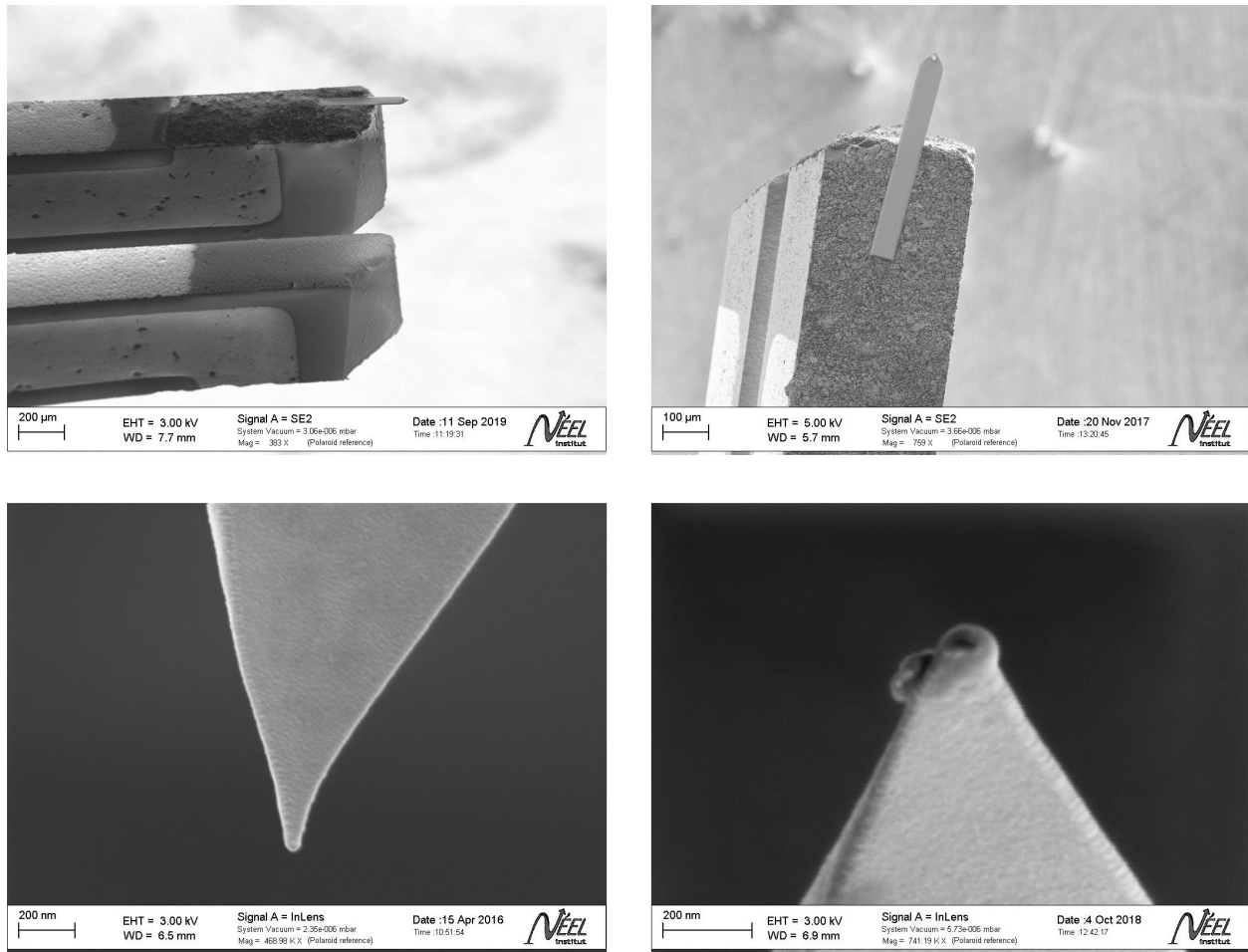


Figure 1.5: (top) Quartz tuning fork used as force sensor for AFM and EFM imaging. A commercial AFM cantilever is fixed with conductive epoxy over half its length. (bottom left) Apex of the commercial AFM tip made of crystalline silicon coated with a platinum-iridium alloy. (bottom right) Example of a broken tip apex after a SGM experiment.

control the tip voltage. The cantilever is approached toward the TF and placed in contact with the film of glue at the very end of the TF. By moving further down the small silicon wafer, the cantilever breaks from the wafer precisely at the base of the cantilever. When the cantilever is fixed over its entire length, the resulting force probe is equivalent to a very stiff cantilever, and it has to be used with very great care, in particular with a low scan speed, as discussed above. By gluing the cantilever on half of its length only, with the tip at the end of the free-standing part of the cantilever, the spring constant at the tip is much smaller than for tips rigidly fixed to the TF, and the scan speed can be safely increased to much higher values. The manipulation required to fix the cantilever in this configuration on the TF is a bit more tricky but is now routinely achieved in our group and also by our collaborators in Belgium.

The electronic equipment necessary to control the microscope is made of several components : a system that generates pulses of specific shape to drive the XYZ inertial actuators, a low-noise high-voltage source to drive the XYZ scanner, a lock-in device to excite and measure the oscillation of the tip, a phase-lock loop to control the excitation frequency of the TF, a feedback loop to control the Z scanner, and a system to control the XY scanning operation with the possibility to record the signal from the transport measurement as a channel of the image. We use the system from Nanonis (SPECS) to control the microscope, and the electronics from Attocube to drive the inertial motors. The Nanonis software gives a full access to all the parameters, with a lot of possibilities for scanning and signal analysis, and features a programming interface under Labview.

Chapter 2

Local potential change induced by the SGM tip

During SGM operation, the tip apex is placed at a small but finite distance above the surface and polarized at a given voltage V_{tip} with respect to the 2DEG. The resulting electric field \vec{E} produces an accumulation of charges with opposite polarities on the tip and the surface (capacitive effect). In case of a negative tip voltage, electrons accumulate on the tip apex and a positive charge appears locally in the 2DEG, corresponding to a local reduction of the electron density. Due to the small density of state of semiconductors, as compared to metals, this local reduction of the electron density results in a local increase of the electrostatic potential inside the 2DEG. This local change of the potential then modifies the trajectories of the conduction electrons at the Fermi level, therefore modifying the conductance and producing the SGM signal.

In this chapter, we discuss in details the properties of the potential perturbation induced by the SGM tip in the 2DEG, explaining the different models and approximations used to obtain analytical expressions, or to perform numerical computations. This analysis is not present in the literature and could be useful for the SGM community.

2.1 Screening of the applied potential

When calculating the tip-induced potential in the 2DEG, the most fundamental question is whether one needs to solve self-consistently the quantum mechanical Schrödinger equation together with the electrostatic Poisson equation, which is a very difficult problem. Fortunately, when the Fermi wavelength is much smaller than the characteristic length scale of the potential landscape, one can neglect the wave nature of the electrons and use a local relationship between the electrostatic potential $V(\vec{r})$ and the carrier density $N(\vec{r})$, involving the density of states $\text{DOS}(E)$ of the 2D system, which greatly simplifies the problem. At low temperature compared to the Fermi energy, this situation is called the Thomas-Fermi approximation, and the relation writes $N(\vec{r}) = \int_0^{\mu+eV(\vec{r})} \text{DOS}(E) dE$, where μ is the electrochemical potential (uniform at equilibrium). This local approximation is usually valid for the potential induced in the 2DEG by the SGM tip (or by surface gates), because the 2DEG is buried several tens of nanometers below the surface of the heterostructure, resulting in smooth potential variations on the scale of the Fermi wave length. This situation is far from the case of a short-range scatter, such as an atomic impurity, which is known to produce Friedel oscillations in the 2DEG. The local approximation however fails in regions where the density approaches zero (close to depletion areas or in quantum point contacts) because the Fermi wave length diverges at zero density. This situation requires a quantum mechanical treatment, involving coupled Poisson and Schrödinger equations, which is a very demanding task. In the following, we assume the local Thomas-Fermi approximation to be valid.

For semiconductor 2DEGs, the density of states is independent of the energy, and the relation becomes $N(\vec{r}) = \frac{m^*}{\pi\hbar^2} (\mu + eV(\vec{r})) = N_0 + \frac{em^*}{\pi\hbar^2} V(\vec{r})$ where N_0 is the intrinsic carrier density of the 2DEG in absence of external potential and m^* is the effective mass of the carriers in the 2DEG. This linear relationship gives rise to a linear screening of the external potential, with two important limitations. First, the Fermi energy $E_F = \mu + eV$ (or chemical potential) should not reach the energy of the second sub-band of the 2DEG quantum well, otherwise the density of states becomes twice larger. Second, the carrier density cannot go below zero (there is no state in the energy gap of the semiconductor) and the relation is simply $N(\vec{r}) = 0$ in the regions where the 2DEG is fully depleted. This situation gives rise to a strongly non-linear screening at the boundary of the depletion region inside which there is no screening at all.

For graphene, the problem is different. The absence of energy gap at the Dirac point allows the carrier density to become negative, with a Fermi energy in the valence band, such that the existence of fully-depleted regions is not possible, and the external potentials are always screened by charge carriers. There is also no perpendicular sub-band since graphene is a perfectly 2D material and has a smooth density of state. The drawback, however, is the energy dependence of its density of states $\text{DOS}(E) \propto E$, which gives a non-linear relation $N(\vec{r}) = \frac{1}{\pi\hbar^2 v_F^2} (\mu + eV(\vec{r})) |\mu + eV(\vec{r})|$ where v_F is the constant Fermi velocity in graphene (in the low-energy approximation). Graphene therefore shows a continuous but non-linear screening of the external potential.

In the following, we consider the case of a semiconductor 2DEG in the regime of linear screening of the external perturbation. We discuss first the case of an SGM tip replaced by a point charge, since it allows a comparison between the exact self-consistent solution for the potential and an approximate solution deduced from the density for perfect metallic screening. This comparison will be used to evidence the high level of screening produced by the 2DEG, and to obtain the regime of validity of a quantum capacitance model. This model will then be used to calculate the potential induced by a realistic SGM tip with a spherical apex and a conical shape. The difficulty arising from the dielectric constant of the semiconductor top layer will be treated qualitatively by the introduction of an effective distance. At the end of the chapter, numerical simulations will be used to treat the correct dielectric configuration of a 2DEG heterostructure, and to consider the non-linear-screening situation occurring when the tip depletes the 2DEG.

2.2 SGM tip modeled by a point charge

Here the polarized tip is represented by a point charge Q_{tip} located at a distance d above an infinite 2DEG within a uniform medium with dielectric constant ϵ_r , or for two different dielectric media above and below the 2DEG with $\epsilon_r = \frac{\epsilon_{r1} + \epsilon_{r2}}{2}$ (see Fig. 2.1). Unfortunately, no analytical expression exists for the real case of a 2DEG embedded in an heterostructure, where there is an additional semiconductor/vacuum interface at an intermediate distance between the point charge and the 2DEG. Numerical simulations (see Sec. 2.6) will be needed to treat real cases. The solution obtained here for a uniform medium is however independent of ϵ_r and should therefore have a certain validity.

Direct calculation of the potential

In the regime of linear response (no depleted region in the 2DEG) and in the Thomas-Fermi approximation (short Fermi wavelength), the self-consistent potential in the 2DEG at a radial distance r from the position of the point charge can be expressed as : [130, 131, 132]

$$V(r) = \frac{Q_{\text{tip}}}{4\pi\epsilon_0} \int_0^\infty J_0(qr) e^{-qd} \frac{2q}{2\epsilon_r q + k_{s0}} dq$$

where J_0 is the zeroth-order Bessel function and $k_{s0} = \frac{m^* e^2}{\pi \hbar^2 \epsilon_0}$ is the screening wave vector in vacuum. This integral can be approximated by a combination of the asymptotic behavior at large r and the value at $r = 0$, which gives :

$$V(r) = \frac{Q_{\text{tip}}}{4\pi\epsilon_0 \epsilon_r d} \frac{I(a)}{1 + a I(a) \left((1 + r^2/d^2)^{3/2} - 1 \right)}$$

where the integral $I(a) = \int_0^\infty \frac{x e^{-x}}{x+a} dx$ is a function of the dimensionless parameter $a = \frac{k_{s0} d}{2\epsilon_r}$ which characterizes the level of screening. To calculate an order of magnitude of this

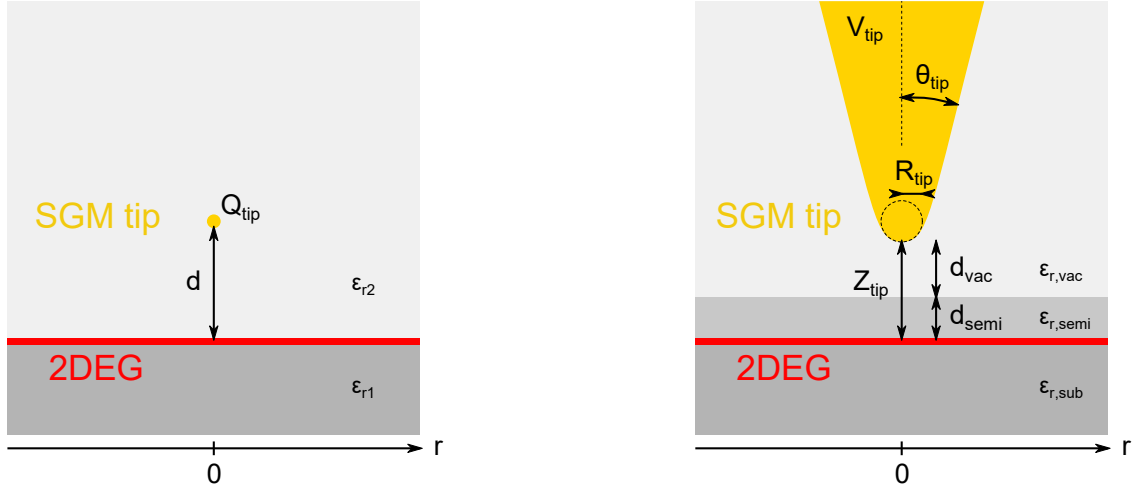


Figure 2.1: Schematic of the SGM experiment with a sharp polarized tip above a 2DEG. (left) Tip modeled by a point charge at a distance d . (right) Tip with a realistic shape at a distance Z_{tip} . Note that there is no analytical solution for the real situation with two different dielectric constants $\epsilon_{r,\text{semi}}$ and $\epsilon_{r,\text{vac}} = 1$ between the 2DEG and the tip.

parameter, we take the average dielectric constant of the semiconductor heterostructure and consider a charge located at $d = 100 \text{ nm}$ above the 2DEG within this effective dielectric medium. For InGaAs 2DEGs, using $m^* = 0.04 m_e$, $k_{s0} = 3.0 \text{ nm}^{-1}$, $\epsilon_r = 13.3$, we obtain $a = 11$. For GaAs 2DEGs, using $m^* = 0.07 m_e$, $k_{s0} = 5.3 \text{ nm}^{-1}$, $\epsilon_r = 12.7$, we obtain $a = 21$. For these large values of a , the integral $I(a)$ can be approximated by $1/a$ and the potential becomes :

$$V(r) = \frac{Q_{\text{tip}}}{4\pi\epsilon_0} \frac{2}{k_{s0} d^2} \frac{1}{(1 + r^2/d^2)^{3/2}}$$

The value at $r = 0$ is reduced by the factor $a \gg 1$ with respect to the unscreened potential $Q_{\text{tip}}/(4\pi\epsilon_0\epsilon_r d)$ in absence of 2DEG. The parameter a is therefore a measure of the screening intensity, which is large for usual semiconductor 2DEGs. At large radial distance, the unscreened $1/r$ decay of the Coulomb potential is replaced by the much faster $1/r^3$ decay which is characteristic of 2D screening. We also note that this expression is independent of the dielectric constant ϵ_r (which is uniform in this calculation).

Calculation from the metallic solution

We now show that this self-consistent potential for a 2DEG with large screening is identical to the potential deduced from the charge distribution in a perfect metallic plane using the

density of state of the 2DEG. This equivalence will allow us to introduce a local capacitance model for the calculation of realistic tip shapes.

The charge distribution in a metallic plane with a charge Q_{tip} located at a distance d from this plane is given by the electric field at the surface, which can be easily calculated with the image charge method based on the isopotential property of the metallic plane :

$$\sigma(r) = - \frac{Q_{\text{tip}}}{2\pi d^2} \frac{1}{(1 + r^2/d^2)^{3/2}}$$

Due to the finite density of state $\text{DOS} = \frac{m^*}{\pi\hbar^2}$ of the 2DEG, this induced charge density corresponds to a local change of the Fermi energy E_F by $\sigma/(-e)\text{DOS}$. But since thermodynamic equilibrium requires the electrochemical potential $\mu = E_F - eV$ to be uniform, the change of the Fermi energy (or chemical potential) corresponds to a change of the electrostatic potential V by a quantity $-\sigma/e^2\text{DOS} = -\sigma/\epsilon_0 k_{s0}$, which gives :

$$V(r) = \frac{Q_{\text{tip}}}{2\pi d^2 \epsilon_0 k_{s0}} \frac{1}{(1 + r^2/d^2)^{3/2}}$$

This expression is the same as the exact one calculated previously in the limit of large screening, showing that it is possible to use the case of perfect screening (with an isopotential surface) to calculate the self-consistent potential, by first calculating the induced charge density in the metallic case, and then dividing by the density of states.

2.3 Potential in the quantum capacitance model

Expression in the general case

For the realistic case of an extended metallic tip at a potential V_{tip} , if one assumes that the 2DEG is also perfectly metallic, it is possible to calculate the charge distribution $\sigma(r)$ on the capacitor plates, and then to deduce the self-consistent potential in the actual semiconductor 2DEG using its finite density of states. This method is based on the quantum capacitance model, which is valid for sufficiently good screening because the induced potential is then much smaller than the one applied on the gate.

The two equations of the quantum capacitance model are $\sigma(r) = -C(r) (V_{\text{tip}} - V(r))$ and $\sigma(r) = -e^2 \text{DOS} V(r)$ with $\text{DOS} = \frac{m^*}{\pi \hbar^2}$. In these equations, the local surface capacitance $C(r)$ would correspond to the charge distribution $\sigma(r)$ for a metallic 2DEG where $V(r) = 0$. The combination of these equations gives the self-consistent potential in the semiconductor 2DEG :

$$V(r) = \frac{C(r)}{C(r) + e^2 \text{DOS}} V_{\text{tip}}$$

Note that the quantum capacitance model is also valid for graphene, but the screening is non-linear, and the equations are a bit more complicated.

Since the local capacitance $C(r)$ can never exceed the value of the plane-plane geometry $\frac{\epsilon_0 \epsilon_r}{Z_{\text{tip}}}$, its spatial distribution can be characterized by a dimensionless function $f(r)$ lower than unity such that :

$$C(r) = \frac{\epsilon_0 \epsilon_r}{Z_{\text{tip}}} f(r)$$

where ϵ_r is the dielectric constant in the capacitor and Z_{tip} is the minimal distance between the scanning gate and the 2DEG plane. Using this dimensionless function, the self-consistent potential then writes :

$$V(r) = \frac{f(r)}{f(r) + 2a} V_{\text{tip}}$$

where $a = \frac{k_{s0} Z_{\text{tip}}}{2 \epsilon_r}$ is the parameter already introduced previously, which characterizes the level of screening, and $k_{s0} = \frac{m^* e^2}{\pi \hbar^2 \epsilon_0}$ is the intrinsic screening wave vector of the 2DEG.

Expression for large screening

In SGM experiments, the parameter a is much larger than unity (around 10 to 20) because the tip is usually several tens of nanometers above the 2DEG whereas the screening length is only a few nanometers in semiconductor 2DEGs. This means that the screening length in the 2DEG is much shorter than the characteristic length of the spatial variations induced by

the tip in the 2DEG. Since the term $f(r)$ is always smaller than unity, the above expression of the induced potential simplifies into :

$$V(r) = \frac{f(r)}{2a} V_{\text{tip}}$$

The potential in the 2DEG below the tip is therefore a fraction $f(0)/2a \ll 1$ of the applied tip voltage, and it decreases in space with a dependence $f(r)$ given by the local metallic capacitance $C(r)$.

Influence of the dielectric constant

The expression $V(r) = f(r) \frac{\epsilon_r}{k_{s0} Z_{\text{tip}}} V_{\text{tip}}$ assumes an homogeneous medium between the tip and the 2DEG, with a unique dielectric constant ϵ_r . In a real SGM experiment however, the medium between the tip and the 2DEG is composed of a layer of semiconductor on top of the 2DEG and vacuum around the tip. An effective dielectric constant :

$$\epsilon_r^{\text{eff}} = \frac{d_{\text{vac}} + d_{\text{semi}}}{d_{\text{vac}} + \frac{d_{\text{semi}}}{\epsilon_{r,\text{semi}}}}$$

might be used to get a more quantitative value of the tip-induced potential, with d_{vac} the tip height above the heterostructure, d_{semi} the thickness of the semiconductor top layer, and $Z_{\text{tip}} = d_{\text{vac}} + d_{\text{semi}}$. This effective dielectric constant quickly drops from $\epsilon_{r,\text{semi}} \approx 13$ to less than 2 when the tip distance above the surface (d_{vac}) increases from zero to a height equal to the top-layer thickness (d_{semi}) which is around 50 to 100 nm, and then slowly tends towards 1 at larger distances as if the tip would be in vacuum.

The tip-induced potential is then given by :

$$V(r) = f(r) \frac{1}{k_{s0} \left(d_{\text{vac}} + \frac{d_{\text{semi}}}{\epsilon_{r,\text{semi}}} \right)} V_{\text{tip}}$$

which corresponds to a tip/2DEG capacitor filled with vacuum, with an effective tip-to-2DEG distance close to the tip-to-surface distance (the vertical offset $\frac{d_{\text{semi}}}{\epsilon_{r,\text{semi}}}$ is smaller than 10 nm). This expression would therefore indicate that the tip-induced potential decreases almost linearly with the inverse of the tip distance above the surface in vacuum, but since the dimensionless function $f(r)$ also depends on the tip distance for some capacitance geometries, one needs to know the tip shape to determine the exact dependence on tip distance.

2.4 SGM tips with realistic shapes

Here, we calculate the local capacitance $C(r)$ for different tip geometries. The spatial distribution of the capacitive charge in various tip/surface geometries has been investigated in the past for the purpose of electrostatic force microscopy (EFM). Calculations have been performed for axially-symmetric tips using the equivalent charge model (ECM). This model consists in replacing the metallic tip by a large set of point charges placed along the symmetry axis that collectively give an isopotential surface that coincides with the position of the tip surface. Finding the positions and values of these point charges requires a heavy numerical computation but can be applied to any axially-symmetric tip shapes [133].

Capacitive charge for sphere/plane geometry

Fortunately, an analytical solution exists for these ECM charges in the sphere/plane geometry and a uniform dielectric environment [134]. Their value $q(i)$ and height $h(i)$ above the plane are given by (starting from $i = 0$) :

$$\begin{aligned} q(i) &= 4\pi\epsilon_0 R_{\text{tip}} V_{\text{tip}} \frac{\sinh(y)}{\sinh((i+1)y)} \\ h(i) &= (Z_{\text{tip}} + R_{\text{tip}}) - R_{\text{tip}} \frac{\sinh(iy)}{\sinh((i+1)y)} \end{aligned}$$

where R_{tip} is the radius of the sphere, Z_{tip} is the distance between the plane and the bottom of the sphere, $s = 1 + Z_{\text{tip}}/R_{\text{tip}}$, $y = \ln(s + \sqrt{(s^2 - 1)})$, and assuming $\epsilon_r = 1$. These charges are used to compute the exact potential $V(r, z)$ inside the empty space of the capacitor (see Fig. 2.2) :

$$V(r, z) = \sum_{i=0}^{\infty} \frac{q(i)}{4\pi\epsilon_0} \left(\frac{1}{((z - h(i))^2 + r^2)^{1/2}} - \frac{1}{((z + h(i))^2 + r^2)^{1/2}} \right)$$

and to compute the surface charge density $\sigma(r)$ on the plane :

$$\sigma(r) = \sum_{i=0}^{\infty} \frac{q(i)}{2\pi} \frac{h(i)}{(h(i)^2 + r^2)^{3/2}}$$

This charge density is plotted in Fig. 2.3 (red curves) as a function of r/Z_{tip} , for different sphere radii. It has been normalized by the maximum possible value $\epsilon_0 V_{\text{tip}}/Z_{\text{tip}}$ corresponding to a plane-plane capacitor ($R_{\text{tip}} \rightarrow \infty$). This normalized quantity is the spatial dependence $f(r)$ of the local capacitance introduced above.

For a sufficiently small tip radius compared to the tip distance, an approximate expression can be obtained by assuming that all the point charges are located at the center of the sphere, giving :

$$\sigma(r) = \frac{Q_{\text{tip}}}{2\pi} \frac{(Z_{\text{tip}} + R_{\text{tip}})}{((Z_{\text{tip}} + R_{\text{tip}})^2 + r^2)^{3/2}}$$

This expression corresponds to the solution given at the beginning of this chapter for a single point charge above a metallic plane, but this model further provides the value of the total charge on the tip $Q_{\text{tip}} = \sum_{i=0}^{\infty} q(i)$. The tip charge is proportional to the tip voltage and can be written $Q_{\text{tip}} = C_{\text{tip}} V_{\text{tip}}$ with a total sphere capacitance approximately given by :

$$C_{\text{tip}} = 4\pi\epsilon_0 R_{\text{tip}} + 2\pi\epsilon_0 R_{\text{tip}} \ln(1 + R_{\text{tip}}/Z_{\text{tip}})$$

which is the sum of its self capacitance and its mutual capacitance with the plane [135]. The corresponding function $f(r)$ can be expressed with dimensionless geometrical parameters as :

$$f(r) = \alpha (2 + \ln(1 + \alpha)) \frac{(1 + \alpha)}{((1 + \alpha)^2 + \rho^2)^{3/2}}$$

where $\rho = r/Z_{\text{tip}}$ and $\alpha = R_{\text{tip}}/Z_{\text{tip}}$. Despite the fact that this analytical expression has been derived for small tip radius compared to the tip distance (small α), it is found to be close to the exact calculation for α up to unity (see blue curves in Fig. 2.3) which is sufficient to analyze most of the SGM experiments.

In the limit of small tip radius compared to the tip distance ($\alpha = 0$), the radial extension of the perturbation is simply equal to the tip distance Z_{tip} and its maximum amplitude below the tip is given by the simple expression :

$$V(0) = \frac{2R_{\text{tip}}}{k_{s0} Z_{\text{tip}}^2} V_{\text{tip}}$$

Capacitive charge for cone/plane geometry

The pyramidal part of the tip above the apex also contributes significantly to the charge induced in plane, specially at large radial distance from the apex position. Since the closest axially-symmetric geometry which models this pyramidal part of the tip is a cone, we now consider a cone-plane capacitor with a cone half-angle θ . Unfortunately, the ECM technique has no analytical solution for a cone at finite height above the plane, but fortunately, there is a simple charge distribution that provides a solution for a cone-plane capacitor with zero height, i.e. with a cone apex exactly on the plane. This solution is obtained for a semi-infinite line of charge, placed along the symmetry axis of the tip, starting at $z = 0$, and with a uniform linear charge density :

$$\lambda_{\text{tip}} = 2\pi\epsilon_0 V_{\text{tip}} / \text{arsinh}(1/\tan \theta)$$

Furthermore, moving this semi-infinite charged line at a finite height z_1 above the plane gives an isopotential surface which is rounded at the cone apex. This charge distribution therefore provides a solution for a capacitor formed by a plane and a rounded conical tip with non-zero apex radius, and can be used to model a tip with a realistic shape [133]. The main limitation

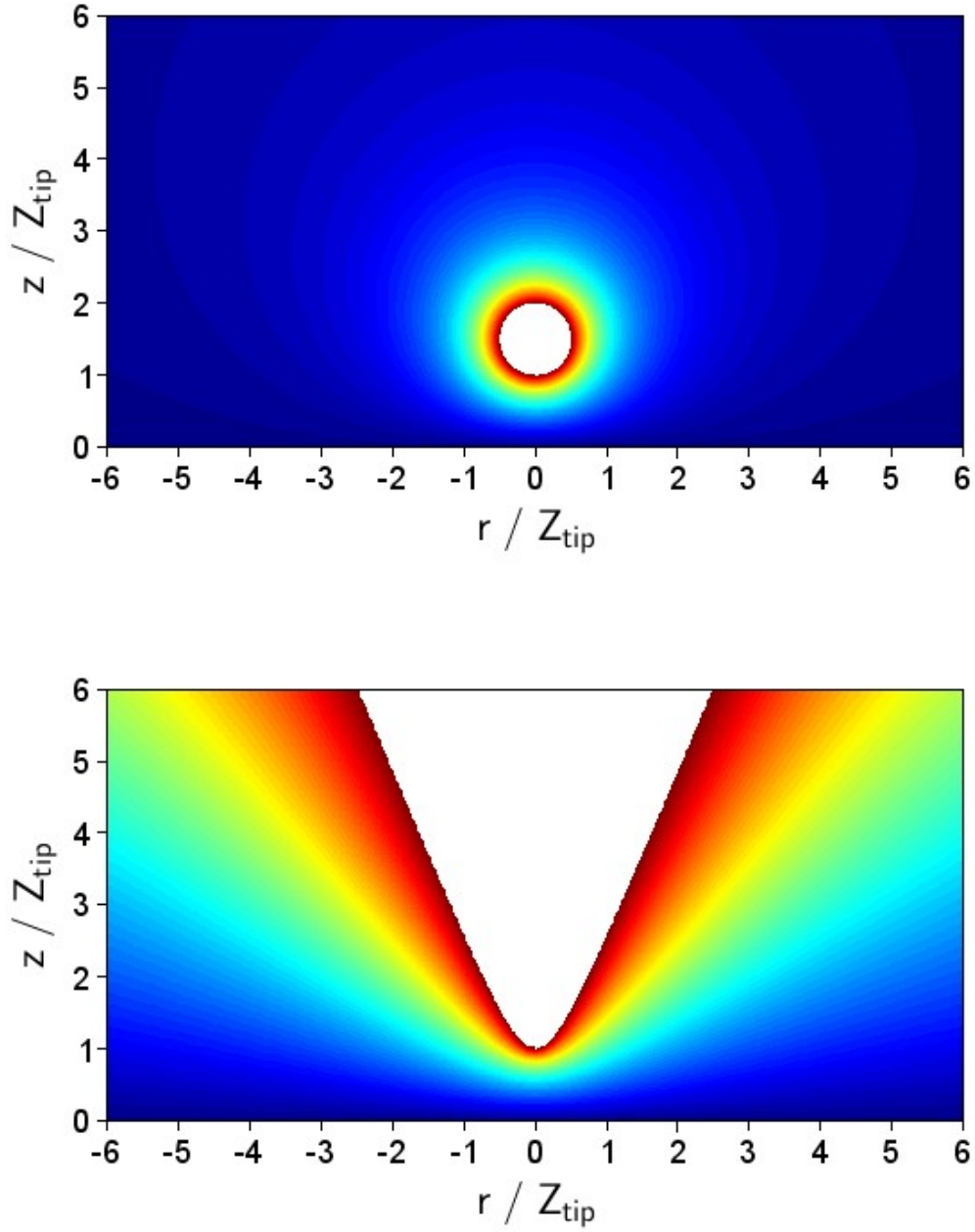


Figure 2.2: Electrostatic potential in a sphere-plane capacitor (top) and a rounded cone-plane capacitor (bottom) calculated with the equivalent charge model (ECM).

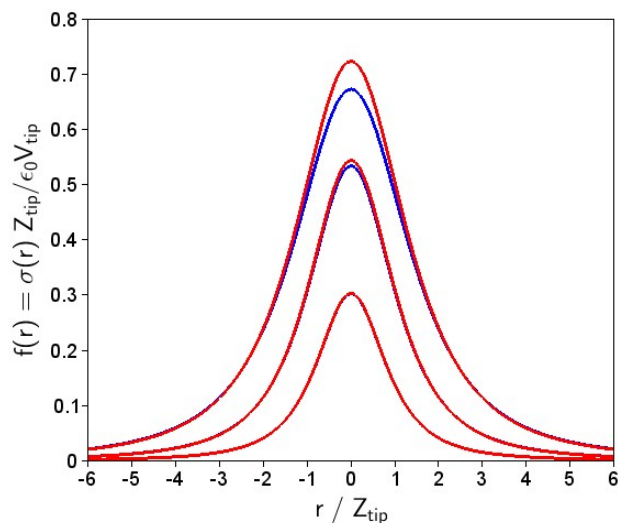


Figure 2.3: Charge distribution on the metallic plane of a sphere-plane capacitor (normalized to the value of the plane-plane capacitor), calculated with the equivalent charge model (red curves) and with the approximate model of a point charge (blue curves). From bottom to top, the sphere radius equals 0.2, 0.5, and 1 in units of the sphere-plane distance.

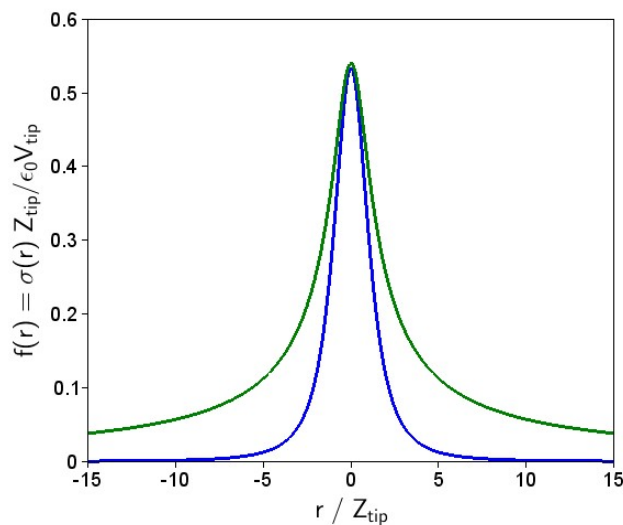


Figure 2.4: Charge distribution on the metallic plane of a rounded cone-plane capacitor (green curve, 20° cone half-angle) normalized to the value of the plane-plane capacitor having the same minimum separation. The influence of the conical gate extends much further away from the gate position than in the case of a spherical gate (blue curve, point-charge model with ratio 0.5 between radius and distance).

of this solution is that the conical surface has an *ideal* apex fixed at $z = 0$, which prevents the calculation of a z -dependence of the contribution coming from the conical surface. The *effective* apex is however at a finite height, that corresponds to the physical distance Z_{tip} when $z_1 = Z_{\text{tip}}\sqrt{1 + \tan^2\theta}$. The potential $V(r, z)$ inside the capacitor (Fig. 2.2) is given by :

$$V(r, z) = \frac{\lambda_{\text{tip}}}{4\pi\epsilon_0} \ln \left(\frac{z_1 + z + \sqrt{(z_1 + z)^2 + r^2}}{z_1 - z + \sqrt{(z_1 - z)^2 + r^2}} \right)$$

and the surface charge density $\sigma(r)$ on the plane has the simple expression :

$$\sigma(r) = \frac{\lambda_{\text{tip}}}{2\pi} \frac{1}{\sqrt{z_1^2 + r^2}}$$

This charge density is plotted in Fig. 2.4 as a function of r/Z_{tip} and has been normalized to the maximum possible value $\epsilon_0 V_{\text{tip}}/Z_{\text{tip}}$ corresponding to a plane-plane capacitor ($\theta \rightarrow \pi/2$). This normalized quantity is the spatial distribution $f(r)$ of the local capacitance introduced above, which can be expressed as :

$$f(r) = \frac{1}{\text{argsh}(1/\tan\theta)} \frac{1}{\sqrt{(1 + \tan^2\theta) + \rho^2}}$$

where $\rho = r/Z_{\text{tip}}$ and θ is the cone half-angle. As opposed to the sphere-plane geometry with $1/r^3$ radial dependence, the local capacitance of the cone-plane geometry has an asymptotic $1/r$ radial dependence, which explains the long-range influence of the tip observed in several SGM experiments. The main perturbation induced by the tip is however sufficiently local to use it as a local probe that influences a region comparable to the tip distance.

For a typical value $\theta = 20^\circ$, the dimensionless function $f(r) = \frac{0.58}{\sqrt{1.06^2 + \rho^2}}$ has a radial extension given by the tip distance Z_{tip} and its maximum amplitude below the tip equals 0.55, such that the maximum induced potential is :

$$V(0) = \frac{0.55}{k_{s0} Z_{\text{tip}}} V_{\text{tip}}$$

This expression can be used to calculate quantitatively the influence of the polarized tip on the 2DEG during SGM experiments.

2.5 Amplitude of the energy change in the 2DEG

We consider here the above case of the cone-plane geometry (or the case of a sphere-plane geometry with $\alpha = 1/2$ which gives the same induced potential below the tip). For a typical tip distance of 50 nm above the surface of a GaAs/AlGaAs 2DEG, i.e. for an effective distance of 58 nm including the 100 nm top layer with dielectric constant 12.7, the induced potential is 2 mV per Volt applied on the tip, so the energy change is 2 meV per Volt. In the GaAs 2DEGs that have been studied, the Fermi energy is about 8 meV, such that a tip voltage of -4 V is necessary to deplete completely the 2DEG below the tip. Experimentally, we found that this GaAs 2DEG is depleted by a tip voltage of -6 V when the tip distance is 50 nm above the surface, which is a slightly larger voltage than expected, but is the correct order of magnitude.

We now estimate the number of charges removed (or accumulated) in the 2DEG by the SGM tip. For the case of a tip modeled by a sphere of radius R_{tip} smaller than the distance Z_{tip} to the 2DEG, the tip capacitance is dominated by the self-capacitance $C_{\text{tip}} = 4\pi\epsilon_0 R_{\text{tip}} = 3$ aF for a typical radius $R_{\text{tip}} = 30$ nm (silicon tip with metallic coating). The charge on the tip is therefore $Q_{\text{tip}} = 20e$ per Volt on the tip, such that 20 elementary charges are removed from the 2DEG for $\Delta V_{\text{tip}} = -1$ V. This calculation shows that SGM (and also EFM) involves a relatively small number of displaced electrons on the tip and in the 2DEG.

Interestingly, the tip-induced energy change $e(2R_{\text{tip}}/k_{s0}Z_{\text{tip}}^2)V_{\text{tip}}$ below the spherical tip corresponds to the product of the number Q_{tip}/e of displaced electrons by a characteristic energy $E_0 = \hbar^2/(2m^*d^2)$. This energy per electron is controlled by the tip distance d which is also the radial extension of the induced perturbation, and can thus be interpreted as a confinement energy inside the perturbed region. For a distance of 100 nm, this characteristic energy per electron is 50 μeV . Since the number of displaced electrons is about 20 per Volt on the tip, the total energy change is about 1 meV per Volt on the tip.

An important result of this analysis is the order of magnitude of the coupling ratio (or lever arm) which is about 1 to 2 meV/V for the energy change in the 2DEG below the tip, in response to the applied voltage on the tip, for standard conditions of SGM experiments.

2.6 Numerical simulations of the tip-induced potential

In the above sections, the tip-induced potential has been calculated for the case of a uniform vacuum medium between the tip and the 2DEG, because there is no analytical model for the case of a 2DEG buried in a semiconductor heterostructure. At first order, the presence of the AlGaAs top layer can be taken into account through the introduction of an effective tip distance $Z_{\text{tip}}^{\text{eff}} = d_{\text{vac}} + \frac{d_{\text{semi}}}{\epsilon_{r,\text{semi}}}$ as explained above. This approximation should give a correct estimate for large dielectric constant (here $\epsilon_{r,\text{semi}} \approx 12$) since the effective thickness of the semiconductor top layer is then very small, and the electrostatic solution is then almost the same.

However, it is interesting and sometimes necessary to calculate the exact solution by numerical calculations based on finite element methods. This numerical approach can be used to treat correctly the presence of the dielectric layers with their specific dielectric constants and the precise shape of the tips used in the experiments. It is also necessary to treat non-linear screening situations where the local capacitance model is not valid any more. It can be the case for large tip voltages that create a local depletion in the electron system : this is a frequent situation in SGM experiments. It can also be the case if the screening level in the 2DEG is too small to ensure a small induced potential compared to the voltage applied on the tip : this situation may occur for 2DEGs with small DOS, and thus small screening wave vector, where $1/k_{s0}$ is larger than the radial extension of the induced potential (of the order of the tip distance).

As explained in the first section of this chapter, calculations beyond the Thomas-Fermi approximation would require to solve the self-consistent Schrödinger-Poisson equations which is a very complicated problem. For this reason, we keep here the Thomas-Fermi approximation which is valid when the Fermi wavelength is much smaller than the spatial variations of the potential. Such classical electrostatic simulations can be performed with commercial softwares such as COMSOL, or with free softwares such as MaxFEM. This free software (developed by a university in Spain) solves several physical problems by finite element methods, including the 3D electrostatic problem that we are considering here. The code solves the Poisson equations in a finite volume of space containing different objects and materials. We modified this software to calculate the self-consistent electrostatic potential in a semiconductor 2DEG (or an encapsulated graphene device) in presence of one or several surface gates defining for example quantum point contacts or quantum dots. We use it here to analyze the potential induced by the SGM tip in the 2DEG for a real semiconductor heterostructure.

For a semiconductor 2DEG with a constant density of states $\text{DOS} = \frac{m^*}{\pi\hbar^2}$, the local charge density in the 2DEG plane is related to the local potential $V(\vec{r})$ by the relation :

$$\sigma(\vec{r}) = -e \text{DOS} \times \max(0, E_{\text{F}} + eV(\vec{r})) + e N_{\text{ion}}$$

The first term is the potential-dependent negative charge density of the electrons in the conduction band, with a Fermi energy E_{F} , which cannot go below zero. The second term is a constant, uniform, positive charge density corresponding to the ionized dopants, that exactly

neutralize the electrons charges in the unperturbed situation. This formulation assumes that the dopants are in the 2DEG plane, which is not the case in high-mobility heterostructures where the doped region is separated from the 2DEG by an un-doped spacing layer. Since this positive charge density is fixed and uniform, this vertical shift should have little effect on the electron distribution.

The self-consistent solution is computed iteratively, starting from the uniform neutral charge distribution, and calculating a new charge distribution at each iteration, until it converges on the self-consistent solution. To avoid divergence or instability, the new charge density should be calculated at each iteration by mixing the previous charge density with only a small fraction of the charge density calculated from the electrostatic potential with the above relation. For a mixing fraction of 1%, the convergence is obtained after about 200 iterations (small residual oscillations are then suppressed by reducing even more the mixing fraction).

Figure 2.5 shows an example of numerical simulation, with a rounded conical tip at 60 nm above the top surface of a GaAs/AlGaAs heterostructure hosting a 2DEG at 100 nm below the surface. The equipotential lines in Fig. 2.5b are concentrated in the vacuum region above the AlGaAs top layer, due to the large dielectric constant $\epsilon_{r,\text{semi}} = 12$ of this material compared to vacuum. This effect justifies the introduction of an effective distance in the analytical models to provide a first-order estimate for the amplitude of the tip-induced potential. The tip-induced potential variations in the 2DEG are not visible on the colorplot because the screening effect of the 2DEG is very large and the potential variations are thus very small. The maximum energy change in the 2DEG is indeed only 1 meV for -1 V on the tip as shown in Fig. 2.5c (red points). It decreases rather slowly in the radial direction due to the long-range influence of the conical tip. The red line shows a comparison with the analytical model (see section 2.4) of a rounded cone with the same characteristic dimensions placed at an effective distance $d_{\text{vac}} + \frac{d_{\text{semi}}}{\epsilon_{r,\text{semi}}} = 68$ nm. There is a good agreement between the analytical and numerical results at intermediate and large distances, but the maximum value just below the tip is overestimated by the analytical model, which shows the importance of numerical simulations to get precise values for the amplitude of the tip-induced potential. The effect of the large (Al)GaAs dielectric constant can be visualized by comparison with the same simulation performed for a semiconductor dielectric constant $\epsilon_{r,\text{semi}} = 1$ (grey points) and with the corresponding model of a rounded cone placed at a distance $d_{\text{vac}} + d_{\text{semi}} = 160$ nm (grey line) which show lower induced potentials.

Simulations for different tip voltages confirm that the induced potential is proportional to the tip voltage (linear screening), until it overcomes the Fermi energy, as shown in Fig. 2.5d for -10 V on the tip (non-linear screening), creating a small depletion disk below the tip. Interestingly, the portion of the curve which is below the Fermi energy follows closely the linear-screening solution calculated for this tip voltage. The diameter of the depleted region (here 200 nm) can thus be calculated by finding the positions where the linear-screening solution reaches the Fermi energy.

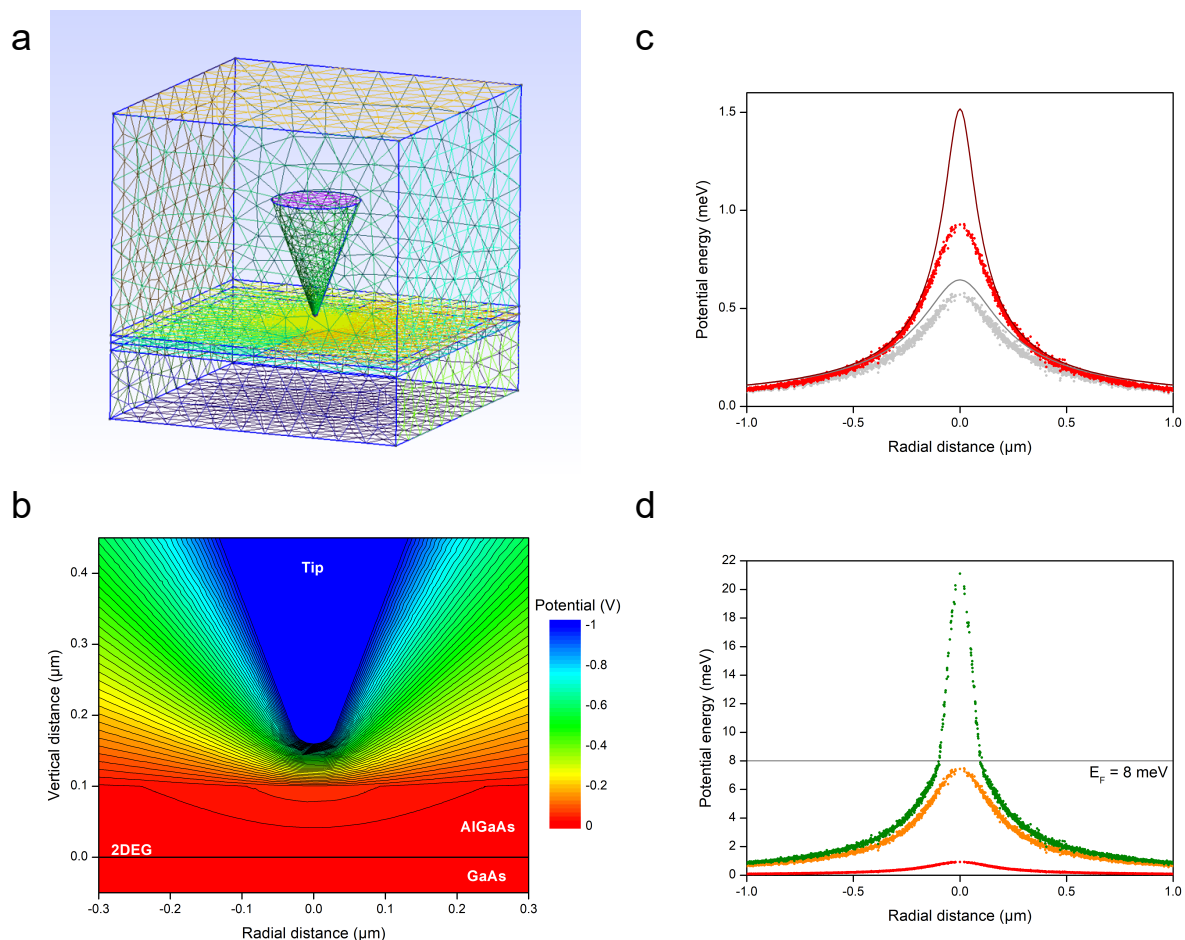


Figure 2.5: (a) Model geometry used to simulate the effect of the SGM tip on the 2DEG. The mesh computed with Gmsh is then used by MaxFEM to solve the Poisson equations by a finite element method. The mesh is $4 \times 4 \times 4 \mu\text{m}^3$. The 2DEG is at the interface between a GaAs substrate and a 100 nm AlGaAs top layer, both with a dielectric constant $\epsilon_r = 12$. The Fermi energy of the 2DEG is 8 meV, corresponding to an electron density of $2.5 \times 10^{11} \text{ cm}^{-2}$. The SGM tip is a 20° half-angle cone, terminated by a 30 nm radius spherical apex, and surrounded by vacuum. The tip apex is 60 nm above the AlGaAs top surface. (b) Self-consistent solution of the electrostatic potential in the space between the tip and the 2DEG, for a tip voltage of -1 V. The equipotential lines are separated by 20 mV. (c) Red points : tip-induced energy change in the 2DEG plane for the same parameters as in panel (b). Red line : analytical model for a rounded cone with the same dimensions and an effective tip distance of 68 nm. Grey points : result obtained when setting $\epsilon_r = 1$ in all the computational volume. Grey line : analytical model for a tip distance of 160 nm. (d) Tip-induced energy change in the 2DEG plane for tip voltages of -1 V (red), -8 V (orange) and -10 V (green). For the last value, the induced energy change overcomes the 8 meV Fermi energy and creates a depletion area.

Chapter 3

SGM investigations of InGaAs quantum rings

We started the SGM activity in Grenoble in 2005, a few years after this technique had been invented in UK and USA. This technique was not used by any other group in France at that time, and it is still the case today. It is important to realize that SGM is a complex technique that requires the cooperation of different groups with complementary expertise, and such a specific situation happened in 2005 in France/Belgium when three teams decided to work together to start an SGM activity : the team of Xavier Wallart at IEMN in Lille for the fabrication of high-mobility 2DEGs by epitaxial growth of III-V heterostructures, the team of Vincent Bayot at UCL in Louvain-la-Neuve for the fabrication of nanostructures and transport measurements, and the team of Serge Huant at Spectro Lab in Grenoble for the development of scanning probes at low temperature. This cooperation has been the starting point of a fruitful collaborative work, which is still going on today, with two SGM apparatus, one in Grenoble and one in Louvain-la-Neuve. In addition, this collaboration between experimentalists has been extended to include theoreticians, with the team of Marco Pala who was working at IMEP in Grenoble at that time. His expertise on numerical simulations of quantum transport in nanostructures was of great help to prepare and analyze the SGM experiments.

The first topic that we addressed was the physics of quantum rings [6, 7, 8, 9] which had not been investigated by SGM before. In quantum rings, wave function interferences around the central anti-dot give rise to quantized eigenstates with a discrete energy spectrum. This interference is sensitive to the magnetic flux through the ring due to an additional quantum phase accumulated after each turn around the ring. This Aharonov-Bohm (AB) effect produces periodic oscillations of the conductance as a function of magnetic field with a periodicity inversely proportional to the ring area. The first idea that comes to the mind is to use SGM to image the interference pattern *in real space*, whereas transport experiments probe the periodicity of the energy spectrum *in the reciprocal space* by varying, for example, the Fermi energy. In practice however, the spatial extension of the tip-induced perturbation is

broader than the electron wave length, and it is not possible to image directly the interference pattern of the wave function by SGM. Nevertheless, SGM can be used to change locally the electrostatic potential along the ring, which influences the interference effect by the so-called electrostatic AB effect. It is therefore an *indirect* probe of the quantum interference in the ring. SGM can also reveal the spatial variations of the electronic density of states on scales much larger than the Fermi wave length due to the presence of bound states or induced by the potential disorder.

The second topic that we investigated by SGM was the transport through nanostructures in the quantum Hall regime [13, 14, 15]. Thanks to a new SGM instrument developed in Louvain-la-Neuve by Benoit Hackens and placed in a dilution fridge, we studied the same quantum ring devices as above, but in large perpendicular magnetic fields and at much lower temperature. In this regime, the anti-dot of the ring forms a quantum Hall Coulomb island which is tunnel coupled to the quantum Hall edge channels flowing along the sample edges. In practice however, the observed pattern of magneto-resistance oscillations is much more complicated than the one predicted for a single quantum Hall Coulomb island located around the anti-dot. To understand the origin of this complex behavior, we performed SGM experiments and discovered that not only the anti-dot could give rise to such oscillations, but also unwanted potential hills that exist in the 2DEG due to unwanted charges at the surface or in the heterostructure. This observation explains the origin of the complex patterns of magneto-resistance oscillations which are often observed in nanostructures in the quantum Hall regime. This study shows the importance of using a scanning probe technique to understand a complex phenomenon, by providing real space images of this phenomenon.

The third topic was an investigation, at zero magnetic field, of a specific geometry of nanostructure forming an asymmetric network, to search for the existence of a counter-intuitive effect analogous to the Braess paradox, described initially for road networks and then extended to several other domains such as electricity and mechanics. In these particular networks, a better *transmission* is obtained when one channel of the network is suppressed, which is counter-intuitive. In quantum nanostructures, we found the conditions to obtain a similar effect by performing quantum transport simulations of networks made of double quantum rings with three parallel arms connected asymmetrically to the source and drain reservoirs [18, 19]. We performed the experiment using the SGM tip to control the transmission of the central arm, and we found a weak signature of this Braess-like effect. The difficulty of the experiment is to distinguish this effect from the interference and localization effects which also give rise to variations of the transmission. To address this problem, we studied in detail the localization effects that arise in narrow quantum wires at low density, using SGM to reveal the position of the potential hills responsible for the localization [21]. More recently, we studied the interference effects that arise in the arms of the network, using SGM to tune the potential of the central arm and separate the different phenomena at play in the network [20].

3.1 Device properties

In these studies, the 2DEG is confined in an InGaAs quantum well, where the electrons have a low effective mass and a high mobility. The semiconductor heterostructures are grown by molecular beam epitaxy at IEMN (Lille) by Xavier Wallart and Ludovic Desplanque. Initially, the layers were grown on undoped InP substrates (which are insulating at low temperature) with the following sequence :

400 nm	In ₅₂ Al ₄₈ As	buffer layer (lattice-matched on InP)
15 nm	In ₇₀ Ga ₃₀ As	channel layer (strained)
10 nm	In ₅₂ Al ₄₈ As	spacer layer
0 nm	Si dopants	doping plane ($4.5 \times 10^{12} \text{ cm}^{-2}$)
15 nm	In ₅₂ Al ₄₈ As	barrier layer
7 nm	In ₅₃ Ga ₄₇ As	cap layer (highly-doped)

By a charge transfer process, the free electrons of the silicon dopants populate the In₇₀Ga₃₀As quantum well, which has a smaller gap ($E_g = 0.6 \text{ eV}$) than the surrounding In₅₂Al₄₈As barriers ($E_g = 1.5 \text{ eV}$). These free electrons form a 2DEG located at 25 nm below the surface (the 7 nm cap layer is removed at the end of the device fabrication). With these values of thickness and doping, the electron density in the 2DEG is $2 \times 10^{12} \text{ cm}^{-2}$ and the electron mobility at 4.2 K is about $100\,000 \text{ cm}^2\text{V}^{-1}\text{s}^{-1}$ corresponding to a mean free path of about $2 \mu\text{m}$.

Later, n-doped InP substrates were employed in order to use the substrate as a back-gate and vary *in-situ* the electron density during the experiment. With the above layer sequence, we found a large leakage current from the back-gate to the 2DEG, even at small back-gate voltage. The reason was probably the insufficient barrier height produced by the 400 nm In₅₂Al₄₈As layer, since the gap of the InP substrate ($E_g = 1.4 \text{ eV}$) is close to that of this barrier ($E_g = 1.5 \text{ eV}$). The solution was to incorporate a layer of AlAsSb with a larger gap ($E_g = 1.9 \text{ eV}$) inside the bottom In₅₂Al₄₈As barrier with the following sequence :

100 nm	In ₅₂ Al ₄₈ As	buffer layer (lattice-matched on InP)
100 nm	AlAs ₅₆ Sb ₄₄	buffer layer (lattice-matched on InP)
400 nm	In ₅₂ Al ₄₈ As	buffer layer (lattice-matched on InP)
15 nm	In ₇₅ Ga ₂₅ As	channel layer (strained)
20 nm	In ₅₂ Al ₄₈ As	spacer layer
0 nm	Si dopants	doping plane ($2.5 \times 10^{12} \text{ cm}^{-2}$)
15 nm	In ₅₂ Al ₄₈ As	barrier layer
7 nm	In ₅₃ Ga ₄₇ As	cap layer (highly-doped)

In these heterostructures, the electron density can be varied from 10^{11} to 10^{12} cm^{-2} by applying a few volts (positive or negative) on the back-gate.

Different nanostructures have been fabricated with ring shapes to study the Aharonov-Bohm effect and other effects. The fabrication is carried out in Louvain-la-Neuve by Benoît Hackens. It consists in three steps : (1) e-beam lithography of alignment marks and metal deposition of Ti/Au by evaporation, (2) e-beam lithography of insulation trenches that define the nanostructure and wet etching in $\text{H}_3\text{PO}_4/\text{H}_2\text{O}_2/\text{H}_2\text{O}$, (3) e-beam lithography of contacts pads, metal deposition of Ni/Ge/Au/Ni/Au by evaporation, and annealing at 315°C .

I also initiated a fabrication process in Grenoble using the facilities of the Plateforme Technologique Amont (PTA). To obtain a better control of the nanostructure shape and dimension, we replaced the wet etching by a reactive ion etching (RIE). Since there was no chlorine-based RIE machine at the PTA at that time, we used a specific machine at the CEA/LETI/DOPT to etch the InGa(Al)As compounds with SiCl_4 mixed with Ar. The devices were working correctly, but we observed the presence of residues along the edges of the trenches, several tens of nanometers in height, which were problematic for SGM experiments. The continuation of this work had to wait for the installation of a chlorine-based RIE machine at PTA, which happened a few years later, but the fabrication process has not been restarted.

Fig. 3.1 shows electron microscope images of typical samples produced in Louvain-la-Neuve and of the very few samples made in Grenoble. Note that these devices have no metallic top gate, but some of them have lateral gates patterned in the 2DEG plane, which are used to tune the electrostatic potential in the near-by channel.

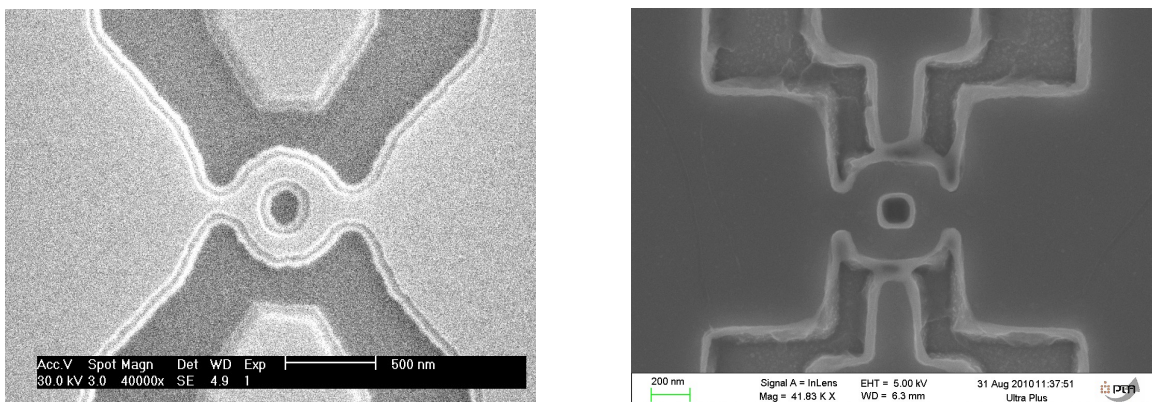


Figure 3.1: Quantum rings fabricated in Louvain-la-Neuve (left) and Grenoble (right).

In these InGaAs/InAlAs heterostructures, the electron mean-free path is typically $2 \mu\text{m}$ at low temperature, so that the electron transport is in the ballistic regime in all our devices. The coherent nature of transport in the quantum rings is revealed by the observation of periodic magneto-conductance oscillations. The coherence length extracted from these oscillations exceeds $1 \mu\text{m}$ at 4.2 K (and much more at lower temperature) such that the transport is coherent in the ring-shaped devices for at least one turn of the electrons around the ring.

3.2 Aharonov-Bohm effect

An open quantum ring (QR) in the coherent regime of transport is the simplest type of electron interferometer. At the entrance of the ring, the incoming electron wave splits naturally into two parts, without the necessity to engineer a complex beam-splitter as in other types of interferometers. Each part propagates in a separate branch of the ring, accumulating a phase which depends on the local electrostatic potential and on the local magnetic vector potential. At the exit of the ring, the two partial waves can interfere constructively (high transmission) or destructively (low transmission). The interference state can be tuned by varying either the magnetic flux enclosed by the ring, or the electrostatic potential difference between the two arms. This tuning by external fields gives rise to the magnetic and electrostatic Aharonov-Bohm (AB) oscillations in the conductance :

$$\delta G = G_{AB} \cos(\Delta\phi)$$

where $\Delta\phi = eBS/\hbar$ or $\Delta\phi = e\Delta V t/\hbar$ for the magnetic and electrostatic cases respectively, S being the ring area and t the traveling time along one arm.

In the above description however, two important effects have been neglected. First, the electron waves can make several turns around the loop before interfering in the output of the ring. This effect becomes important when the coherence length is several times the ring perimeter and gives rise to harmonics in the AB oscillations. It also explains why usually non-symmetric rings with different arm lengths always show symmetric conductance oscillations around $B = 0$ as required by the Onsager relations for the two-probes conductance. Second, the propagation along the arms of the ring is usually not one-dimensional, but involves several transverse modes. Since each mode has a slightly different effective perimeter, and thus a different period in magnetic field, the amplitude of the AB oscillations decreases with the number of modes.

Although these effects have been studied extensively through transport measurements, those techniques cannot probe the spatial properties of the AB interference. In this work [6], we use scanning gate microscopy (SGM) to perturb locally the propagation of the electrons through the QR with the tip of an atomic force microscope (AFM). We therefore take advantage of both the high-resolution imaging capabilities of the AFM and the high sensitivity of the conductance measurement to electron phase changes. When the tip scans outside the QR, the electrostatic AB effect induced by the polarized tip gives rise to a well-developed fringe pattern in the SGM conductance image (Fig. 3.2). This outer pattern is mainly concentric with the ring geometry. The qualitative interpretation in terms of a scanning-gate-induced electrostatic AB effect is the following. As the tip approaches the QR from the left, the electrostatic potential mainly increases on the left side of the QR. This potential change induces a phase difference between electron wave-functions traveling through the two arms of the ring, which produces the observed pattern of concentric circles. Since the magnetic field contributes another phase term through the magnetic AB effect, varying the field shifts the phase of the concentric oscillations. This displacement is periodic in magnetic field, with

the same periodicity as the AB oscillations seen in the magneto-conductance measurements, which gives further support to the interpretation in terms of AB effects. In addition, we measured the SGM contrast versus temperature in the range 3 to 40 K and observed the same evolution as in the magneto-conductance measurements.

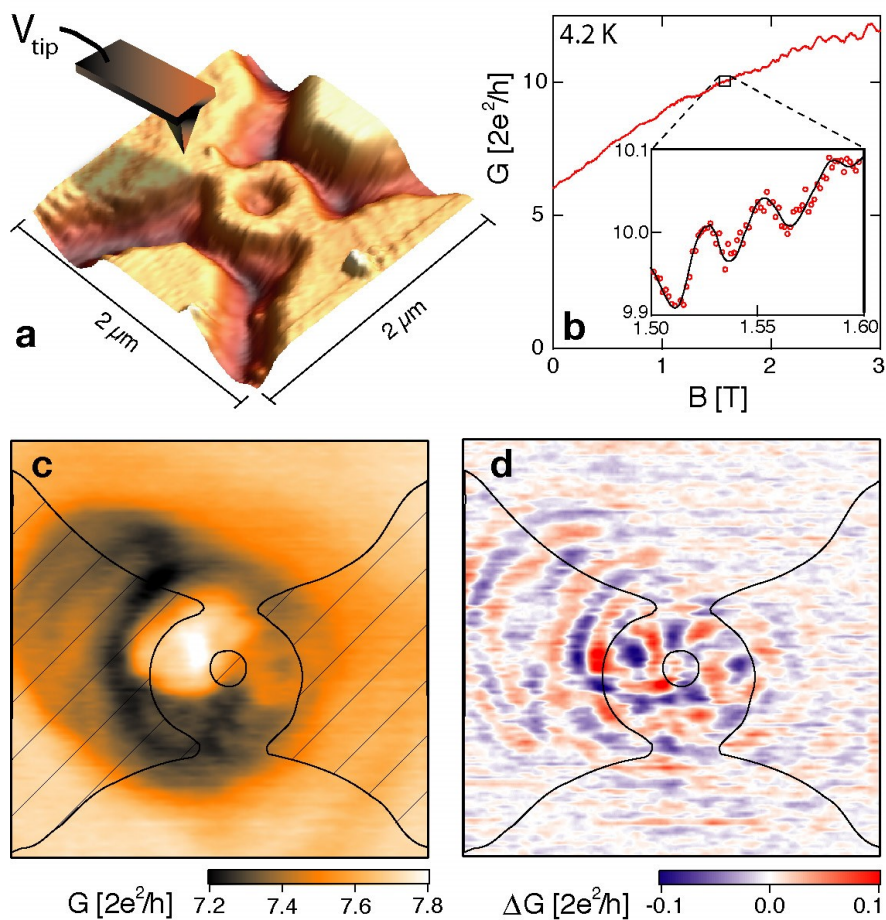


Figure 3.2: (a) Topography of a quantum ring patterned in an InGaAs 2DEG. The drawing shows schematically the SGM tip which applies a local gate effect on the device. (b) Conductance of the ring as a function of the magnetic field at 4.2 K showing periodic h/e Aharonov-Bohm oscillations below 2 T. The oscillations are weak because several transverse modes propagate along the QR arms. (c) Conductance of the ring as a function of tip position with $V_{\text{tip}} = 0.3\ \text{V}$, $d_{\text{tip}} = 50\ \text{nm}$ and $B = 2\ \text{T}$. Weak fringes are superimposed on a stronger background. (d) High-pass-filtered conductance map revealing the weak fringes. Figure reprinted from [6].

3.3 Local density of state

Here we discuss the possibility for SGM to directly image the local density of states (LDOS) inside a nanostructure, i.e. the square modulus of the electron wave functions. When applied to QRs, the question is to determine the conditions in which the tip-induced perturbation can reveal the maxima and minima of the interference along the QR arms.

In our experiments on QRs [7], when the SGM tip scans directly over the QR arms, the SGM conductance images exhibit a complex pattern of oscillations, forming radial stripes which are not equidistant along the QR arms (Fig. 3.3). This pattern is unchanged when the tip voltage is varied, but kept below a certain threshold, which indicates that the perturbative action of the tip does not modify the spatial distribution of the LDOS. The observed linear increase of the SGM signal with the tip voltage is consistent with this interpretation. On the other hand, when the tip voltage exceeds a certain threshold, the amplitude of the SGM signal saturates, and the pattern of oscillations deviates significantly from the low-voltage case. Note that this limitation to low tip voltages holds only for experiments aiming at measuring the unperturbed electronic properties of the electron system such as the LDOS, as opposed to scattering experiments where the SGM tip is used to back-scatter the electron waves in the 2DEG and image the electron trajectories (see chapter 4).

Numerical analysis have been performed, based on quantum mechanical simulations of the electron probability density, including the perturbing tip potential, the magnetic field and the presence of randomly distributed impurities [9]. The simulations are able to reproduce the main experimental features and demonstrate the relationship between SGM conductance maps and electron probability density maps at the Fermi level. An example of such a relationship is shown in Fig. 3.3 in the case of a realistic QR with negatively charged impurities. The distortions induced by the impurities are reproduced in the SGM image, provided that the perturbation induced by the tip is small enough in amplitude and narrow enough in space. As seen in the figure, both the LDOS map and the SGM image tend to develop radial fringes, which are related to the impurity locations. This complex pattern of fringes is reminiscent of the experimental SGM images that are often found to be asymmetric.

A simple analytical model for a single transport channel can be used to relate the tip-induced conductance change and the local density of states [8]. At first order in the perturbation strength U_{tip} and for a spatial extension σ smaller than the Fermi wavelength, the conductance change when the tip is at position x is proportional to the real part of the local retarded Green's function at the Fermi energy E_F . Since the LDOS at position x is given by the imaginary part of the same local retarded Green's function, the Kramers-Kronig relation between the the real and imaginary parts shows that the conductance change is simply proportional to the Hilbert transform of the LDOS :

$$\frac{\Delta G}{G}(x) = 2 U_{\text{tip}} \mathcal{P} \int \rho(x, E) \frac{1}{E_F - E} dE$$

where \mathcal{P} stands for the Cauchy principal part. This relation corresponds to applying a filter on the LDOS spectrum that selects the states closest to the Fermi level. The sign of the

conductance change is determined by both the sign of the perturbing potential U_{tip} and the relative position of the dominant energy level with respect to the Fermi level.

In the multi-channel transmission case, a simple correspondence between LDOS and SGM maps is not possible due to the uneven effect of the tip on the different transverse modes involved in the transport. However, a noticeable correspondence can be achieved when the total wave function is determined only by the few states close to the Fermi energy. This is the case when the LDOS is dominated by semi-classical periodic orbits inducing scarring effects in the total wave function.

The above discussion suggests that, in certain conditions, SGM can be viewed as the analogue of STM for imaging the electronic LDOS at the Fermi level in 2DEG nanostructures buried under an insulating layer and thus not accessible to STM. The main limitation is the spatial resolution of the perturbing potential, which is limited by the vertical distance between the tip and the 2DEG.

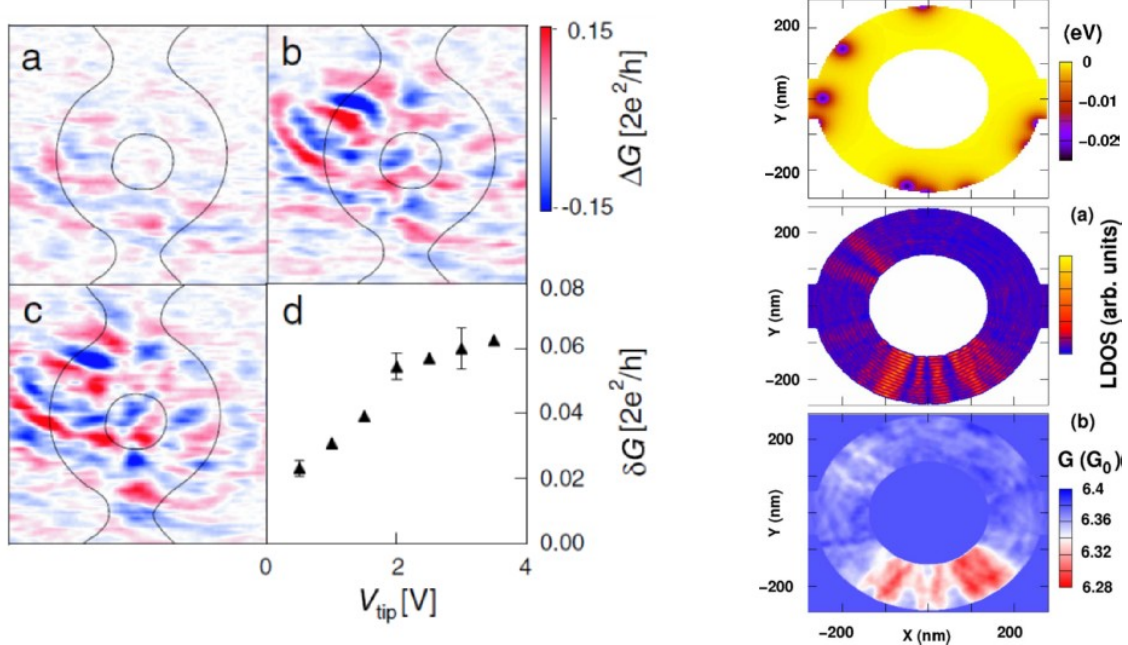


Figure 3.3: (left) SGM conductance maps of a quantum ring recorded with $V_{\text{tip}} = 0.5$ V (a), 2.5 V (b), 3.5 V (c), for $d_{\text{tip}} = 50$ nm and $B = 2$ T. (d) Amplitude of the SGM signal versus tip voltage. Figure reprinted from [7]. (right) Numerical simulation showing the correspondence between the local density of states (LDOS) and the SGM conductance map (G) in presence of charged impurities mainly localized around the border of the ring. The perturbation induced by the SGM tip is modeled by a potential $U(r) = U_{\text{tip}}/(1 + r^2/\sigma^2)$ with $U_{\text{tip}} = E_F/100$ and $\sigma = 5$ nm. Figure reprinted from [8].

3.4 Coulomb islands in the quantum Hall regime

In large perpendicular magnetic field, the cyclotron motion is quantized, and the energy spectrum is composed of equally spaced Landau levels. The number of occupied levels is determined by the electron density and characterized by the filling factor ν . In the quantum Hall regime, electrons are transported in ν ballistic channels flowing along the edges of the 2DEG in a single direction (chiral transport) with a zero longitudinal resistance.

When the 2DEG forms a narrow constriction between the source and drain contacts, electrons can tunnel between the edge channels flowing in opposite directions on the opposite sides of the sample. This electron tunneling produces back-scattering and results in a finite longitudinal resistance. If an anti-dot is etched in the middle of a wide constriction, the back-scattering is the result of two successive tunneling events, from the sample edge to the anti-dot, and then from the anti-dot to the opposite sample edge (Fig. 3.4a). Since the edge channels form closed loops around the anti-dot, their motion around the anti-dot is quantized, and the resulting energy levels are sensitive to the enclosed magnetic flux with an Aharonov-Bohm period $\Delta B_{AB} = \phi_0/A$ inversely proportional to the area A of the anti-dot. When the magnetic field is varied, the quantum states encircling the anti-dot change size, which creates a charge imbalance in the region close to the anti-dot, equal to one elementary charge per additional flux quantum. The incompressible region between the anti-dot and the sample edges is not able to screen this charge imbalance and acts as a barrier responsible for Coulomb blockade of the charges encircling the anti-dot. The charge imbalance is relaxed by the tunneling of an electron from the sample edge channels thereby increasing the conductance through the anti-dot. For ν edge channels encircling the anti-dot, ν electrons will tunnel for each additional flux quantum. The magneto-resistance thus shows periodic oscillations versus magnetic field with a period $\Delta B = \Delta B_{AB}/\nu$ [137, 136]. A similar effect occurs in cavities forming quantum Hall interferometers where charging effects appear in the bulk part of the cavity [138].

Experimentally, these sub-periodic AB oscillations appear not only in anti-dot devices fabricated on purpose, but also in mesoscopic Hall bars without any hole inside. A possible origin of these oscillations can be spatial fluctuations of the electrostatic potential in the 2DEG, due to the remote ionized dopants, which create local potential hills similar to anti-dots. The objective of our work was to investigate this effect using the SGM technique to locate the presence of such quantum Hall islands (QHI) and to probe their properties. In order to have a reference with a controlled geometry, we studied a device patterned by etching with both constrictions and anti-dot, in fact a quantum ring similar to those discussed in previous sections (Fig. 3.4b).

In some ranges of magnetic field, this device did show the expected sub-periodic AB oscillations in transport measurements, and we thus carried out SGM experiments to check if these oscillations really come from charging effects around the anti-dot. The measurements have been performed at filling factor $\nu = 6$ in a range of magnetic field where the oscillations have a period $\Delta B_{AB}/6$ (Fig. 3.4c-e). The SGM images reveal a set of concentric circles,

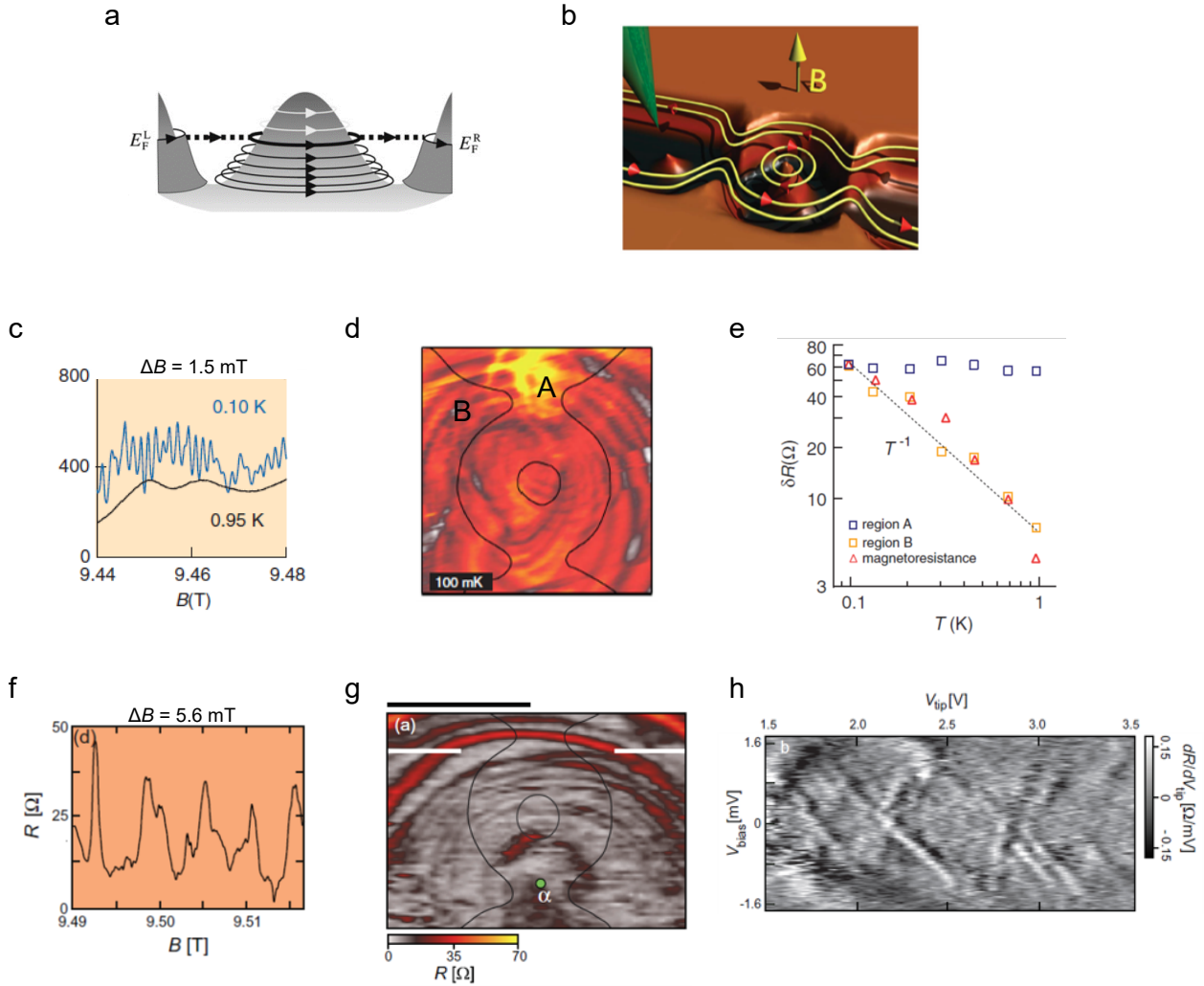


Figure 3.4: (a) Electron tunneling through the discrete levels of a QH island around an anti-dot in the case of a single Landau level [136]. (b) Schematic of the SGM experiment (green tip) on a quantum ring forming a cavity with a central anti-dot. (c) Magneto-resistance oscillations of the quantum ring in the $\nu = 6$ QH plateau at 100 mK. The period $\Delta B = 1.5$ mT equals $1/\nu$ times the low-field Aharonov-Bohm period $\Delta B_{AB} = 9$ mT. (d) These oscillations form concentric rings in the SGM maps (red fringes of type B) and are centered on the quantum ring anti-dot. (e) The $1/T$ temperature dependence is the same for the red SGM fringes in (d) and the magneto-resistance oscillations in (c) which indicates a common origin. (f) Magneto-resistance oscillations with a larger period $\Delta B = 5.6$ mT corresponding to a QH islands with a smaller area. (g) SGM maps reveals that the island responsible for the oscillations in (f) is located in the bottom constriction. (h) Source-drain spectroscopy of these oscillations reveals Coulomb blockade diamonds with a charging energy around 1 meV. Data reprinted from [13] and [14].

centered on the anti-dot, corresponding to the sub-periodic AB oscillations observed in the transport measurements, and with the same temperature dependence, confirming the anti-dot origin of these oscillations [13].

In the same device but in different ranges of magnetic field, we observed other sets of concentric circles in the SGM images, circles which are not centered on the anti-dot and which show larger magnetic-field periods (Fig. 3.4f-h). These oscillations could come from small QHI induced by potential fluctuations in the 2DEG. The presence of several of such QHI in a device generate a complex pattern of oscillations which cannot be understood in standard transport experiments. The SGM appears therefore as a unique technique to understand the origin of such complex magneto-conductance oscillations in mesoscopic quantum Hall systems. We further studied the properties of these disorder-induced QHI by source-drain bias spectroscopy across the QHI. We could extract quantities such as charging energy, edge state velocity, and bias-dependent dephasing rate [14, 15].

3.5 Mesoscopic Braess paradox

The Braess paradox is a counter-intuitive behavior which was first described in the context of road networks. Adding a new road to a congested network can paradoxically lead to a deterioration of the overall traffic situation, i.e. longer trip times for road users. This paradox was later extended to other networks in classical physics, such as mechanical or electrical networks, where adding extra capacity to a congested network can counter-intuitively degrade its overall performance. Initially known for classical networks only, we have extended the concept of the Braess paradox to quantum devices with particular network geometries.

In this study [18], we considered a simple network made of three narrow wires connected to source and drain reservoirs via two large openings, such that the narrow wires behave as congested constrictions for propagating electrons (Fig. 3.5). The dimensions are chosen to ensure that the device is in the ballistic and coherent regime of transport at 4.2 K. To search for the existence of a Braess-paradox effect, we used the SGM gating effect to partially block the transport through the central branch. Doing so should intuitively result in a decreased current transmitted through the device, but in certain conditions, we observed the opposite behavior, which can thus be called a Braess paradox (red curve in panel d).

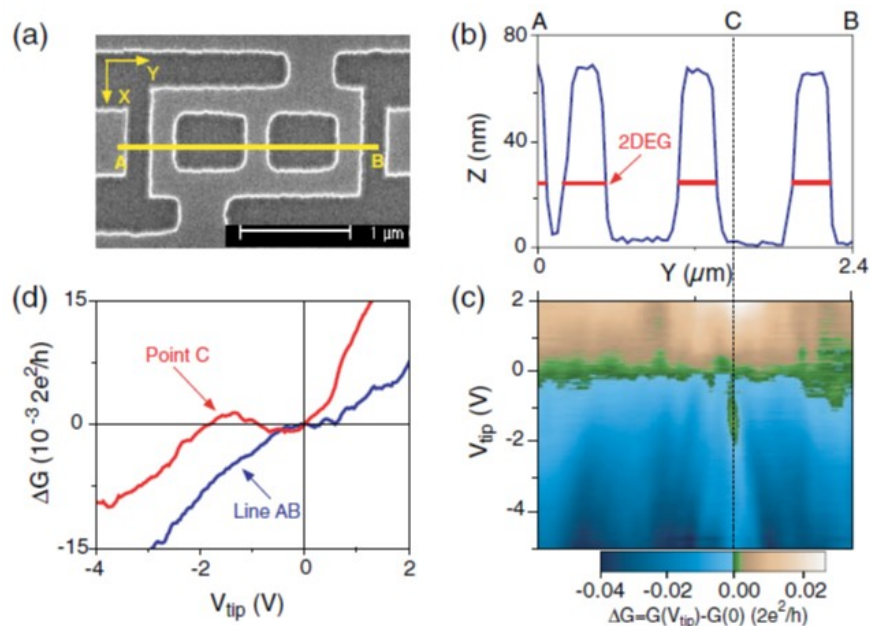


Figure 3.5: (a) Electron microscope image of the mesoscopic network. (b) AFM topography along the AB line. (c) Conductance change versus tip voltage when the tip is at position C in red and its average value over the AB line in blue. (d) Colorplot of the same data showing the narrow region C where the anomalous conductance change is observed. Data reprinted from [18].

To analyze the origin of this effect, we performed quantum simulations of the device transmission in presence of the tip (Fig. 3.6). By plotting the current density maps in different configurations, we found a possible explanation of the effect in terms of semi-classical trajectories in the network. The simulation shows that depleting the central arm (panel c) increases the current flow throughout the structure in comparison with the unperturbed situation (panel b). Some trajectories use first the lateral arms to go forward, and then the central arm to go backward instead of escaping the network. This phenomenon is a sort of localization effect imposed by the network geometry and can be compared to localization effects in an infinite system due to the presence of scatterers. This effect has a much larger amplitude than the universal conductance fluctuations which are also present as a function of tip position. On the other hand, closing one of the lateral arms (panel a) reduces the current flow, which stresses the particular role played by the central branch in this particular asymmetrical geometry. An additional experimental work [20] has then examined in more details the role played by quantum interference in the paradoxical effect.

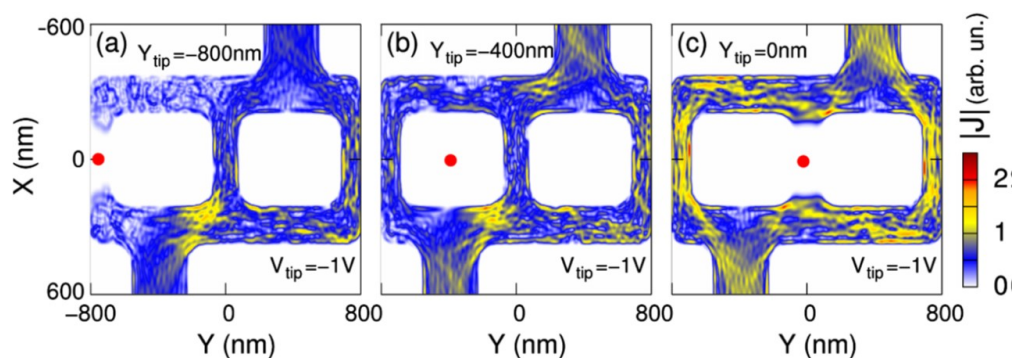


Figure 3.6: Quantum simulations of the current density J inside the network in presence of a scanning tip (red point). The tip potential is tuned to deplete entirely the 2DEG when the tip is above the lateral arm (a) or central arm (c). The unperturbed situation corresponds to (b). The colorscale is the same in the three panels, such that the current flows can be compared. Data reprinted from [18].

3.6 Localization at low charge density

Even though 2DEGs in semiconductor heterostructures show very-high carrier mobility, they still suffer from residual potential fluctuations induced by the random distribution of the remote ionized dopants. At low enough charge carrier density, this disorder potential drives a metal-to-insulator transition with charge localization at low temperature. Potential fluctuations also play a key role in the physics of the quantum Hall effect by creating a band of localized states between the Landau levels. To reach a better understanding of these phenomena, scanning probe microscopy can be used to map localization effects in real space.

In this work [21], we employed SGM to investigate the inhomogeneity of the potential landscape in the 2DEG patterned into narrow wires. This study has been performed on a device with the same geometry as for the investigation of the mesoscopic Braess paradox, thus with three narrow wires in parallel, but with a lower charge density in order to have a larger influence of the potential fluctuations (Fig. 3.7). In this sample, the SGM images revealed several sets of concentric circles typical of Coulomb blockade in quantum dots. The detailed analysis of the SGM conductance images as function of tip position and tip voltage points towards the formation of quantum dots along the narrow wires due to the potential fluctuations in the 2DEG. These fluctuations create several confining barriers in series along the narrow wires, and the effect of the SGM tip is to bring them at the Fermi level to reveal their existence in transport measurements. The SGM images therefore reveal the regions with large potential fluctuations. Numerical simulations have been carried out with a realistic potential disorder in order to support this interpretation. The key point in this experiment was the use of trans-conductance measurements with a periodic modulation of the tip voltage and a detection of the current modulations at this frequency. This technique was essential to enhance the effect of tip-induced charging in the Coulomb-blockade quantum dots.

As a result, this work provides a new experimental demonstration of the existence of significant potential fluctuations even in high-mobility systems. It is interesting to note here that the first demonstration of a non-uniform electron flow in high-mobility 2DEGs was also obtained by SGM using point contacts [39] as discussed in the next chapter. From a more general point of view, these SGM works have shown the importance to make the distinction between the hard scattering centers, which affect the electron mobility at the Fermi level, and the smooth potential fluctuations, which are hidden below the Fermi level, but influence significantly the propagation of the electron waves.

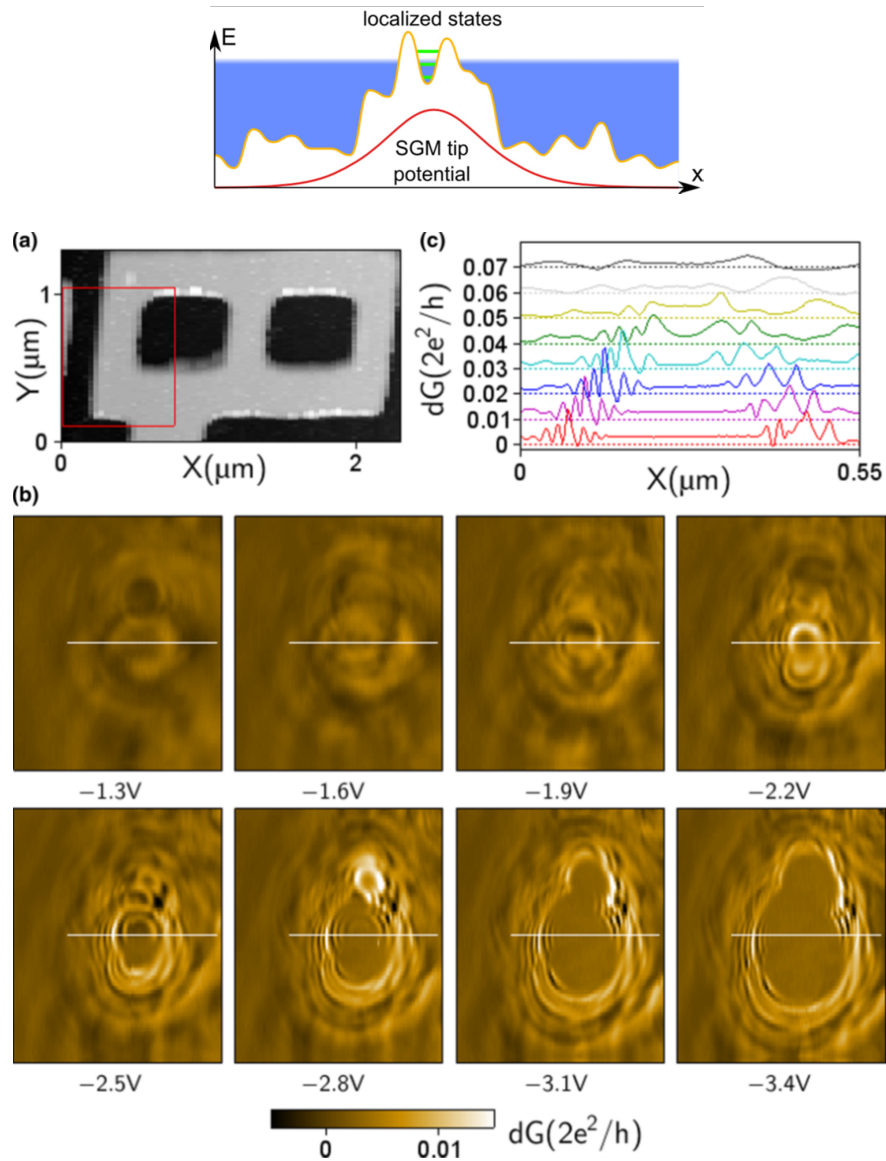


Figure 3.7: (top) Schematic of the potential fluctuations brought locally at the Fermi level by the tip-induced potential and creating quantum dots with Coulomb blockade in transport measurements. (a) AFM topography of the device. The red rectangle indicates the region of the SGM images shown below. (b) SGM images for increasing negative tip voltages. Several quantum dots are formed along the wire when the tip is moved along this wire. At large negative tip voltage, full depletion occurs in the wire, visible as regions without any features. (c) Conductance changes along the white lines in (b) showing the tip-controlled Coulomb blockade oscillations of the quantum dot located at the white line position. Data reprinted from [21].

Chapter 4

SGM investigations of GaAs quantum point contacts

This research has been performed in the context of the collaborative ANR project “ITEM-exp” involving the Néel Institute (coordinator), the CEA-INAC in Grenoble, the CNRS-LPN in Marcoussis, and the UCL-IMCN in Belgium. Most of the experiments were performed from 2011 to 2014 by a brilliant PhD student, Boris Brun. A new research project has emerged based on the same collaborative network and will be discussed in the last chapter.

The objective of the project was to investigate the role of electron interactions on the anomalous transport properties of quantum point contacts (QPC), used as basic building blocks in more complex quantum circuits. This simple device is a ballistic constriction in a two-dimensional electron gas, which forms a quasi-one-dimensional channel with quantization of the transverse electron wave vector (Fig. 4.1). In addition to its well-known quantized conductance curve versus split-gate voltage, two anomalous features have been studied for more than 15 years without being understood : the 0.7 anomaly below the first conductance plateau [139] and the zero-bias anomaly in the source-drain spectroscopy [140]. Several microscopic mechanisms involving electron interactions have been proposed to explain their origin, but none of them is satisfactory. The necessity to bring new kinds of information to clarify this complex problem has motivated the present project.

In contrast to most of the previous studies, we used a local potential perturbation to probe these anomalies in real space. This local perturbation was induced either by a thin metallic gate patterned on the surface, or by the more flexible technique of scanning gate microscopy (SGM) where a sharp metallic tip is used as a local and movable gate. This technique allowed us (i) to finely tune in-situ the potential profile of the constriction in order to check the properties of the electronic state, and (ii) to produce an interference pattern by back-scattering the electrons towards the QPC in order to check the transmission phase of the electronic state. These experiments required the joint effort of four research groups with complementary expertise : the three partners of the project (NEEL, INAC, LPN) plus a decisive collaboration with a group in Louvain-la-Neuve (Belgium).

The major result is the periodic modulation of the conductance anomalies when the SGM tip distance is varied, with the anomaly oscillating between one zero-bias peak and two finite-bias peaks. This phenomenon is interpreted in terms of a non-equilibrium Kondo effect and supports the scenario of a localized spin chain induced by electron interactions, a sort of one-dimensional Wigner crystal [23]. A second important result is the observation of an abrupt phase shift of the interference fringes when the QPC is tuned in the region of the 0.7 and zero-bias anomalies. This shift reveals the transmission phase of the electrons crossing the QPC and shows strong similarities with the case of quantum dots in the Kondo regime [24]. Finally, thermoelectric SGM experiments revealed new phase shifts at very low transmission where standard SGM becomes inefficient [25].

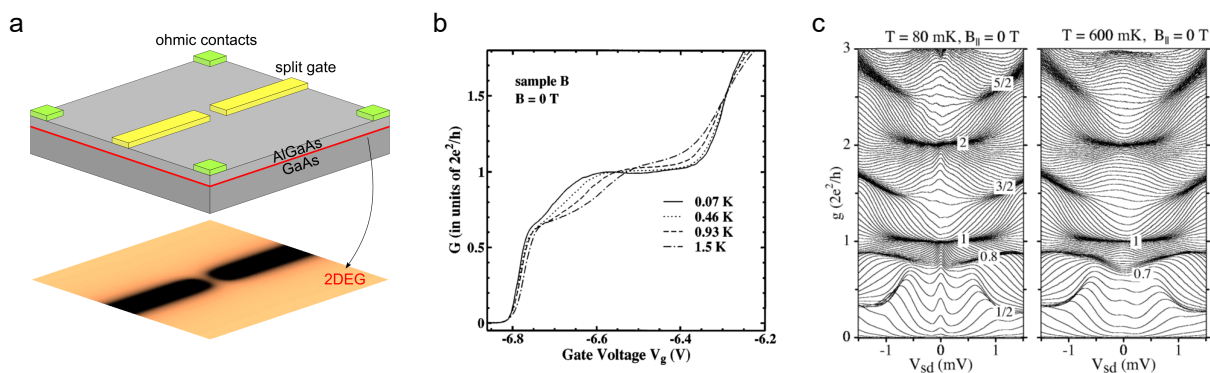


Figure 4.1: (a) Quantum point contact defined in a 2DEG by the voltage applied on a split-gate. (b) Linear conductance versus split-gate voltage, showing the 0.7 anomaly below the first plateau of quantized conductance. Reprinted from [139]. (c) Differential conductance versus source-drain bias for different split-gate voltages, showing the zero-bias anomaly below the first plateau. Reprinted from [140].

4.1 Interactions and conductance anomalies in QPCs

The mesoscopic regime of electron transport deals with nanometer-scale devices which are much larger than the fully-quantum atomic scale, but small enough to exhibit significant quantum phenomena at low temperature. In this regime, electronic transport is sensitive to defects, impurities, potential disorder, thermal phonons, magnetic field, electron-electron interactions, leading to a variety of interesting and complex physical problems. A mesoscopic device hosts a large number of conducting electrons, and dealing with the Coulomb interactions between all these charges is a very complex problem. Although this interaction is intrinsic, the complexity of its treatment often makes it the last property to be included in the theoretical description of the system. This repulsive interaction is however very important, or even dominant, when the electrons have a reduced velocity. This electron-electron repulsion acts as a sort of energy barrier for the electron transport. It results, for example, in the Mott localization for large systems at low electron density, or in the Coulomb blockade effect for small quantum dots. In quantum point contacts (QPC), the electron density is also very low when the conductance is lowered below the first quantized conductance plateau. There, electron-electron interactions play a significant role, and produce interesting phenomena such as the 0.7 anomaly in the conductance curve versus split-gate voltage. The objective of this project is precisely to investigate the role of interactions in QPCs in this low-density regime.

A QPC is a narrow constriction obtained by squeezing locally a high-mobility two-dimensional electron gas (2DEG) by electrostatic depletion using surface gates. This ballistic constriction forms a quasi-one-dimensional channel which is open on larger contacts, and shows a quantized conductance due to quantization of the transverse electron wave vector. By varying the potential in the QPC, zero, one, or more transverse modes can be involved in the total conductance, giving a series of conductance plateaus at integer values of $2e^2/h$ (the factor 2 coming from the spin degeneracy). In practice however, the conductance-versus-gate-voltage curves show significant variations depending on the exact geometry of the channel. Sometimes the plateaus are poorly defined or anomalies appear in the steps between the plateaus. The design of a good QPC is usually empirical and is obtained after several trials and successive improvements. A better understanding of their behavior is however fundamental, since QPCs are basic quantum devices which are parts of more complex quantum circuits. QPCs are, e.g., used to define quantum dots with controllable tunneling rates [141], punctual injectors and detectors in ballistic devices for collimation experiments [142], or beam-splitters for quantum Hall edge currents [143, 144] (although here the quantization is of different origin).

Among the open questions on QPCs, the origin of the so-called 0.7 anomaly is still a very debated subject. This anomaly below the first conductance plateau [139] has been investigated experimentally as a function of constriction length, temperature, in-plane magnetic field, gate voltage, in devices controlled by surface gates, lateral gates, top gates, in electron or hole systems, by conductance, finite bias, shot-noise, and other kind of experiments

[140, 145, 146, 147, 148, 149, 150, 151]. Nevertheless, after being studied for more than 15 years, its origin still remains puzzling. “It’s the single most important open problem in the field of quantum ballistic transport”, claimed Beenakker [152]. From a theoretical point of view, this anomaly cannot be explained within the non-interacting electron formalism, and several theories or phenomenological models have been proposed to address this question by including the electron-electron interactions [153, 154, 155, 156, 157, 158, 159]. These theories cannot reproduce completely the experimental observations, and they disagree on the origin of the phenomenon [152, 160]. Many correlated states have been proposed as possible explanations including a spin polarized state, a Kondo-like state, a charge density wave, a Wigner crystal (Fig. 4.2), but a unique satisfactory explanation has not yet been found. Clearly, the effects of electron interactions in QPCs are far from being understood and thus required further investigations, justifying the present project.

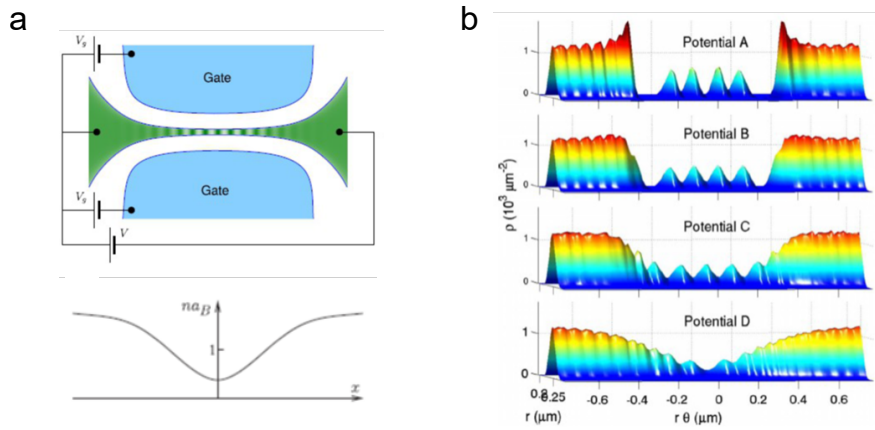


Figure 4.2: One-dimensional Wigner crystallization in a ballistic channel at low electron density. (a) The continuous electron density (in green) breaks up into a correlated chain of individual charges when the critical parameter $n a_B$ goes below unity, n being the electron density and a_B the effective Bohr radius in the 2DEG. Reprinted from [153]. (b) Quantum Monte Carlo simulation of the electron density for different sharpness of the potential step between the lead and the channel, from sharp in A to smooth in D. The Friedel oscillations in the leads (liquid state) change to a correlated chain in the channel (crystal state). Reprinted from [161].

4.2 Originality of the experimental approach

In most of the experimental studies, the influence of electron-electron interactions on the transport properties of QPCs was investigated by electric transport measurements on an isolated QPC. Here, our original idea was to use an additional control parameter, in the form of a local electron scatterer (a thin surface gate or a sharp scanning gate) located outside the interacting region of the QPC, but still coherently coupled to it. In the original proposal, this scatterer was aimed at modifying the electron density in the QPC by the so-called Friedel oscillations, without changing the potential inside the QPC. This idea was studied in details during the theoretical ANR project “ITEM-th” (interaction and transport at mesoscopic scale : theory) started in 2008 and coordinated by Jean-Louis Pichard from the CEA/SPEC in collaboration with Dietmar Weinmann and Rodolfo Jalabert from IPCMS. Our project was originally inspired by these theoretical ideas as a possible route to measure the strength of the interactions in the QPCs, with the objective to elucidate the origin of the 0.7 anomaly. The ANR project “ITEM-exp” (interaction and transport at mesoscopic scale : experiments), which started in November 2010, was in fact the experimental counterpart of the ANR project “ITEM-th”.

In the theoretical proposal, a local scattering center located away from a QPC was used to reflect the electrons coming out of the QPC back into itself and influence the density in the QPC through a non-local action. The back-scattering of the electrons from the tip position into the constriction involves electrons at all energies, and the resulting Friedel oscillations of the electron density should change the amount of interactions in the QPC (Fig. 4.3). This approach represents an original way of testing the properties of the correlated state formed at low density in the QPC, without changing capacitively the size of the constriction as usually done with the QPC split-gate itself. In addition, the multiple reflections between the QPC and the scattering center produce Fabry-Perot interference in the transport at the Fermi level, and it was predicted that the interference pattern should be significantly influenced by the electron interactions in the QPC at low electron density [95, 162].

A specificity of the project was to use the unique possibility to move the scattering site by moving the sharp polarized tip of an SGM microscope. Besides the control of the scatterer position with nanometer accuracy, the advantage of this type experiment is the absence of contact between the gate and the semiconductor material that preserves the high electron mobility in the 2DEG and allows a precise comparison of the QPC conductance with and without the presence of the scattering center. In addition to the SGM experiments, the project also included similar scattering experiments based on devices where a narrow surface gate was patterned at a few hundreds of nanometers from the QPC and playing the same role as the scanning gate. In this type of device, the effective position of the scattering center can be changed continuously through the applied voltage that controls the depletion area below the narrow scattering gate. The comparison of these two types of experiments provided very valuable information for the interpretation of the results.

Interestingly, the SGM technique was originally developed precisely to investigate QPCs

[37], before being applied to various other semiconductor nanostructures. The previous SGM studies of QPCs included the transverse quantization in the constriction [38, 53], the branched electron flow with interference patterns in the 2DEG [39, 40, 48, 49, 69], a tuning of the 0.7 anomaly versus tip position [57, 80], and possible effects of disorder in etched devices [163, 84]. In a study done at Stanford in 2009 on the interference between the QPC and the tip [49], the authors say : “This interferometer may prove useful for studying electron interactions and complex flow patterns in the 0.7 structure regime of a QPC in which transport measurements indicate correlated electron structure”, citing the theoretical work done in the French ANR project “ITEM-th” [95, 162]. This original idea, which was at the basis of our experimental ANR project, was therefore also in the mind of the leading groups at the international level when starting our project in 2010.

This project involved four partners, all experts in the field of low temperature mesoscopic physics, but with complementary expertise, the partner NEEL on scanning gate microscopy, the partner INAC on very low temperature transport measurements, the partner LPN on the growth and the patterning of high-mobility two-dimensional electron systems, and the partner IMCN in Belgium on scanning gate microscopy at very low temperature.

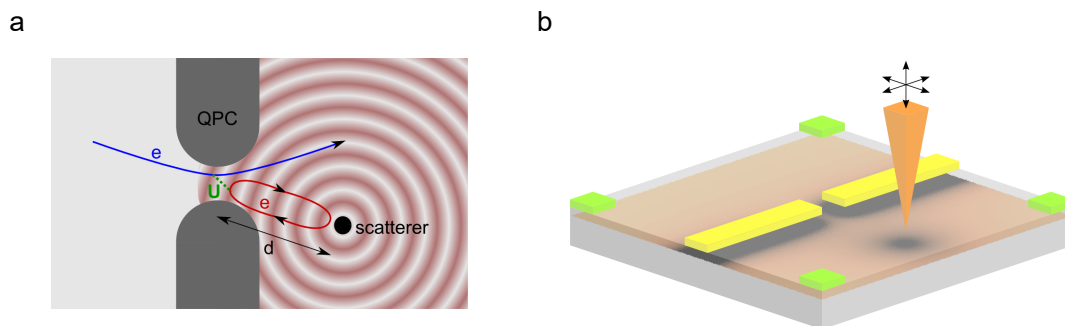


Figure 4.3: (a) Original idea of using a scattering center to modulate the electron density in the QPC by Friedel oscillations (red). If conduction electrons (blue) interact with other electrons in the QPC, they should be sensitive to these density oscillations. (b) Implementation of this idea using the tip of a scanning probe microscope to apply a local potential change.

4.3 Overview of the experiments

The first task of the project was the fabrication of quantum point contacts with good properties. After a few trials, very good devices have been fabricated by Ulf Gennser and Dominique Maily. The GaAs/AlGaAs heterostructure contains a 2DEG located 105 nm below the surface, with a low-temperature mobility equal to 1.0×10^6 cm²/V/s and a density 2.5×10^{11} /cm². Several geometries of quantum point contacts have been fabricated on this heterostructure, showing a well quantized conductance, no charge noise, and no gate leakage. The optimal dimensions of the constriction were found to be about 300 nm in width and 300 nm in length. In these devices, the interaction effects are clearly visible, showing both the 0.7 anomaly and the zero-bias anomaly. About 10 devices have been the object of deeper investigations and gave interesting results.

Before the SGM experiments, a few transport experiments were performed on devices with a narrow additional gate patterned on the surface, in order to induce a back-scattering of the transmitted electrons and generate interference. These experiments were conducted with Marc Sanquer at INAC, at very low temperature, and revealed interesting interference patterns. These patterns were studied as a function of various parameters to understand their origin and search for their influence on the conductance anomalies (see section 4.4). These transport experiments were preliminary to the SGM experiments conducted afterward using devices with only the QPC split-gate.

The 4 K SGM microscope at NEEL was first redesigned to reach better stability during the long SGM measurements. A few SGM images were recorded with this microscope on QPC devices. The images showed an interesting pattern of lines and a few interference fringes. The lines were later interpreted as the result of a tip-induced back-scattering in presence of a hard-scatterer in the reservoir, thanks to a collaboration with the theory group of Bartłomiej Szafran in Krakow (Poland) during a short stay of his student Krzysztof Kolasinski in Grenoble [26].

Since the temperature of this 4 K microscope was too high to have good conductance quantization and to observe tip-induced interference fringes, the SGM experiments were then performed in Louvain-la-Neuve (Belgium) with Benoit Hackens and Vincent Bayot. Their SGM microscope is working in a dilution fridge down to a temperature of 20 mK and in a perpendicular magnetic field up to 17 T. Two series of measurements have been conducted, one in February and March 2013, and one in February and April 2014. Four devices have been studied in details, which gave very good and unexpected results, which will be detailed in the sections 4.5, 4.6, 4.7 below.

4.4 QPC with patterned interferometers

In devices with an additional narrow gate at about 800 nm from the QPC and aligned on the transport axis (Fig. 4.4a), we observed a periodic modulation of the conductance as a function of the voltage applied on the additional gate. This modulation corresponds to the electronic interference described in the proposal, due to multiple reflections between the depleted regions below the additional gate and below the split-gate. The behavior of this interference has been studied as a function of the QPC opening, temperature, source-drain voltage, and perpendicular magnetic field [22]. The quantum transport simulation software KWANT developed at INAC (<http://kwant-project.org>) was used to simulate this back-scattering experiment and to interpret the data. We analyzed the crucial role of disorder in the origin of the interference and reached the conclusion that the interference involves, as expected, the electron trajectories between the QPC and the additional gate. This well-defined back-scattering behavior constitutes a good result when compared to previous studies in the literature. It is also crucial for the realization of the project since it demonstrates that the interference involves the QPC itself as one of the cavity mirror and could thus provide information on the interaction effects in the QPC.

The most interesting result was the observation of an abrupt shift of the interference fringes when the conductance is lowered below the first plateau and enters the regime of the 0.7 anomaly (Fig. 4.4c). We assume that this shift arises from a particular transmission phase of the electrons when they are transmitted through the QPC in the correlated state that gives rise to the 0.7 anomaly. This result has been confirmed in the two devices which were studied in details at INAC, and in a third one studied later in Louvain-la-Neuve. A similar phase shift was also observed in the evolution of the interference fringes versus source-drain bias (Fig. 4.4d), with probably the same origin. A correlation with the zero-bias anomaly could however not be demonstrated during this experiment, but this was done later in the SGM experiments discussed below.

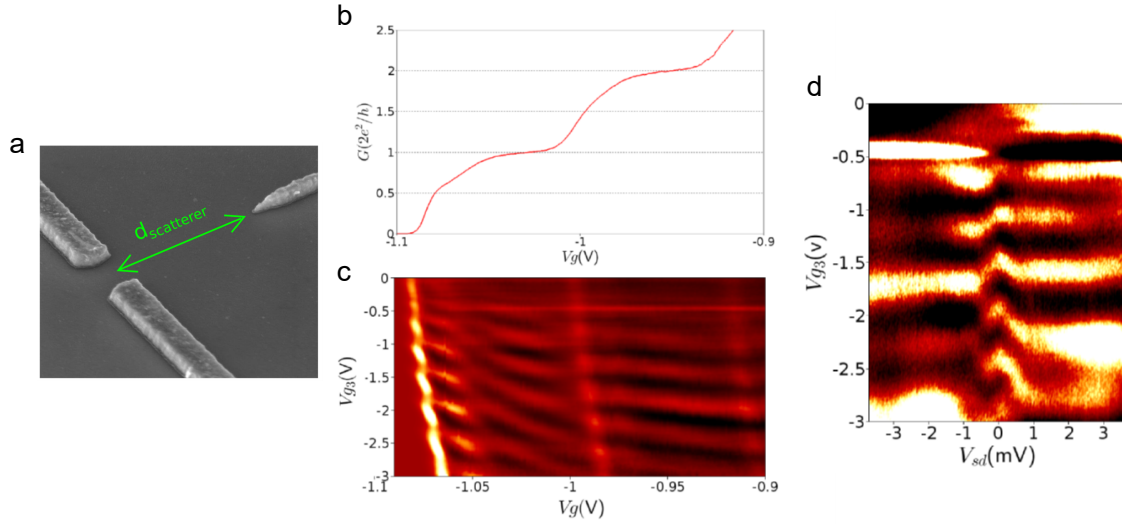


Figure 4.4: (a) Interferometer device made of a split-gate and a scattering-gate. (b) Conductance curve versus split-gate voltage. (c) Interference fringes versus scattering-gate voltage (V_{g3}) and split-gate voltage (V_g), showing a phase shift in the region of the 0.7 anomaly. (d) Interference fringes versus scattering-gate voltage (V_{g3}) and source-drain bias (V_{sd}), showing a phase shift at low bias. Data reprinted from [22].

4.5 SGM tuning of a 1D Wigner crystal

The major results were obtained in the simple QPC geometry using SGM at very low temperature. When the QPC is tuned on the first conductance plateau, the SGM images show the well-known branched electron flow decorated by interference fringes as reported in the early SGM experiments on QPCs. These interference fringes have the same origin as those discussed in the previous section and will be studied in the next section. Here we focus in a regime where the QPC conductance is tuned below the first plateau. By moving the potential perturbation of the SGM tip around the QPC, we observed a periodic modulation of the 0.7 anomaly, correlated with a periodic splitting of the zero-bias anomaly (Fig. 4.5c,d).

After having excluded various other effects, we could conclude that this phenomenon corresponds to a change in the number of localized charges in the constriction in presence of strong electron-electron interactions. The explanation is the following. When the number of localized charges is odd, a single peak is observed at zero bias due to the usual Kondo effect in presence of an unpaired electron spin. When this number is even, the peak is shifted at finite bias due to a non-equilibrium Kondo effect involving the excited triplet state [164] (Fig. 4.5e,f).

This discrete change in the number of localized charges is similar to the Coulomb blockade effect in a quantum dot, but it appears here in absence of confining barriers, since the QPC is an open system. This spontaneous charge localization corresponds to the formation of a one-dimensional Wigner crystal, which is one of the theoretical scenarii that could occur in QPCs in presence of interactions [153].

These results have been published in Nature Communications [23] and have been presented in several international conferences (EP2DS 2013, ICPS 2014) and workshops (Vietnam 2013, Poland 2013, Italy 2014), including three invited talks. At the same period, another group obtained a similar result using a device with six surface gates to define a QPC with a tunable length [165]. The fact that the same result has been obtained with two different techniques gave stronger confidence to this finding.

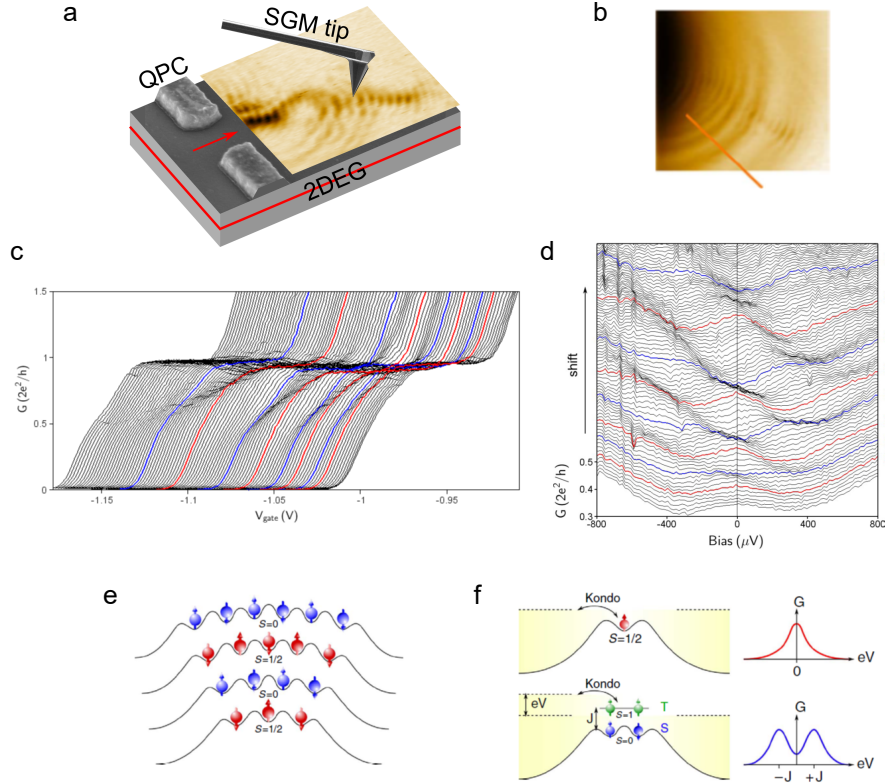


Figure 4.5: (a) Schematics of the SGM experiment on a QPC. The SGM image has been measured with the QPC tuned on the conductance plateau. (b) SGM images recorded with the QPC below the first plateau. Large concentric rings are visible and correspond to a periodic modulation of the 0.7 and zero-bias anomalies, as shown respectively in (c) and (d) when the SGM tip is scanned along the orange line. (e) Discrete change of spontaneously localized charges when the SGM tip approaches the QPC. The number of charges is alternatively odd and even. (f) An odd number of localized charges gives rise to a Kondo effect on a single unpaired electron, whereas an even number gives rise to an out-of-equilibrium Kondo effect on the triplet state. Data reprinted from [23].

4.6 Kondo phase shift probed by SGM interferometry

In this section, we report the analysis of the interference fringes induced by scanning the SGM tip at a finite distance from the QPC as suggested in the proposal [24]. Although the interference pattern was rather complex due the residual disorder, we could investigate well-defined series of fringes within the branches of the electron flow visible on the SGM images (Fig. 4.6b). The important result was the observation of an abrupt phase shift of the fringes in the region of parameters where the zero-bias anomaly (ZBA) is present (Fig. 4.6c,d). The observation of an intimate QPC property in the interference pattern demonstrates that the interference occurs directly between the tip and the QPC, and not between scattering sites of the disordered potential landscape as often reported in the literature.

The observed phase shift in presence of the ZBA is similar to the one observed in quantum dots placed in Aharonov-Bohm interferometers and tuned in the Kondo regime [166, 167]. In that case, a universal $\pi/2$ phase shift is obtained because the many-body screening of a single spin localized in the dot restores a perfect transmission through the dot. In the case of the QPC, the observed phase shift in the interference pattern could be another signature of the Kondo effect, which is one of the possible origins for the ZBA.

This experimental result supports the explanation of the conductance anomalies in terms of spontaneously localized charges in the constriction, where the localized spins are screened by the conduction electrons of the leads below the Kondo temperature. This shift shows the same properties as the one observed in transport experiments on QPC devices with an additional surface gate (see Sec. 4.4 above). Both effects therefore have probably the same origin, which is a Kondo phase shift.

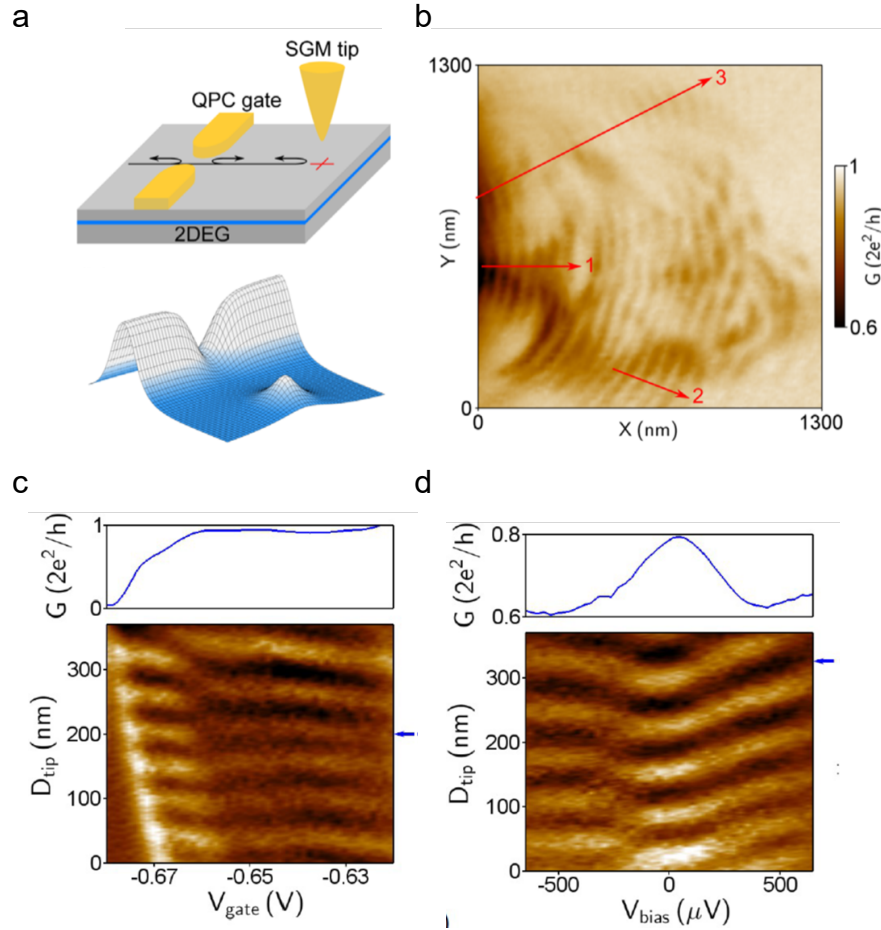


Figure 4.6: (a) Principle of scanning gate interferometry to investigate the QPC reflection phase. (b) SGM image in the 2DEG region in front of the QPC. Lines indicate branches of the electron flow where the interference fringes are well-defined. (c) Phase shift of the fringes in the gate-voltage range of the 0.7 anomaly shown in the top panel. (d) Phase shift of the fringes in the bias-voltage range of the zero-bias anomaly shown in the top panel. Data reprinted from [24].

4.7 Thermoelectric scanning gate interferometry

Finally, an interesting result has been obtained by measuring the thermovoltage of the QPC instead of the conductance. It was the first SGM experiment measuring the thermovoltage of a quantum device, and we named this technique Thermoelectric Scanning Gate Microscopy (TSGM) [25].

A thermovoltage experiment consists in applying a temperature difference between the source and drain reservoirs of the QPC, and measuring the resulting voltage drop. In absence of electron interaction, the thermopower $S = (\frac{\partial V}{\partial T})_{I=0}$ is related to the conductance G by the Mott's relation :

$$S^{\text{Mott}}(\mu, T) = -\frac{\pi^2 k_B^2 T}{3e} \frac{1}{G(\mu, T)} \frac{\partial G(\mu, T)}{\partial \mu}$$

In presence of electron interaction however, the thermopower deviates from this relation, such as in quantum dots with Coulomb blockade. In a QPC below the first plateau, the strong interactions responsible for the conductance anomalies also produce deviations from the Mott's relation [168].

We performed such thermovoltage measurement by heating one of the two reservoirs while keeping the other one at the fridge temperature (Fig. 4.7a). This heating was achieved by injecting a large current between two ohmic contacts of the same reservoir, and the resulting temperature was calibrated using the Mott's relation in the gate-voltage range where the QPC is open with several modes. Then, in the region of the anomalous thermopower below the first conductance plateau, we performed TSGM experiments with the tip scanned in front of the QPC to generate interference fringes. The TSGM images of the thermovoltage revealed essentially the same pattern of interference fringes as the SGM images of the conductance, in agreement with the Mott's relation (Fig. 4.7b,c). These TSGM images of interference fringes constitute the first images of a coherent heat flow in a mesoscopic device.

Surprisingly, a phase shift of the interference fringes was observed at low transmission in the thermovoltage signal, whereas this shift was not visible in the conductance signal measured in the same conditions. The phase shifts in the conductance fringes (discussed in the previous section 4.6) were usually observed at intermediate transmission around 0.7 and never at very low transmission. A reason could be that the fringes in conductance have a very low contrast at low transmission, whereas the fringes in thermovoltage are reinforced due to its $1/G$ divergence at low transmission, such that TSGM is more sensitive than SGM in this regime. Regarding the origin of the phase shift observed at very low transmission, it has been tentatively attributed to the presence of a localized state on the shoulder of the QPC potential barrier whose maximum is significantly above the Fermi level.

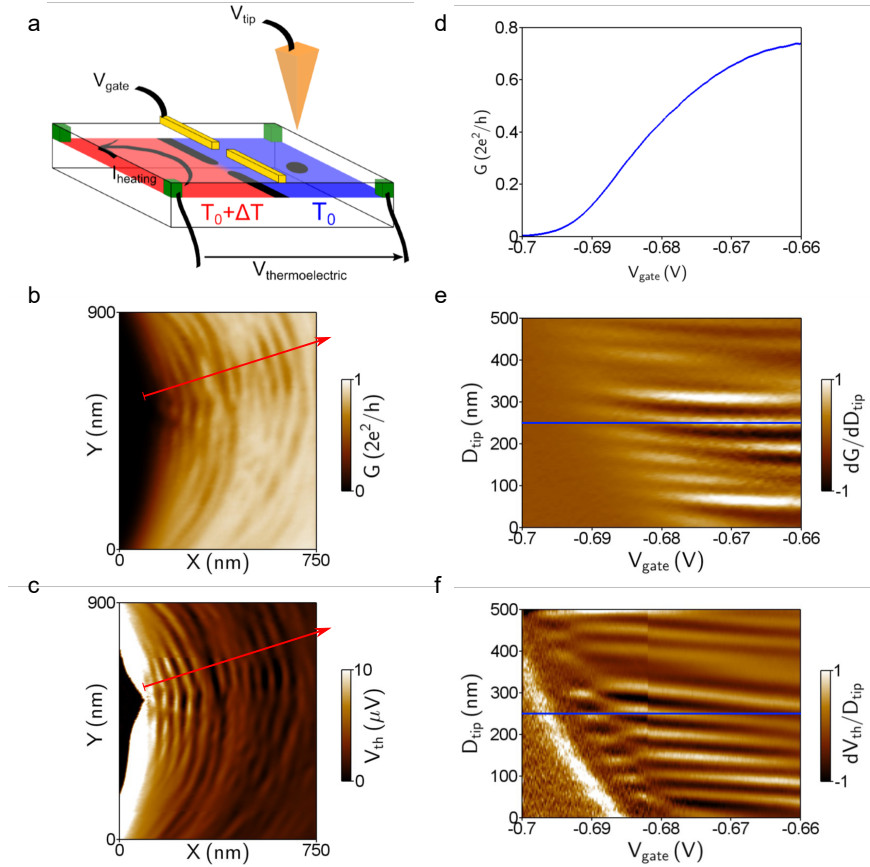


Figure 4.7: (a) Principle of a TSGM experiment (thermoelectric scanning gate microscopy) in which the polarized tip is scanned above the surface while recording the thermoelectric voltage. The temperature difference is obtained by heating one reservoir with a large current while keeping the other at 25 mK. (b) SGM image of the conductance recorded with a small voltage of $10 \mu\text{V}$. (c) TSGM image of the thermovoltage recorded with a heating current of 150 nA corresponding to a reservoir temperature of 450 mK. (e,f) Interference fringes along the red lines in (b,c) versus split-gate voltage in the region below the first conductance plateau. The conductance trace, when the tip is at the position of the blue lines, is shown in (d). Data reprinted from [25].

4.8 Perspectives

After this series of experiments, a lot of questions still remain on the nature of the correlated state induced by the interactions, like the static or dynamic nature of the localized charges, or the spin structure of the chain. Several kinds of experiments could be done to investigate these properties, like magnetic focusing experiments, high-frequency experiments, and charge detection experiments including electrostatic force microscopy (EFM). In particular, the 0.7 anomaly, which survives up to very high temperatures compared to the other energy scales, is far from being understood. Explaining this puzzling effect, more than 30 years after its first observation, remains a challenge for the future. A research proposal was submitted to the ANR to continue this work but it was unfortunately not funded.

Chapter 5

Projects on GaAs devices

In this chapter, I describe my research projects related to SGM investigations of quantum devices based on semiconductors 2DEGs. The first one is a continuation of the past ANR project “ITEM-exp” described in the previous chapter. I submitted a pre-proposal to the ANR calls 2015 and 2016, but the project was not selected. Since I would like to develop some of the proposed experiments anyway, I will describe this project in the first section below. The second project has emerged from our previous work on QPCs where the zero-bias anomaly could be interpreted in terms of Kondo effect, and therefore deals with the Kondo effect in semiconductor quantum dots (QD). More precisely, the objective is to measure the spatial extension of the Kondo cloud of screening particles and to investigate its entanglement properties. I submitted a detailed proposal to the ANR calls 2017 and 2018, and it was finally selected the second year. This “KONEX” project started in June 2019 and will be presented in the second section below.

Other projects have been considered and submitted to the ANR but were not funded and will not be described here. I just mention a project concerning the on-the-fly manipulation of individual spins in InAs 2DEGs using the spin-orbit Rashba effect. This project was submitted to the QuantERA European call in Spring 2017, passed the first round of selection, but was finally not selected for funding. This project called “Ballistic Spin-Orbitronics for quantum computation” involved the partners IMCN in Louvain-la-Neuve, IEMN in Lille, AGH in Krakow, and NEEL in Grenoble.

5.1 Spontaneous charge localization in quantum point contacts

Quantum point contacts (QPCs) are basic quantum systems where very fundamental questions can be addressed. A QPC is a ballistic quasi-one-dimensional channel obtained from a two-dimensional electron gas (2DEG) by depletion with a pair of metallic gates [169]. This channel represents a nanoscale region of low electron density, which is freely connected to large reservoirs with higher density. When the channel is made sufficiently narrow such as to allow the transmission of a single transverse mode, the conductance shows anomalous features called the 0.7 anomaly [139] and the zero-bias anomaly [140]. In this regime, the QPC is a one-dimensional system of strongly interacting electrons within a non-uniform potential and a strong coupling to the reservoirs. This system is so complex that theory is not yet able to predict its properties and explain the origin of the observed conductance anomalies [160]. Experts in the field do not hesitate to qualify this problem as one of the most stubborn problem in mesoscopic physics. Despite intensive experimental and theoretical efforts, the QPC behavior at low density is still an open problem in condensed matter physics.

During our ITEM-exp ANR project presented in chapter 4, we could demonstrate experimentally that several electrons spontaneously localize in the constriction due to the strong repulsive interaction between them. This outstanding result could be obtained by combining high-resolution transport measurements at very low temperature with the unique capability of scanning gate microscopy (SGM) to tune in-situ the potential of the constriction. This result has been published in Nature Communications [23] and received considerable attention during conferences. The increasing number of spontaneously localized charges was deduced through the occurrence of repetitive splitting of the zero-bias anomaly, corresponding alternatively to equilibrium and non-equilibrium Kondo resonances. This phenomenon is a beautiful signature of the presence of several localized charges and was not anticipated before in the numerous theoretical works on the subject : neither in those explaining the zero-bias anomaly by the Kondo screening of a single localized charge [170], nor in those predicting the spontaneous localization of several charges [161]. At about the same time, a similar result was obtained independently by another group using a different technique [165], therefore giving confidence to these findings.

This demonstration of the presence of several localized charges is an important step towards the understanding of this complex many-body problem, but the enigma around the 0.7 anomaly is not yet elucidated, and an abundance of questions remains :

- What is the spatial structure and dynamics of the localized charges ? As opposed to quantum dots, there is probably not a definite and static set of charges in such an open system.
- What is the spin structure in this chain of charges ? Theories either predict an anti-ferromagnetic coupling in a 1D Wigner crystal [161], or a spontaneous spin polarization like in a ferromagnet [171].

- What are the transport mechanisms through this correlated state? The conduction in this 1D wire could present the spin-charge separation of Luttinger liquids [153].
- Why is the zero-bias peak visible down to very low conductance ? The localized state and the Kondo resonances should in principle disappear when the channel is empty.
- Why is the 0.7 anomaly so robust at higher temperatures ? The anomaly is still visible above 4 K when the other quantum phenomena have disappeared.
- Is the spontaneous localization limited to purely 1D channels or can it occur in the second mode ? Weaker anomalies are indeed also observed below the second conductance plateau.
- What is the role of disorder and channel geometry ? Nominally identical devices often show different behaviors with respect to their conductance anomalies.
- Are theoretical investigations going in the right direction, or is there a crucial ingredient missing ? An alternative and controversial theory has been proposed in Ref. [172].

Because of their fundamental importance for the understanding of strongly interacting systems, these questions are greatly debated and stimulate experimental and theoretical efforts from highly reputed research groups all over the world. Based on the experience gained during the successful ITEM-exp project, we would like to continue our investigations of these phenomena and address some of the above questions with our original approach, combining transport experiments and scanning probe techniques.

Several discussions with the scientific community during conferences have underlined the importance to get additional information on the localized state revealed by our SGM experiment, in order to understand the nature of this correlated state. In particular, a spatial mapping of the charge localization and a determination of its spin structure would probably solve this complex problem. The present proposal aims at tackling these questions by performing new experiments which are all challenging, but really necessary to make decisive progress.

Detection of the localized charges using a coupled electrometer

The direct detection of Coulomb-blockaded charges in quantum dots (QD) is traditionally done using very sensitive built-in electrometers, which are capacitively coupled to the QD, in particular with QPCs tuned in the transition between two plateaus where the conductance varies abruptly with the external electrostatic potential [173]. Here the detection of spontaneously localized charges in a QPC showing conductance anomalies could also be probed with such an electrometer, by building a second QPC very close to the first one. Since the spontaneous localization in QPCs is weaker than the Coulomb blockade effect, the signal will be smaller than for QDs where it is easily measured. We will therefore start with a

QD, then progressively weaken the confinement, and finally suppress one of the two barriers to reach the case of a QPC with its conductance anomalies. This task is challenging, but is based on an established technique, which should be optimized to detect the localization effect in QPCs. Alternatively, this localized charge detection can be performed by dispersive reflectometry, a novel technique which has been successfully applied on QDs [174].

Detection of the localized charges using electrostatic force microscopy

Scanning probe techniques, in particular electrostatic force microscopy (EFM), could be used to get spatial information on the charge localization. Force detection with single-charge resolution has been demonstrated in the past for QDs located at the surface, e.g. self-assembled InAs dots [114], but never for QDs made in 2DEGs buried several tens of nanometers below the surface. The detection limit of a force sensor is however well below a single electron charge at this distance if the mechanical sensor is at liquid helium temperature in order to strongly reduce its thermal noise [175]. We will make use of a quartz tuning fork (TF) because of its high stiffness, that prevents jump-to-contacts, and because of its all-electrical read-out, that prevents optical excitation of carriers as compared to cantilever-based force sensors used in [114]. The lower force sensitivity of the stiff TF is compensated by an extremely high quality factor at low temperature in vacuum. TFs are indeed commonly used to measure very small atomic forces in non-contact mode and produce images with atomic resolution even at room temperature [176]. Here, a cryogenic current amplifier will be integrated in-situ with the TF to reduce its thermal noise to the lowest possible value. We will first start the charge detection experiments on QDs where charges are strongly localized, and then progressively shift to QPCs where the charge localization has to be investigated.

Detection of the electron crystal by microwave experiments

An original approach to test for the presence of the electronic Wigner crystal in the QPC is to measure its response to a high-frequency excitation (microwaves in the GHz range). An electron crystal in a bulk 2DEG is indeed expected to show a specific dispersion relation, similar to that of surface acoustic waves in usual crystals. This effect has been observed in low-density 2DEGs under a high perpendicular magnetic field [177] and interpreted as an evidence for the formation of a 2D Wigner crystal [178]. This 2D case requires the system to be placed in the extreme quantum limit, as opposed to 1D Wigner crystals, which should be observable at zero magnetic field, in standard conditions of density and temperature. Due to pinning [179] and finite size effects in the present case of a constriction, the absorption spectrum should show a resonant structure at a particular frequency. The spectrum dependence with the QPC geometrical parameters (width, length, shape, pinning defects) would be the signature of the sought-after electron crystal.

Determination of the spin state by magnetic focusing experiments

The spontaneously localized state in the QPC should have a particular spin structure due to strong exchange interactions between the electrons. If the electron chain is like a 1D Wigner crystal, it should have an anti-ferromagnetic ordering [161]. However, the conductance anomalies have also been interpreted as the formation of a spontaneously spin polarized state with ferromagnetic ordering [139, 171]. This scenario is incompatible with that of a Wigner crystal, and a more direct measurement of the spin polarization is therefore necessary to clarify the situation. For this purpose, we will measure the degree of spin polarized current emitted by a QPC in the regime of the 0.7 anomaly using a magnetic focusing geometry. This type of experiment has been done in the regime of the zero-bias anomaly at very low temperature [180], but in this case, the Kondo effect screens completely the localized spins and no conclusion can be drawn. A magnetic focusing experiment consists in bending the electron trajectory outside a QPC with a perpendicular magnetic field and collecting the electron beam with a second QPC. A spin polarized state in the QPCs should result in a specific signal which differs from the non-polarized case. This type of experiment is well known for a Zeeman polarization in strong parallel magnetic field [181] and will be applied here to investigate a possible spontaneous spin polarization in the regime of the 0.7 anomaly at zero field and moderate temperature. In case of a Wigner crystal, a zero spin polarization is expected, and the anti-ferromagnetic ordering will be analyzed as a function of the parallel magnetic field.

Manipulation of the spin state by scanning gate microscopy

We have already demonstrated [23] that the total spin of the localized state in the QPC can be periodically changed between 0 and $1/2$ when moving the polarized SGM tip around the QPC. This change was revealed by a splitting of the Kondo peak at very low temperature, but the Kondo mechanism giving a split peak at finite bias was not really understood. To investigate these different spin states in more details, we need to apply a large parallel magnetic field and tune the Zeeman energy while carrying out the SGM microscopy. Such an experimental configuration with a magnetic field parallel to the scanning plane has never been reported so far in the SGM literature and will require some instrumental development. With this unique instrument, we could also perform combined magnetic focusing and SGM experiments [41] in order to probe the spin polarization while tuning the spin state in the QPC. It also opens the possibility to test the presence of the localized charges by electrostatic force microscopy for various degree of spin polarization under parallel magnetic field. There is therefore a strong interest in developing a scanning probe microscope in this unusual parallel magnetic field configuration.

Impact of the project

Despite their apparent simplicity, QPCs represent fascinating objects for fundamental research on electron interactions in nanoscale systems. Their conductance anomalies, first reported more than 20 years ago, still defy our understanding. The objective of the project is to understand the microscopic mechanisms at the origin of these phenomena by performing original and decisive experiments. The impact of the expected results is set at two different levels. First, many quantum devices containing QPCs as basic building blocks, such as quantum dots and quantum Hall interferometers, would benefit directly from a better understanding of the QPC properties. Second, pushing further our investigations of these phenomena will provide us with a better understanding of condensed matter physics in general, and should therefore not be seen as a focus on a very specific problem. The QPC is an inhomogeneous system of strongly interacting electrons, restricted to a small region of space, and freely connected to large non-interacting reservoirs. From a theoretical point of view, this problem is very hard to tackle, because usual approximations are not valid, and there is currently no theoretical tool that can handle the exact equations. Solving this problem by a joint experimental and theoretical effort would be an important breakthrough, and would significantly enhance our knowledge on condensed matter physics.

Beyond the investigation of a complex physical phenomenon, our project also includes an important instrumental part of broad interest, with the development of the new experimental probes. In particular, achieving electrostatic force microscopy with single charge sensitivity on a 2DEG system would be of high interest for the investigation of other quantum systems with strongly correlated electron states, such as 2D Wigner crystals and exotic phases in the fractional quantum Hall regime. Even if the scientific project presented here and submitted to the ANR could not be funded, the instrumental development will be performed in the future to open new experimental perspectives for combined SGM-EFM experiments. An interesting project would be to measure in real space the hopping transport at the metal-to-insulator transition in semiconductor field-effect transistors.

5.2 Kondo-cloud extension around quantum dots

Known for a long time in metals with magnetic impurities, the Kondo effect has shown a revival since the late 1990's in the context of semiconductor quantum dots (QD) [182]. This many-body effect results from the dynamical screening of an unpaired electron spin in the QD by the conduction electrons of the reservoirs tunnel-coupled to the QD (Fig. 5.1). This mechanism produces a coherent state in which the localized and the itinerant electrons are entangled. Remarkably, the transmission through this coherent Kondo state is perfect at the Fermi energy, despite the fact that the QD is in the Coulomb blockade regime [183, 184]. The renown of the Kondo effect also comes from the existence of an exact solution at zero temperature and a single characteristic scale T_K for all the physical quantities. However, the complexity of the effect appears in the description of the crossover from the full-screening regime to the perturbative regime above the Kondo temperature, which requires the more sophisticated renormalization group theory [185]. Analogously to charge screening, the conduction electrons involved in this process form a screening cloud around the localized spin with a characteristic length scale ξ_K [186]. Despite its fundamental character and the numerous theoretical works on the topic, this so-called ‘‘Kondo cloud’’ has for a long time eluded experimental observation [187], and its very existence was an open question until very recently [188].

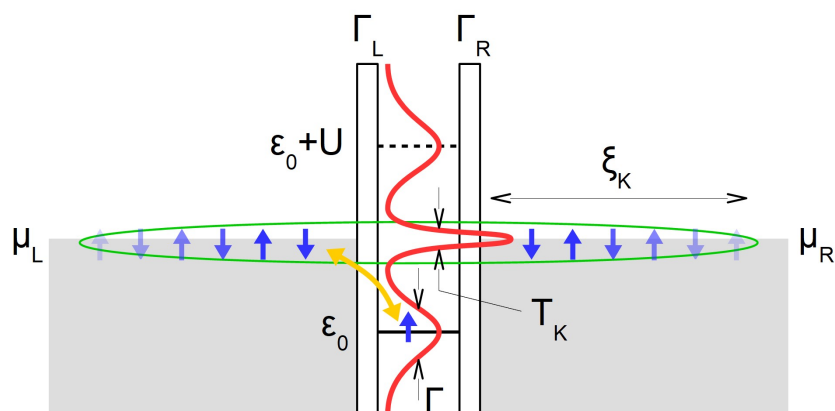


Figure 5.1: The Kondo effect is the dynamical screening (yellow arrow) of an unpaired electron spin in the QD (at energy level $\epsilon_0 < 0$) by the conduction electrons of the reservoirs (tunneling rates Γ_L and Γ_R). This coherent process creates a peak in the density of state (red curve) at the Fermi level of the reservoirs in an energy window $k_B T_K$. The Kondo cloud (green line) extends over a characteristic length $\xi_K \propto 1/T_K$.

Objectives

The objective of the project is to tackle this fundamental question with an original approach combining transport experiments and scanning probe microscopy, complemented by a strong theoretical support to analyze these complex experiments. Thanks to a detailed spatial investigation of the Kondo effect, the project has the ambition to answer open questions in the Kondo problem, with possible important impact in other fields of condensed matter physics involving strongly interacting electrons, such as the physics of heavy fermions materials where the Kondo effect plays a central role [189]. From a broader point of view, investigations of interaction effects in quantum nanostructures are particularly important, both for our fundamental understanding of the matter and for applications in electronic devices in order to produce new functionalities based on quantum effects.

In addition, the Kondo effect is a coherent many-body effect which puts the impurity spin and the screening cloud into a “singlet” entangled state [190] extending over large distances for small tunneling rates. This long-range coherence property is of high interest for possible applications in the emerging field of quantum technologies [191]. A long-range Kondo entanglement between two spin qubits separated by a large distance could indeed bring an original solution to the coupling issue encountered with large networks of qubits [192]. This possibility, however, requires deeper understanding of the Kondo entanglement before planning any dedicated experimental realization, and is beyond the scope of the current proposal.

The central objective of the project is to demonstrate the existence of a long-range Kondo cloud of screening particles in the electron reservoir coupled to the QD. For a typical Kondo temperature of 300 mK, the predicted Kondo length is about $5 \mu\text{m}$, which is very large compared to nowadays available sample sizes in nanotechnology. Kondo clouds have been looked for by scanning tunneling microscopy on conducting surfaces with magnetic impurities where the expected Kondo length is much smaller [193, 194], but have never been investigated experimentally in the tunable environment of gate-defined QDs. In this project, we plan to :

1. investigate the spatial extension of the Kondo screening cloud in real space,
2. study the long-range coupling of two quantum dots in the Kondo regime,
3. demonstrate the entanglement of two spins by a common Kondo cloud.

To achieve these goals, the project combines several experimental techniques, including scanning gate microscopy (SGM), electronic transport, and high-frequency detection. These original experiments, which have never been reported in the literature, should produce high impact results. They will contribute to a better understanding of the Kondo effect from a fundamental point of view, with possible applications in future quantum electronic devices.

According to theoretical works [195, 196], the existence and extension of the Kondo cloud can be probed by charge-carrier confinement using a finite-size reservoir. For this, the SGM technique [39] provides a highly flexible way for controlling the length of a quasi-one-dimensional channel over large distances and is more suitable than a control by surface gates

[197]. The project will use this technique and measure the Kondo resonance by weakly-invasive transport spectroscopy across the QD [198] as a function of the tip position above the reservoir containing the Kondo cloud (Fig. 5.2). The periodic modulations of the Kondo resonance due to interference in the finite-size reservoir will disappear for tip distances exceeding the Kondo length. This crossover will be the signature of the existence of the cloud, with a measure of the Kondo length. This last quantity can be varied experimentally by tuning the gate voltage controlling the tunnel coupling to the reservoir. The splitting of the Kondo resonance by a parallel magnetic field will also be useful to interpret the experimental data by providing an independent energy scale.

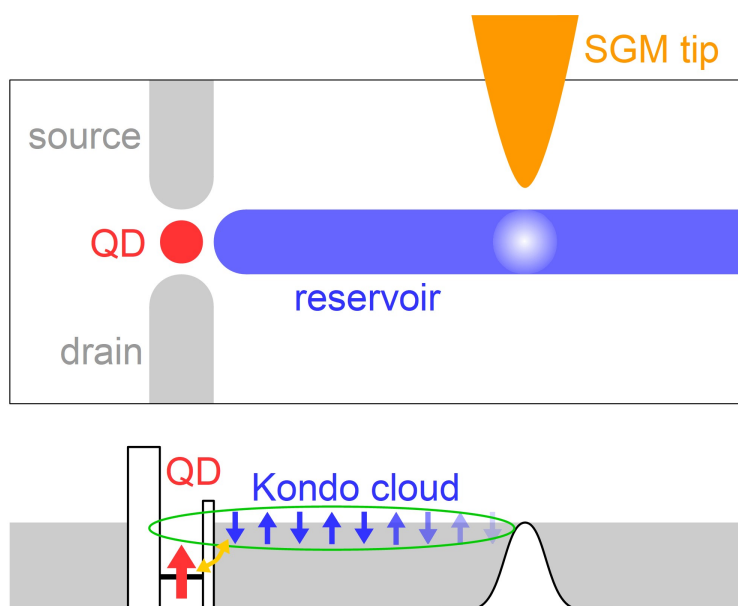


Figure 5.2: Scanning gate investigation of the Kondo cloud extension around a QD placed in the Kondo regime by strong coupling with the reservoir in blue. The tip-induced depletion area is used to vary continuously the reservoir size and probe the Kondo length ξ_K . The strength of the Kondo effect is measured by spectroscopy of the Kondo resonance using the weakly-coupled contacts in gray.

The Kondo cloud extension will also be studied by a complementary approach, based on samples with two separate QDs (Fig. 5.3), tunnel coupled to a common reservoir, and placed in the Kondo regime. For the case of small QD separation, which has already been studied [199, 200], the two spins are coupled by an effective exchange interaction, called the RKKY interaction, and the Kondo effect disappears when the coupling is antiferromagnetic since the total spin is zero. For the case of large QD separation, which has not been discussed yet in the literature, it is expected that the RKKY interaction will become negligibly small, whereas the Kondo cloud extension can be made larger than the QD separation, by reducing

the tunneling rate of the barriers. In this case, the charge parity of the right dot should influence the formation of the cloud of the left dot, which will be probed by tunneling spectroscopy using the weakly-coupled source and drain contacts. For an even number of electrons in the right dot, the Kondo cloud of the left dot should remain unchanged, while for an odd number of electrons, a single cloud should be shared by the two dots. Such a shared Kondo cloud should have very specific yet unexplored properties, that will be studied experimentally and theoretically during the project. SGM experiments will also complement this transport study by probing the spatial distribution of this shared Kondo cloud inside the common reservoir.

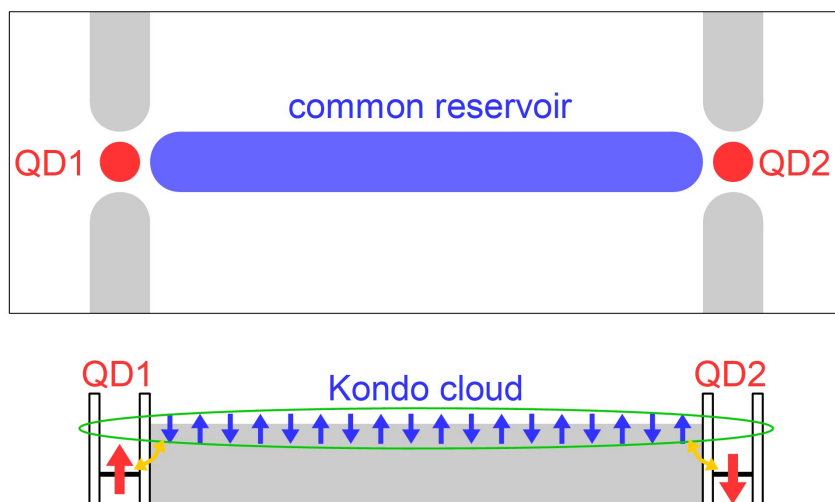


Figure 5.3: Device geometry used to probe the spatial extension of the Kondo cloud by coupling two QDs to the same reservoir in blue. The Kondo effect on each QD is measured by spectroscopy of the Kondo resonance using the weakly-coupled contacts in gray. This configuration is also used to study the interplay between the RKKY and the Kondo effects.

After having carefully analyzed the spatial extension of the Kondo cloud, the project will investigate its long-range entanglement properties using a more complex device architecture to measure the spin correlations between the two extremities of the cloud. This objective is clearly more challenging than the previous part, but is of fundamental importance in our understanding of the Kondo cloud as a “singlet” entangled state between the local spin and the conduction electrons [201]. The idea is to measure the spin correlations between two distant QDs (red dots in Fig. 5.4) connected to a common reservoir and sharing the same Kondo cloud. This scenario has been discussed theoretically in exchange-coupled spin chains, where the long-range entanglement between the spins at the two ends of the chain has been analyzed [191]. Here we propose to extend this theoretical proposal to the case of semiconductor QDs where the spin state can be measured experimentally. The spin-correlation experiment will consist in reading separately the spin states of the two QDs just

after a quench of the Kondo interaction via a fast suppression of the tunneling rates to the common reservoir. The spin states will be measured by comparison with a reference spin stored in an adjacent QD (green dots in Fig. 5.4) using the Pauli spin-blockade technique [202] and fast charge detectors [174]. The quench of the tunnel coupling should be done faster than the tunneling time (about 100 ps) to ensure that the two spins are frozen in the correlated state, whereas the spin measurement can be done on a longer time scale (about 100 μ s) thanks to the long spin relaxation time in semiconductors [203]. Observation of non-zero correlations will be the signature of the entangled nature of the Kondo cloud.

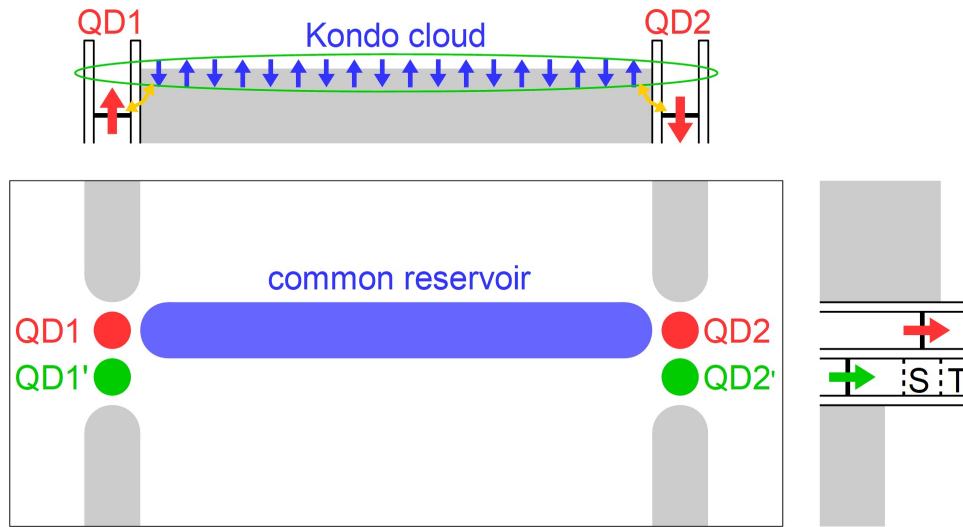


Figure 5.4: Device layout used for the measurements of spin correlations between the two red dots sharing the same Kondo cloud. The green dots serve as spin filters based on the Pauli spin-blockade technique. The single-shot charge detectors nearby the red dots are not represented.

Kondo effect in quantum dots

This section explains first the mechanism of the Kondo effect which is at the core of the project. When a spin-degenerate quantum level is occupied by a single electron and coupled to a reservoir of electrons forming a Fermi sea, the conduction electrons equilibrate the occupation probability of the spin states by exchanging particles with this quantum level in a coherent manner. This many-body process screens the spin polarization and produces an effectively non-polarized state. Originally, this phenomenon was observed as a resistance increase at very low temperature in bulk metals containing magnetic impurities and was explained theoretically by Jun Kondo in 1964. Here we will consider the case of unpaired electrons in semiconductor QDs where the Kondo effect was demonstrated for the first time in

1998 [183, 184]. The two cases differ essentially by the fact that the screening of a magnetic moment increases the backward scattering of the conduction electrons in metals, thereby increasing the resistance, whereas it enhances the forward scattering in the case of QDs, with an enhanced density of state, thereby decreasing the resistance.

The microscopic mechanism of the Kondo effect in QDs can be described as follows [185]. When the QD is in the Coulomb blockade regime with an unpaired electron spin below the Fermi level of the reservoirs, an elastic co-tunneling process can occur in which the electron of the QD is replaced by an electron from the reservoir with an opposite spin, thereby flipping the spin of the QD (Fig. 5.1). This particular co-tunneling process is strongly enhanced at low temperature, giving rise to a perfect screening of the total spin in the QD. The characteristic energy of this effect is the Kondo temperature given by the expression [204] :

$$T_K = \frac{1}{2} \sqrt{\Gamma U} e^{\frac{\pi \epsilon_0 (\epsilon_0 + U)}{\Gamma U}}$$

where $\Gamma = \Gamma_L + \Gamma_R$ is the tunneling rate between the dot and the reservoirs, U is the energy required to add another electron to the dot, and $\epsilon_0 < 0$ is the energy level occupied by the unpaired electron in the dot with respect to the Fermi level of the reservoirs. These three parameters can be tuned by the geometry and by the different gate voltages, such that the theory can be tested and verified in details experimentally. Typical values are $U = 2$ meV for small QDs, $\Gamma = 500$ μ eV for large tunneling rates, and ϵ_0 can be tuned between 0 and $-U$ upon varying the central gate of the QD. In practice, T_K can be varied between 0 and 1 Kelvin in GaAs QDs.

The screening mechanism of the Kondo effect produces a strong enhancement of the co-tunneling rate for electrons near the Fermi level, which manifests itself in transport experiments by a strong enhancement of the linear conductance, up to $2e^2/h$ for a QD with symmetric barriers. Above the Kondo temperature T_K , the zero-bias conductance decreases logarithmically down to the value similar to that of the Coulomb blockade regime with zero total spin in the dot. On the microscopic scale, the screening of the spin is perfect well below T_K and imperfect around T_K .

Another important manifestation of the Kondo effect is the peak of differential conductance in measurements as a function of the source-drain voltage. Since only conduction electrons in an energy range $k_B T_K$ around the Fermi level contribute to the screening effect (Fig. 5.1), the Kondo resonance around zero bias has a width of the order of $k_B T_K / e$ [205]. In the presence of a magnetic field, the Zeeman energy lifts the spin degeneracy and the equilibrium Kondo effect disappears. A weaker out-of-equilibrium Kondo effect then occurs, in which the screening process involves simultaneously the two reservoirs [206]. This process leads to a splitting of the Kondo resonance around zero bias by twice the Zeeman energy, a behavior which is characteristic of the Kondo effect.

First task : Kondo cloud extension

When a coherent process involves particles spread out over a finite energy range Δ , the coherence extends generally on a characteristic length scale $\hbar v_F/\Delta$ in the ballistic regime. In the case of the Kondo effect, the definition of a length scale is more subtle, and the quantity $\xi_K = \hbar v_F/k_B T_K$ does not enter into an exponential decay as usual, but instead marks the distance beyond which the correlations decrease with a larger power-law exponent [207]. This length scale is usually taken as the characteristic size of the Kondo cloud where most of the correlations are concentrated. The very existence of this length scale has been investigated by STM on surfaces containing magnetic impurities [193, 194] and the Kondo peak in the density of state was found to disappear at much shorter distance than expected. In the case of semiconductor QDs, there was no experimental study of the spatial extension of the Kondo correlations. Experiments have been proposed (Fig. 5.5) to probe the spatial extension of the Kondo cloud [195, 208, 209, 196], but they had never been realized at the time of writing this research proposal. Recently, this type of experiment has finally been performed with a QD and a set of fixed gates placed along a quasi-one-dimensional channel [188]. The result is very promising, but a lot of questions remain and justify the in-depth study proposed here.

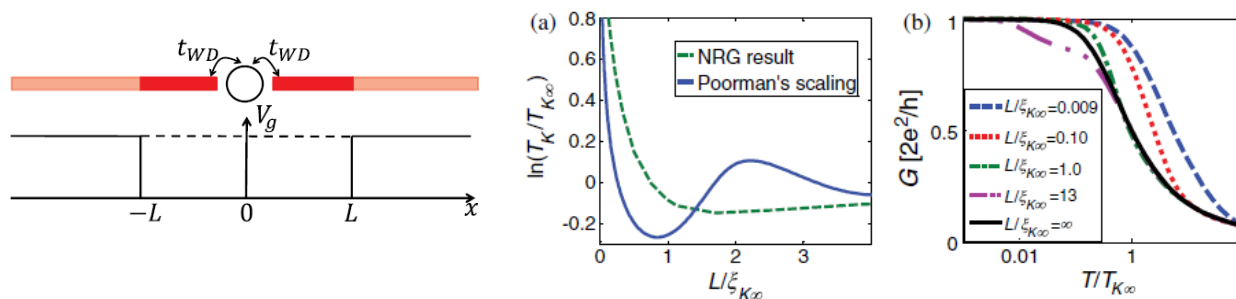


Figure 5.5: Theoretical proposal [196] for the measurement of the Kondo length ξ_K based on the influence of the reservoir length L (a) on the Kondo temperature T_K and (b) on the conductance curve versus temperature $G(T)$.

It is the first task of the project to investigate this spatial dependence of the Kondo effect. Several complementary approaches will be used to address this question, in particular using SGM to tune the length of the reservoir over a large range of distances by gating it locally (Fig. 5.2). The Kondo resonance will be probed by transport spectroscopy as a function of the tip position above the reservoir containing the Kondo cloud. By tuning the tip voltage and height, the channel can be depleted to form a finite-length reservoir affecting the Kondo resonance for tip positions inside the Kondo cloud. Periodic modulations of the Kondo resonance due to interference in the reservoir are predicted and should disappear for tip distances exceeding the Kondo length, thereby providing a signature of the existence of the Kondo cloud.

A second approach for measuring the Kondo length will be to measure the Kondo phase shift by SGM interferometry. As shown in our previous work on QPC [24], the scattering off a Kondo system induces a phase shift of the transmitted electrons at the energy of the Kondo resonance. The full Kondo phase shift $\pi/2$ is acquired by the conduction electrons only if they are crossing the entire screening cloud. Here, we thus propose to detect the extension of the Kondo cloud as the tip distance below which the phase shift no longer reaches the value of $\pi/2$ for the fully screened Kondo state. For this experiment, as opposed to the previous one, the Kondo reservoir will not be laterally confined in a channel since the Kondo resonance should not be affected by the tip-induced interference.

To perform such SGM experiments at Néel Institute, we will develop a new SGM microscope at 300 mK funded by the ANR contract “KONEX”, in complement to the existing microscope in Louvain-la-Neuve working down to 20 mK. This new SGM setup will have the possibility to work under parallel magnetic field (a configuration which has never been used) to tune the Kondo strength with a non-electrical control parameter, as an alternative to gates which are subjected to unavoidable cross-talks.

A third approach will use only surface gates (i.e. without SGM tip) in the same spirit as the recent experiment of Ref. [188]. A local gate will be placed at a fixed distance from the QD (typically 1 or 2 μm) to limit the length of the Kondo reservoir, in a similar way as in the first SGM approach above, but with less flexibility. On the other hand, this approach allows the use of a larger channel width (the SGM tip perturbation cannot block wide channels), in case the narrow channels would show poor Kondo characteristics. With such a fixed gate, the Kondo length will be varied by tuning the voltage on this gate, instead of tuning the reservoir length by moving the tip. Compared to the SGM experiment, this approach provides an alternative way to quantify the extension of the Kondo cloud.

Second task : Kondo cloud coupling

The second task of the project is to consider the interaction between two QDs placed in the Kondo regime (Fig. 5.3). The case of double QDs in direct exchange interaction through a tunnel barrier has been investigated in details, both experimentally [210, 211] and theoretically [212, 213] : if the coupling is weak, the unpaired spins of each dot produce separately a Kondo effect with their reservoirs ; if the coupling is strong and ferromagnetic (total spin $S = 1$), a common Kondo effect occurs ; if the coupling is strong and antiferromagnetic (total spin $S = 0$), no Kondo effect can take place.

In contrast, the case of two QDs separated by a small reservoir has been much less investigated, and is closely related to the situation of the present proposal. In this configuration, the conduction electrons of the common reservoir not only screen the unpaired spins of the QDs, leading to the Kondo effect, but also give rise to the Ruderman-Kittel-Kasuya-Yosida (RKKY) interaction between the two spins [200, 214, 215]. The interplay between the Kondo screening and RKKY interaction plays an important role in strongly correlated electron systems and is not trivial even in model systems such as QDs. The Kondo properties of two

QDs coupled by RKKY interaction have been studied experimentally by the group of Marcus [199]. The effect of this RKKY interaction was studied through the evolution of the Kondo peak in the conductance of the global system, interpreted as the formation of an $S = 0$ or $S = 1$ ground state for the two coupled QDs (Fig. 5.6). In this experiment, the RKKY interaction was stronger than the Kondo effect, which was only a small perturbation used to detect the RKKY interaction.

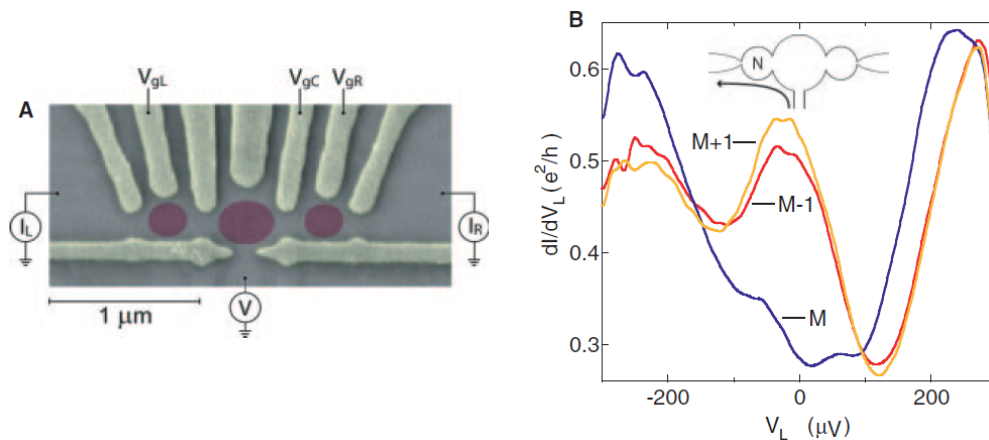


Figure 5.6: Marcus' experiment studying the RKKY coupling between two QDs [199]. The coupling is visible as a disappearance of the Kondo resonance of the left QD.

In our proposal, we consider instead the regime where the RKKY interaction is weak compared to the Kondo interaction, a situation that will be obtained with a large separation of the two dots (Fig. 5.7). We will fabricate devices with separations up to several microns (instead of 500 nm in Marcus' experiment), thanks to the long range extension of the Kondo correlations inside the Kondo cloud ($\xi_K = 5 \mu\text{m}$ for $T_K = 300 \text{ mK}$). The Kondo length and the Kondo temperature will be adjusted in-situ by tuning the gate voltage controlling the tunnel coupling between the QDs and the reservoir. This tunability will be very important to check the origin of the observed phenomena. The coupling should disappear when the Kondo length is reduced below the QDs separation.

In practice, the measurement consists in studying the Kondo effect in one dot when it is connected to the second dot by the common reservoir. For an odd number of electrons on the second dot, the local spin of this dot should participate to the Kondo cloud of the first dot and thereby influence its Kondo properties. After this coupling will have been demonstrated, it would be very interesting to consider the spatial distribution of the coupling between the two dots. For this, we will make use of the SGM technique to probe if specific paths are preferentially used to mediate the interaction. It has indeed been shown by SGM that electrons do not flow uniformly in a 2DEG even in very high mobility samples [39].

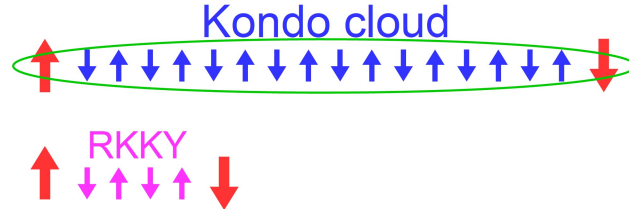


Figure 5.7: The project addresses the regime of large QDs separation where the Kondo cloud of left QD extends up to the right QD with negligible short-range RKKY coupling.

Third task : Kondo cloud entanglement

We now discuss the question of entanglement in the Kondo regime [190]. The dynamical screening of the unpaired spin of the QD by the conduction electrons of the reservoir results in a many-body ground state $|QD, FS\rangle = (|\uparrow\downarrow\rangle - |\downarrow\uparrow\rangle)/\sqrt{2}$ where the spin of the QD is entangled in a singlet state with the global spin of the Fermi sea (FS) participating to the Kondo cloud. An experiment has been recently performed on a Kondo QD coupled to a cavity showing a signature of this entanglement [197].

When two separate QDs are entangled with the same portion of Fermi sea, the three components are expected to share a common entangled state, which may be schematically expressed as $|QD1, FS, QD2\rangle = (|\uparrow\uparrow\rangle - |\downarrow\downarrow\rangle)/\sqrt{2}$. This configuration of two simultaneously entangled QDs by a Kondo cloud has not been studied theoretically yet, and we expect our project to stimulate theoretical works on this system. As a consequence of the entanglement of the two QDs, the measurement of one will determine the measurement of the other.

We propose here to perform such a correlation measurement, which is essential to demonstrate that the Kondo cloud can mediate entanglement, and to open the way for applications to qubit architectures. Conversely, the very existence of the Kondo cloud will result from the demonstration of a long-range coupling at distances of the order ξ_K . This type of experiment requires the simultaneous control of the two QDs on very short time scales to freeze out the dynamical evolution of the Kondo correlations and then to measure the spin states within the spin coherence time. The entanglement between two tunnel-coupled QDs has already been demonstrated with this correlation technique [216]. Such correlation measurements require the use of high-frequency electronics and microwave wiring in the cryogenic setup, and will be performed by our collaborators at CEA/Phelics/Lateqs [217].

More precisely, the spin entanglement between the two separate QDs sharing the same Kondo cloud will be probed by correlation measurements between the spin states measured after a quench of the Kondo coupling that isolates the two entangled spins from the reservoir. This kind of measurements requires a spin-sensitive detection such as the spin-blockade technique which is not based on magnetic field. This spin-sensitive detection requires the fabrication of two additional QDs (green dots) tunnel-coupled to the Kondo QDs (red dots)

and two QPCs (not shown) coupled electrostatically to the Kondo dots (Fig. 5.4). The spin state of the red QD is measured by comparison with a reference spin stored in the adjacent green QD using the Pauli spin-blockade technique [202]. A small parallel magnetic field is applied continuously to fix the spin direction in the green QD placed in the Coulomb-blocked regime. The energy of the singlet and triplet two-electron states are tuned such that only the singlet state can be used by an electron of the red QD to tunnel through the green QD : if the red spin is the same as the green one, the tunneling is forbidden. The red spin can therefore be measured by checking the occurrence of an interdot tunneling event versus time, using either a neighboring QPC [173] with large detection bandwidth [174] or the gate reflectometry technique [218]. This single-shot detection sensitivity is required for the correlation measurements proposed here.

The spin correlations between the two Kondo-coupled QDs will be measured by reading separately the spin state of each QD just after a quench of the Kondo coupling, induced by a fast suppression of the tunneling rates to the common reservoir. During the read-out sequence, the energy level of each red QD is adjusted such as to be in the configuration of the spin-sensitive detection described above. Observing correlations between the tunneling (or not tunneling) events on the left and right systems will provide a direct evidence of their coupling which was mediated by the common reservoir before the quench. This coupling will be studied first in the established RKKY regime, then in the Kondo regime at larger distance. Note that the complete demonstration of the Kondo-mediated entanglement requires much more complex quantum-state-tomography experiments [216] which are well beyond the scope of the present project.

The spatial-temporal propagation of the Kondo correlations after a quench in the QD Hamiltonian has been studied theoretically. The spin correlations propagate at the Fermi velocity, and the equilibrium correlation function is reached after a time scale $\tau = \hbar/k_B T_K$ controlled by the Kondo temperature [219, 220]. An interesting long-term perspective offered by the project would be to reveal this dynamics. A fast control of the Kondo entanglement between two QDs could find applications in quantum technologies to perform two-qubits operations.

Chapter 6

Projects on graphene devices

Since 2015, I am also working on the physics of graphene in collaboration with Benjamin Sacépé. With an ERC funding, he developed all the necessary equipments and processes to fabricate high mobility graphene devices. The research topics focus on quantum Hall physics in graphene in connection with proximity-induced superconductivity. In addition to transport experiments, he developed a scanning tunneling microscope (STM) that can work at very low temperature, in high magnetic field, and in ultra-high vacuum to probe the graphene properties by tunneling spectroscopy. On these research topics, I bring my expertise on mesoscopic physics in 2D systems and on scanning probe microscopies.

A first topic deals with electron optics experiments in the quantum Hall regime using gate-control beam splitters for quantum Hall edge channels. The difficulty to realize good quantum point contacts resides in the absence of band gap in graphene which allows charge transfer below the split-gate electrodes even in the quantum Hall regime. We studied the corresponding equilibration process in details in Ref. [29] and the low-magnetic-field properties of the constriction in Ref. [30]. We then studied Fabry-Perot quantum Hall interferometers made of two split-gates in series acting as the two mirrors of the optical cavity. Coherent oscillations of the current reveal the electron interference in the cavity that we studied in details in Ref. [32].

A second topic deals with the many-body ground state of the $N = 0$ Landau level in graphene. Electron interactions lift the four-fold degeneracy related to the spin and valley degrees of freedom, and various many-body ground states have been proposed theoretically at the charge neutrality point of graphene ($\nu = 0$). This ground state is usually found to be insulating, but screening the interactions with a high-dielectric-constant material (SrTiO₃) revealed a quantum spin Hall (QSH) phase with helical edge transport that we reported in Ref. [31]. This QSH phase is currently investigated by tunneling spectroscopy in the bulk of graphene and along the edges, using the AFM capabilities of the STM microscope.

In addition, we decided to carry out SGM experiments on the encapsulated graphene devices which are not accessible to STM. Two projects are currently running involving SGM on graphene :

1. One is the study of the negative electron refraction at a p-n interface in ballistic graphene at zero magnetic field, with the possible realization of a perfect planar Veselago lens. This topic uses SGM to study the trajectories in real space and their behavior at the p-n interface. This research is the PhD thesis of Marco Guerra who got a PhD grant from the GreQuE program in Fall 2017. The objectives of the project are detailed in the section 6.1.
2. The second one is a spatial investigation of electron transport in the quantum Hall regime of graphene using SGM to manipulate the edge channels. A first experiment has been performed during the PhD thesis of Marco Guerra with the help of a Master student (Akash Patil). Other experiments are planned to investigate specific questions such as the equilibration at p-n interfaces, the helical transport at $\nu = 0$ in graphene on SrTiO₃, and the formation of tip-controlled interferometers. This last topic is explained in the section 6.2.

6.1 Electron optics in ballistic graphene

Context and objective

Graphene is a monolayer of carbon where the linear dispersion relation around the Dirac points gives to electrons the properties of mass-less Dirac fermions with unique properties as compared to other materials studied in condensed matter physics. In addition, its gap-less density of states makes graphene a bipolar material with either electron-like or hole-like charge carriers depending on the sign of the doping. The density and polarity of charge carriers can be controlled by electrostatic gating to form controllable electronic devices such as bipolar transistors. For fundamental research in physics, this gate-tunability of the carrier type offers the unique possibility to study original quantum effects at low temperature, such as the specific quantum Hall effect that arises in graphene in perpendicular magnetic field.

The distinctive feature of the present project is to investigate micron-size graphene devices at zero magnetic field where charge transport is fully ballistic and coherent at low temperature. The possibility to combine ballistic effects and Dirac fermions properties makes graphene the elective material to study unusual physical effects such as negative refraction. This effect has been predicted in graphene p-n junctions and would make possible the realization of a perfect lens similar to the Veselago lens in optics (Fig. 6.1).

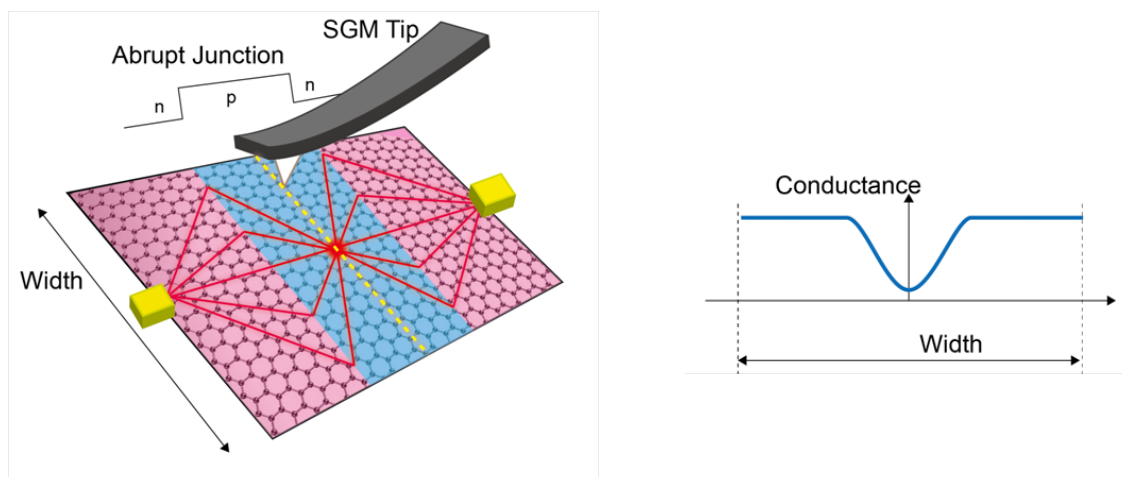


Figure 6.1: The negative refraction at the two p-n interfaces of a graphene n-p-n junction can be used to focus a divergent beam and realize an electronic equivalent of the perfect optical lens imagined by Veselago. Scanning gate microscopy will be used to image in real space this focusing effect through a drop of the conductance at the focal point.

A fundamental investigation of the refraction effect in ballistic graphene junctions is a prerequisite before the realization of new electronic devices that would be electronic analogs of optical components such as lenses, prisms, and wave guides. Importantly, the control of the

refraction effect by gate voltages would make it possible the realization of tunable components similar to the optical switches used to route light beams towards different output ports. In addition, coherent electron optics experiments at low temperature and zero magnetic field would offer exciting perspectives for both fundamental studies and applications in quantum technologies.

The originality of the present project is to use the SGM technique to image the ballistic trajectories in graphene in order to obtain a real-space demonstration of the refraction effect that a pure transport experiment could only infer indirectly. The negative refraction will be studied at the p-n interface between two regions of graphene with different carrier polarities thanks to a thin graphite bottom gate below half of the graphene device, the second half being gated by the silicon substrate. SGM will be used to image the ballistic trajectories in real space, the negative refraction at the p-n interface, and the re-focusing of the electron beam after the interface.

Sample fabrication

The technique to obtain ballistic graphene is the encapsulation of a previously exfoliated graphene flake between two flakes of hexagonal boron nitride (h-BN) using a van-der-Waals pick-up technique. The unique feature of this technique is that the surfaces around of the graphene are never put in contact with resist materials throughout the process, in contrast to non-encapsulated graphene devices where the lithography steps require covering the graphene with a layer of resist with the presence of residues after process. Moreover, the BN flakes are about 10 to 20 nm thick and define a physical separation between the graphene and the silicon oxide top layer of the substrate. In absence of separation, the presence of trapped charges in the oxide shifts randomly the Fermi level of graphene and lead to an uncontrolled and inhomogeneous carrier density. Here, the stacking technique gives rise to high electron mobility and thus very long mean free path exceeding the size of the devices.

The existing fabrication process includes the following steps : exfoliation of graphite and h-BN crystals, identification of the interesting flakes by optical microscopy, characterization of the flakes by atomic force microscopy, stacking the BN/graphene/BN heterostructure using the van-der-Waals pick up technique, e-beam lithography of a resist layer to define the device geometry, reactive ion etching of the BN/graphene/BN heterostructure, e-beam lithography of a resist layer to define the electrodes, deposition of the metallic electrodes by evaporation. Note that the electrodes are contacting the encapsulated graphene along the side walls of the heterostructure, forming one-dimensional contacts.

The stacking process is achieved by taking the top BN flake with a stamp made of PPC (polypropylene carbonate) and PDMS (polydimethylsiloxane) coated on a glass plate. This operation is performed with a dedicated microscope equipped with micro-manipulators and a sample platform with precise temperature control. The second step is to place this BN flake on top of the graphene flake and to pick-up both of them with the stamp. The third step is to deposit them on the bottom BN flake and to pick-up the three flakes. The fourth

and last step is to deposit this BN/graphene/BN sandwich on a thin graphite flake, a few nanometers thick, such that only half of the graphene flake overlaps the graphite flake, the other half being directly on top of the Si/SiO₂ substrate (Fig. 6.2).

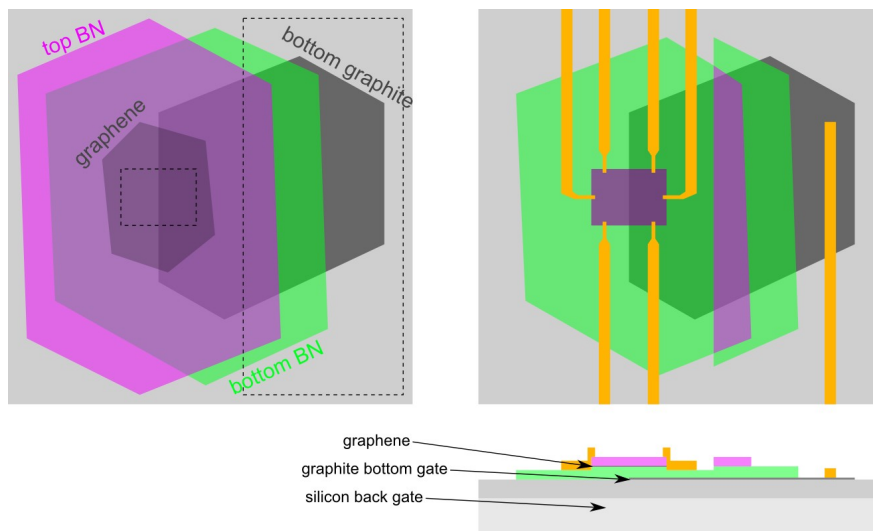


Figure 6.2: (left) Stack obtained by van-der-Waals pick-up. The dotted lines indicate the regions protected during the etching process. (right) Stack after etching and deposition of contacts. The grey flake is the graphite bottom gate used to create the p-n junction. (bottom) Cross-section of the device showing the Si/SiO₂ back gate.

SGM of the electron flow

The SGM technique has been developed to image the spatial distribution of the electron flow in 2DEG nanostructures. SGM revealed that the weak spatial fluctuations of the electrostatic potential create a complex pattern in electron trajectories instead of an homogenous spread of the current density. This inhomogeneous potential distribution is due to the charged dopants in the heterostructure and exists even in high-mobility 2DEGs. Ballistic trajectories are therefore not straight lines but smooth curves optimizing the potential landscape. Before studying the refraction effect in a p-n junction, it is therefore important to have a precise understanding of the electron trajectories in our high-mobility graphene devices. Non-ideal ballistic trajectories may arise due to the weak potential fluctuations induced by the charges in the silicon oxide of the substrate. The smooth potential variations can curve locally the trajectories and split a uniform beam into a ramified pattern of electron paths. In this study, electrons will be injected in the graphene by a small contact of a few hundreds of nanometers in order to have a small injection point on the scale of the device. SGM images of the current variations, in one of the drain contacts, as a function of the tip

position will map the spatial distribution of the inhomogeneous current density and reveal the non-ideal ballistic trajectories. Studying the correlations between patterns obtained at different carrier densities and for both charge polarities will be very interesting (and cannot be done with ungated GaAs 2DEGs). For a better understanding of the experimental results, the branched flow in the SGM images will be calculated using the quantum simulation software KWANT, which is already used in the group for the analysis of the branched flow in GaAs 2DEGs with random potential fluctuations. This software fully describes the electronic properties of graphene by considering the specific honey-comb lattice of graphene.

SGM of the electron refraction

The next step will be to perform SGM images of the current flow across the p-n interface using small source and drain contacts located on the opposite sides of the junction. The direction of a particular current path (of the branched flow described above) is expected to change abruptly at the interface, giving access to the refraction angle for the particular incident angle of this current path. The use of different combinations of source and drain contacts placed around the device will give access to a large range of incident angles in order to reconstruct the refraction law for all angles. For n-n' junctions with the same carrier polarity on both sides, the refraction angle should be of the same sign as the incident angle, but smaller for $|n| < |n'|$ and larger for $|n| > |n'|$. When the carrier type is changed to hole in the region after the interface, the incident and refraction angles should be of opposite signs, corresponding to a negative refraction effect. Note that this phenomenon can be uniquely realized in graphene thanks to its bipolar properties, using hole-type carriers with group velocity opposite to that of electrons.

Refraction is a wave effect resulting from the conservation of the electron momentum parallel to the interface. It is therefore a quantum mechanical effect, and more precisely a semi-classical effect, since it does not require long-range coherence and can be obtained by the equivalent of the Fermat's principle of geometrical optics. The refraction angle can be found with this semi-classical approach, but the details of the refraction phenomenon such as the reflection and transmission coefficients requires quantum mechanics. In case of a bipolar p-n junction in graphene, the particular shape of the potential profile at the p-n interface has a strong influence on the transmission amplitude with the formation of a transmission gap at large incident angle for smooth interfaces. This angle-dependent transmission coefficient is an important issue for the observation of the refraction effect in a large range of angles. This point will be addressed by varying the thickness of the bottom BN flake that controls the size of the region over which the carrier density is changing from n to p (this size is to be compared with the particle wavelength). Smooth interfaces present a narrow range of transmission angle, while abrupt interfaces transmit at all angles. Note that the transmission at zero angle is always perfect (equal to one) due to the absence of 180° backscattering in graphene (conservation of the pseudo-spin degree of freedom, leading to the Klein tunneling effect in case of n-p-n barriers).

SGM of the electron focusing

After this detailed investigation of the refraction phenomenon, the next logical step is to study the focusing properties of the p-n interface in presence of a wide incident beam. Contrary to usual case of positive refraction where focusing requires a curved interface, negative refraction produces focusing even for a straight interface. In the ideal case, after injecting electrons by a small contact in the n region, the p-n interface should focus the different electron trajectories onto a single point for symmetric carrier densities with $|n| = |p|$. This focal point should appear very clearly in the SGM images since the transverse distribution of the current density is concentrated in a small region of space (Fig. 6.1).

For non-symmetric carrier densities $|n| \neq |p|$, theory predicts the formation of a caustic pattern which could also be very interesting to image by SGM, together with the shift in the longitudinal direction of the optimum focal point. In addition, an interference pattern is expected in this case due to the difference in optical paths for trajectories with different incident angles. This interference pattern may also be spatially resolved in SGM images recorded at low enough temperature to have sufficient phase coherence. Note that for all these investigations of ballistic and coherent effects in graphene junctions, the KWANT simulation software will be of great help to reach a better understanding of the SGM images.

Perspectives of this work could then be to study devices forming n-p-n junctions with two interfaces using a narrow graphite bottom gate to control the density of the central region only. With such a device, it would be possible to focus a divergent beam in the middle of the central region using the first interface and then to focus it again after the second interface onto the drain contact. This situation would correspond to the exact electronic analog of the Veselago lens which has been realized using meta-materials in the field of optics. This beautiful electrical control of a coherent electron beams in free space could be of high interest for quantum technologies by enabling the coherent transfer and selective addressing of electrons between various quantum dots in a qubit array.

6.2 Quantum Hall interferometers in graphene

Context

In 2DEGs, a wealth of quantum phenomena can be observed at high magnetic fields, with the emergence of the integer and fractional quantum Hall effects. In addition to important applications as resistance standards, these effects give to physicists a unique situation where ballistic transport can be studied over macroscopic distances. The formation of Landau levels at large magnetic field indeed opens energy gaps in the electron spectrum and makes the bulk of the material insulating, while the rapid variations of the potential at the 2DEG edges push the Landau levels at the Fermi energy, thereby creating one-dimensional and unidirectional conducting edge channels. In this regime, electron transport is restricted to the edges of the samples, and to the edges of the depletion regions created by metallic gates on top of the 2DEG. The ballistic conduction through a device can therefore be controlled by split-gates forming constrictions in the 2DEG, whose transmission can be precisely tuned to allow a controlled number of edge channels to be transmitted. Another interesting situation is the tunneling regime of the QPC, where the electron wave function can be partitioned into transmitted and reflected waves. Such a beam splitter can be used for example to investigate the charge and statistics of the quasiparticles in the fractional quantum Hall regime. Using several split-gates, micron-scale electronic interferometers equivalent to the optical Mach-Zehnder or Fabry-Pérot interferometers can be fabricated, in order to investigate the electronic interactions and quantum coherence on long distances.

For a long time, this fascinating physics was restricted to high-mobility semiconductor 2DEGs in GaAs/AlGaAs heterostructures grown by molecular beam epitaxy. In the recent years, the discovery of graphene as a 2D material has been a revolution for the quantum Hall community, providing the ultimate 2DEG made of a single layer of atoms, directly accessible to surface probes like scanning tunneling microscopy, and showing new quantum Hall properties. The honey-comb lattice of graphene indeed gives to the electrons a linear dispersion relation around the six K points of the Brillouin zone, with two non-equivalent sets of three equivalent K points, and a Fermi energy located at the K points for undoped graphene. The linear dispersion gives to electrons the properties of relativistic (mass-less) Dirac fermions with a specific spectrum of Landau levels and the presence of a zero-energy Landau level. In addition, the absence of gap at the K points allows the type of carriers to be continuously changed from electron to hole. Another specificity of graphene is the four-fold degeneracy of the Landau levels, including the usual two-fold spin degeneracy and the specific two-fold valley degeneracy induced by the non-equivalent K points. After some experimental limitations in the first years due to the low electron mobility of graphene on silicon oxide substrates, the full quantum Hall properties of the intrinsic graphene can now be investigated in high mobility samples based on boron-nitride substrates. With such high sample quality, it is now possible to build quantum devices like those described above and previously limited to GaAs/AlGaAs 2DEGs. In particular, QPCs could be used to investigate the nature of

the quasiparticles in the integer and fractional quantum Hall regimes of graphene, and more sophisticated devices such as quantum Hall interferometers allow us to access the electronic interactions and the quantum coherence of electrons in the edge channels of graphene.

Objective

The objective of the project is to use SGM to create tunable quantum Hall interferometers in high-mobility graphene devices with gated constrictions. At zero magnetic field, the absence of energy gap in graphene makes the fabrication of nanostructures difficult using metallic surface gates. In large magnetic fields however, the formation of Landau levels creates gaps in the energy spectrum, such that the conducting edge channels follow the electrostatic potential of the gates. In our previous work [29], we have demonstrated the realization of quantum point contacts in the integer and fractional quantum Hall regime using a very high-mobility graphene encapsulated between boron-nitride flakes.

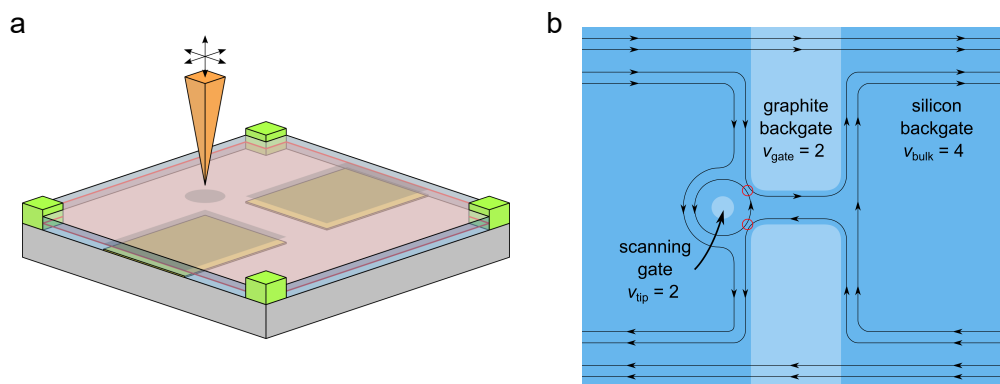


Figure 6.3: (a) Typical configuration of the SGM experiment where the tip is placed near the constriction formed by a thin graphite split-gate below the BN/graphene/BN heterostructure. (b) In this example, the electron density and magnetic field are tuned to have 4 edge channels in the bulk, the split-gate voltage is tuned to guide 2 edge channels through the constriction, and the tip voltage is also tuned to have a filling factor 2 below the tip. By placing carefully the tip with respect to the two split-gate electrodes, a quantum Hall interferometer is created around the tip-induced potential.

Here, we propose to create graphene quantum Hall interferometers by combining such a gated constriction with the tunable electrostatic potential induced by the SGM tip. In large magnetic fields, the potential perturbation induced by the SGM tip has a different effect on electron transport than at zero field, as electrons move in one-dimensional and unidirectional quantum Hall edge channels and cannot be backscattered by the tip-induced potential. Electrons below the tip are forced to turn around this potential, making small loops, which remain localized below the tip. When the tip is either far from the edges or close

to a single edge of the device, these loops do not change the device conductance, since the two counter-propagating edge channels (flowing on the opposite sides of the device) are not connected. By adding a split-gate on the sample to create a constriction, these two counter-propagating edge channels are forced to pass close to each other, and can be connected in a controlled way by placing the SGM tip close to the constriction (Fig. 6.3).

Since the edge channels will form loops along the equipotential lines of the tip-induced potential hill, they will acquire a quantum phase. Placing the SGM tip close to the QPC will couple these loops to the edge channels flowing along the QPC gates, such that quantum interference in the loops can be detected by measuring the device conductance. The selective gate-tunable transmission of the edge channels through the QPC will allow us to investigate the coherence of each individual edge channel, their symmetry and mutual interactions. As compared to similar investigations done previously in GaAs/AlGaAs 2DEGs [75], the graphene platform presents a higher tunability in term of carrier density and carrier polarity. The four-fold symmetry of Dirac fermions in graphene also provides new physics related to the lifting of these degeneracies by electron interactions. The investigation of small-size tip-induced quantum Hall interferometers in graphene would thus be of great interest.

Description

In the experimental configuration shown in Fig. 6.4a, the tip will be placed close to the constriction such that the edge channels flowing along the QPC gates will be tunnel-coupled to the edge channels forming loops around the tip position. The quantum interference of the electron waves in these closed-loops will be controlled by the tip voltage and the tip height above the surface, and also by the precise value of the magnetic field. In order to have this interference process visible in the overall transmission of the device, the loop has to be coupled simultaneously to the two counter-propagating edge channels of the devices, which occurs when the tip is placed at an equal distance from the two gates. By controlling precisely the distance between the tip and the gates, the coupling can be tuned from the weak-tunneling regime up to the half-transmission regime.

With this unique experiment in hand, the coherence length of the edge channel in the loop can be measured by analyzing the interference visibility as a function of the loop size. These coherence properties will give us information on the interactions between the various edge channels, belonging either to different Landau levels, or within the same level but with different spin and valley indexes. The existence of inter- and intra-Landau level interactions in graphene has already been demonstrated using p-n and p-n-p junctions created with large gates. The observed deviations of the conductance from the ideal case have been successfully explained by a process of current equilibration between co-propagating edge channels. The microscopic mechanism of this equilibration process is however still to be investigated, and the present project aims at answering this question by measuring directly the inelastic interactions between edge channels via their influence on the coherence length in interferometric experiments.

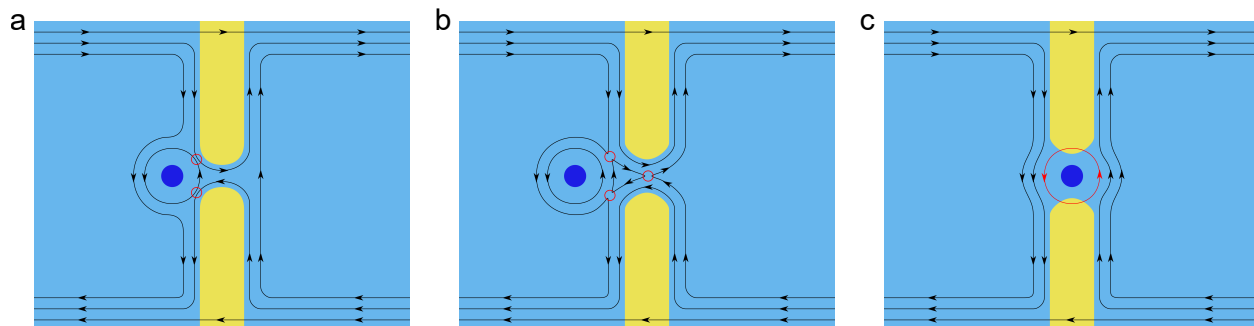


Figure 6.4: (a) Quantum Hall interferometer around the tip-induced potential, measured by the backscattering at the constriction. (b) Small QH island between the split-gate electrodes and the tip, with possible Coulomb blockade. (c) Tip-induced charge transfer by equilibration between co-propagating edge channels, with tunable position and inter-edge-channel distance.

To achieve this goal, the total number N_0 of edge channels in the bulk of the graphene will be controlled by tuning the magnetic field and the back-gate voltage. Then, a particular edge channel will be selected by the split-gate voltage such as to be transmitted through the constriction, while a number N_1 of outer channels will flow freely below the gates and a number N_2 of inner channels will be totally reflected ($N_0 = N_1 + N_2 + 1$). The tip position will then be adjusted such that this particular edge channel makes a loop below the tip and is coupled to the channel flowing through the constriction. In this way, we can choose which particular edge channel to be probed by the interferometer, and choose independently the number N_2 of edge channels flowing around the loop that will interact with it. By tuning the tip voltage, a number N_3 of edge channels (between 0 and N_1) can also be induced inside the loop and interact with it (not shown in the figure). The size of the loop will be varied from a few hundred nanometers up to several microns by varying in-situ the height of the tip above the surface. The profile of the tip-induced potential will have an influence on the separation between the edge channels and thus on their mutual interactions, and will be controlled by the tip voltage and the tip height.

To demonstrate the potentiality offered by this SGM investigation of QH interferometers, Fig. 6.4b shows another geometry of quantum Hall interferometer where a loop is created between the tip and the two split-gate electrodes, with three coupling points to the bulk edge channels. Compared to the previous case, the position of the tip has been slightly shifted to the left and the gap between the QPC gates has been slightly increased in order to have the inner edge channel in the bulk forming a small loop in the middle. A precise tuning of all the parameters will therefore be necessary to obtain the desired configuration of edge channels and interpret correctly the data of the interferometry experiments. In this configuration, the loop can be made very small and will therefore present strong Coulomb interactions. Such quantum Hall Coulomb islands have been studied by SGM in semiconductor 2DEGs (see

chapter 3.4) and we could therefore investigate this effect also in graphene.

Fig. 6.4c shows an interesting geometry where the tip induces a full depletion of the electron-type carriers inside the constriction. Charge transfer between co-propagating edge channels would allow current to be transmitted through the interfering loop. This leakage current corresponds to the equilibration process at play in n-p-n junctions, and could be studied here in real space along the junction by replacing the split-gate by a single gate.

Bibliography

- [1] H. Sellier, C. Baraduc, F. Lefloch, and R. Calemczuk, *Temperature-induced crossover between 0 and π states in S/F/S junctions*, Physical Review B **68**, 054531 (2003).→
- [2] H. Sellier, C. Baraduc, F. Lefloch, and R. Calemczuk, *Half-integer Shapiro steps at the $0 - \pi$ crossover of a ferromagnetic Josephson junction*, Physical Review Letters **92**, 257005 (2004).→
- [3] L. Crétonin, A. K. Gupta, H. Sellier, F. Lefloch, M. Fauré, A. Buzdin, and H. Courtois, *Scanning tunneling spectroscopy of the superconducting proximity effect in a diluted ferromagnetic alloy*, Physical Review B **72**, 024511 (2005).→
- [4] H. Sellier, G. P. Lansbergen, J. Caro, S. Rogge, N. Collaert, I. Ferain, M. Jurczak, and S. Biesemans, *Transport spectroscopy of a single dopant in a gated silicon nanowire*, Physical Review Letters **97**, 206805 (2006).→
- [5] H. Sellier, G. P. Lansbergen, J. Caro, S. Rogge, N. Collaert, I. Ferain, M. Jurczak, and S. Biesemans, *Subthreshold channels at the edges of nanoscale triple-gate silicon transistors*, Applied Physics Letters **90**, 073502 (2007).→
- [6] B. Hackens, F. Martins, T. Ouisse, H. Sellier, S. Bollaert, X. Wallart, A. Cappy, J. Chevrier, V. Bayot, and S. Huant, *Imaging and controlling electron transport inside a quantum ring*, Nature Physics **2**, 826–830 (2006).→
- [7] F. Martins, B. Hackens, M. G. Pala, T. Ouisse, H. Sellier, X. Wallart, S. Bollaert, A. Cappy, J. Chevrier, V. Bayot, and S. Huant, *Imaging electron wave functions inside open quantum rings*, Physical Review Letters **99**, 136807 (2007).→
- [8] M. G. Pala, B. Hackens, F. Martins, H. Sellier, V. Bayot, S. Huant, and T. Ouisse, *Local density of states in mesoscopic samples from scanning gate microscopy*, Physical Review B **77**, 125310 (2008).→
- [9] M. G. Pala, S. Baltazar, F. Martins, B. Hackens, H. Sellier, T. Ouisse, V. Bayot, and S. Huant, *Scanning gate microscopy of quantum rings: effects of an external magnetic field and of charged defects*, Nanotechnology **20**, 264021 (2009).→

Bibliography

- [10] H. Sellier, B. Hackens, M. Pala, and S. Huant, *Imager les interférences quantiques dans les semiconducteurs*, Images de la Physique, CNRS, 2009, p. 49.→
- [11] H. Sellier, B. Hackens, M. G. Pala, F. Martins, S. Baltazar, X. Wallart, L. Desplanque, V. Bayot, and S. Huant, *On the imaging of electron transport in semiconductor quantum structures by scanning-gate microscopy: successes and limitations*, Semiconductor Science and Technology **26**, 064008 (2011).→
- [12] F. Martins, H. Sellier, M. G. Pala, B. Hackens, V. Bayot, and S. Huant, *Scanning probe electronic imaging of lithographically patterned quantum rings*, Physics of quantum rings (V. M. Fomin, ed.), Springer Nature, aug 2013, pp. 107–121.→
- [13] B. Hackens, F. Martins, S. Faniel, C. A. Dutu, H. Sellier, S. Huant, M. Pala, L. Desplanque, X. Wallart, and V. Bayot, *Imaging Coulomb islands in a quantum Hall interferometer*, Nature Communications **1**, 39 (2010).→
- [14] F. Martins, S. Faniel, B. Rosenow, M. G. Pala, H. Sellier, S. Huant, L. Desplanque, X. Wallart, V. Bayot, and B. Hackens, *Scanning gate spectroscopy of transport across a quantum Hall nano-island*, New Journal of Physics **15**, 013049 (2013).→
- [15] F. Martins, S. Faniel, B. Rosenow, H. Sellier, S. Huant, M. G. Pala, L. Desplanque, X. Wallart, V. Bayot, and B. Hackens, *Coherent tunnelling across a quantum point contact in the quantum Hall regime*, Scientific Reports **3**, 1416 (2013).→
- [16] P. Liu, *Etude du transport électronique dans les nanodispositifs semiconducteurs par microscopie à grille locale*, Ph.D. thesis, Université de Grenoble, 2011.
- [17] L. Desplanque, D. Vignaud, S. Godey, E. Cadio, S. Plissard, X. Wallart, P. Liu, and H. Sellier, *Electronic properties of the high electron mobility $Al_{0.56}In_{0.44}Sb/Ga_{0.5}In_{0.5}Sb$ heterostructure*, Journal of Applied Physics **108**, 043704 (2010).→
- [18] M. G. Pala, S. Baltazar, P. Liu, H. Sellier, B. Hackens, F. Martins, V. Bayot, X. Wallart, L. Desplanque, and S. Huant, *Transport inefficiency in branched-out mesoscopic networks: an analog of the Braess paradox*, Physical Review Letters **108**, 076802 (2012).→
- [19] M. G. Pala, H. Sellier, B. Hackens, F. Martins, V. Bayot, and S. Huant, *A new transport phenomenon in nanostructures: a mesoscopic analog of the Braess paradox encountered in road networks*, Nanoscale Research Letters **7**, 472 (2012).→
- [20] S. Toussaint, F. Martins, S. Faniel, M. G. Pala, L. Desplanque, X. Wallart, H. Sellier, S. Huant, V. Bayot, and B. Hackens, *On the origins of transport inefficiencies in mesoscopic networks*, Scientific Reports **8**, 3017 (2018).→

-
- [21] P. Liu, F. Martins, B. Hackens, L. Desplanque, X. Wallart, M. G. Pala, S. Huant, V. Bayot, and H. Sellier, *Formation of quantum dots in the potential fluctuations of InGaAs heterostructures probed by scanning gate microscopy*, Physical Review B **91**, 075313 (2015).→
- [22] B. Brun, *Electron interactions in mesoscopic physics: scanning gate microscopy and interferometry at a quantum point contact*, Ph.D. thesis, Université de Grenoble, 2014.
- [23] B. Brun, F. Martins, S. Faniel, B. Hackens, G. Bachelier, A. Cavanna, C. Ulysse, A. Ouerghi, U. Gennser, D. Mailly, S. Huant, V. Bayot, M. Sanquer, and H. Sellier, *Wigner and Kondo physics in quantum point contacts revealed by scanning gate microscopy*, Nature Communications **5**, 4290 (2014).→
- [24] B. Brun, F. Martins, S. Faniel, B. Hackens, A. Cavanna, C. Ulysse, A. Ouerghi, U. Gennser, D. Mailly, P. Simon, S. Huant, V. Bayot, M. Sanquer, and H. Sellier, *Electron phase shift at the zero-bias anomaly of quantum point contacts*, Physical Review Letters **116**, 136801 (2016).→
- [25] B. Brun, F. Martins, S. Faniel, A. Cavanna, C. Ulysse, A. Ouerghi, U. Gennser, D. Mailly, P. Simon, S. Huant, M. Sanquer, H. Sellier, V. Bayot, and B. Hackens, *Thermoelectric scanning-gate interferometry on a quantum point contact*, Physical Review Applied **11**, 034069 (2019).→
- [26] K. Kolasinski, B. Szafran, B. Brun, and H. Sellier, *Interference features in scanning gate conductance maps of quantum point contacts with disorder*, Physical Review B **94**, 075301 (2016).→
- [27] K. Kolasinski, H. Sellier, and B. Szafran, *Conductance measurement of spin-orbit coupling in two-dimensional electron systems with an in-plane magnetic field*, Physical Review B **94**, 121304(R) (2016).→
- [28] K. Kolasinski, H. Sellier, and B. Szafran, *Extraction of the Rashba spin-orbit coupling constant from scanning gate microscopy conductance maps for quantum point contacts*, Scientific Reports **7**, 14935 (2017).→
- [29] K. Zimmermann, A. Jordan, F. Gay, K. Watanabe, T. Taniguchi, Z. Han, V. Bouchiat, H. Sellier, and B. Sacépé, *Tunable transmission of quantum Hall edge channels with full degeneracy lifting in split-gated graphene devices*, Nature Communications **8**, 14983 (2017).→
- [30] L. Veyrat, A. Jordan, K. Zimmermann, F. Gay, K. Watanabe, T. Taniguchi, H. Sellier, and B. Sacépé, *Low-magnetic-field regime of a gate-defined constriction in high-mobility graphene*, Nano Letters **19**, 635 (2019).→

- [31] L. Veyrat, C. Déprez, A. Coissard, X. Li, F. Gay, K. Watanabe, T. Taniguchi, Z. Han, B. A. Piot, H. Sellier, and B. Sacépé, *Helical quantum Hall phase in graphene on SrTiO₃*, *Science* **367**, 781–786 (2020).→
- [32] C. Déprez, L. Veyrat, H. Vignaud, G. Nayak, K. Watanabe, T. Taniguchi, F. Gay, H. Sellier, and B. Sacépé, *A tunable Fabry–Pérot quantum Hall interferometer in graphene*, *Nature nanotechnology*, 1–8 (2021).→
- [33] J. Laurent, *Mesures de la force de Casimir à basse température*, Ph.D. thesis, Université de Grenoble, 2010.
- [34] J. Laurent, A. Mosset, O. Arcizet, J. Chevrier, S. Huant, and H. Sellier, *Negative backaction noise in interferometric detection of a microlever*, *Physical Review Letters* **107**, 050801 (2011).→
- [35] J. Laurent, A. Drezet, H. Sellier, J. Chevrier, and S. Huant, *Large variation in the boundary-condition slippage for a rarefied gas flowing between two surfaces*, *Physical Review Letters* **107**, 164501 (2011).→
- [36] J. Laurent, H. Sellier, A. Mosset, S. Huant, and J. Chevrier, *Casimir force measurements in Au–Au and Au–Si cavities at low temperature*, *Physical Review B* **85**, 035426 (2012).→
- [37] M. A. Eriksson, R. G. Beck, M. Topinka, J. A. Katine, R. M. Westervelt, K. L. Campman, and A. C. Gossard, *Cryogenic scanning probe characterization of semiconductor nanostructures*, *Applied Physics Letters* **69**, 671–673 (1996).→
- [38] M. A. Topinka, B. J. LeRoy, S. E. J. Shaw, E. J. Heller, R. M. Westervelt, K. D. Maranowski, and A. C. Gossard, *Imaging Coherent Electron Flow from a Quantum Point Contact*, *Science* **289**, 2323–2326 (2000).→
- [39] M. A. Topinka, B. J. LeRoy, R. M. Westervelt, S. E. J. Shaw, R. Fleischmann, E. J. Heller, K. D. Maranowski, and A. C. Gossard, *Coherent branched flow in a two-dimensional electron gas*, *Nature* **410**, 183–186 (2001).→
- [40] B. J. LeRoy, A. C. Bleszynski, K. E. Aidala, R. M. Westervelt, A. Kalben, E. J. Heller, S. E. J. Shaw, K. D. Maranowski, and A. C. Gossard, *Imaging Electron Interferometer*, *Physical Review Letters* **94**, 126801 (2005).→
- [41] K. E. Aidala, R. E. Parrott, T. Kramer, E. J. Heller, R. M. Westervelt, M. P. Hanson, and A. C. Gossard, *Imaging magnetic focusing of coherent electron waves*, *Nature Physics* **3**, 464–468 (2007).→
- [42] P. Fallahi, A. C. Bleszynski, R. M. Westervelt, J. Huang, J. D. Walls, E. J. Heller, M. Hanson, and A. C. Gossard, *Imaging a Single-Electron Quantum Dot*, *Nano Letters* **5**, 223–226 (2005).→

-
- [43] A. C. Bleszynski, F. A. Zwanenburg, R. M. Westervelt, A. L. Roest, E. P. A. M. Bakkers, and L. P. Kouwenhoven, *Scanned Probe Imaging of Quantum Dots inside InAs Nanowires*, Nano Letters **7**, 2559–2562 (2007).→
- [44] J. Berezovsky, M. F. Borunda, E. J. Heller, and R. M. Westervelt, *Imaging coherent transport in graphene (part I): mapping universal conductance fluctuations*, Nanotechnology **21**, 274013 (2010).→
- [45] S. Bhandari, G.-H. Lee, A. Klales, K. Watanabe, T. Taniguchi, E. Heller, P. Kim, and R. M. Westervelt, *Imaging Cyclotron Orbits of Electrons in Graphene*, Nano Letters **16**, 1690–1694 (2016).→
- [46] S. Bhandari, G. H. Lee, K. Watanabe, T. Taniguchi, P. Kim, and R. M. Westervelt, *Imaging electron flow from collimating contacts in graphene*, 2D Materials **5**, 021003 (2018).→
- [47] S. Bhandari, G.-H. Lee, K. Watanabe, T. Taniguchi, P. Kim, and R. M. Westervelt, *Imaging Andreev Reflection in Graphene*, Nano Letters **20**, 4890-4894 (2020).→
- [48] M. P. Jura, M. A. Topinka, L. Urban, A. Yazdani, H. Shtrikman, L. N. Pfeiffer, K. W. West, and D. Goldhaber-Gordon, *Unexpected features of branched flow through high-mobility two-dimensional electron gases*, Nature Physics **3**, 841–845 (2007).→
- [49] M. P. Jura, M. A. Topinka, M. Grobis, L. N. Pfeiffer, K. W. West, and D. Goldhaber-Gordon, *Electron interferometer formed with a scanning probe tip and quantum point contact*, Physical Review B **80**, 041303 (2009).→
- [50] M. P. Jura, M. Grobis, M. A. Topinka, L. N. Pfeiffer, K. W. West, and D. Goldhaber-Gordon, *Spatially probed electron-electron scattering in a two-dimensional electron gas*, Physical Review B **82**, 155328 (2010).→
- [51] A. G. F. Garcia, M. König, D. Goldhaber-Gordon, and K. Todd, *Scanning gate microscopy of localized states in wide graphene constrictions*, Physical Review B **87**, 085446 (2013).→
- [52] M. König, M. Baenninger, A. G. F. Garcia, N. Harjee, B. L. Pruitt, C. Ames, P. Leubner, C. Brüne, H. Buhmann, L. W. Molenkamp, and D. Goldhaber-Gordon, *Spatially Resolved Study of Backscattering in the Quantum Spin Hall State*, Physical Review X **3**, 021003 (2013).→
- [53] R. Crook, C. G. Smith, C. H. W. Barnes, M. Y. Simmons, and D. A. Ritchie, *Imaging diffraction-limited electronic collimation from a non-equilibrium one-dimensional ballistic constriction*, Journal of Physics: Condensed Matter **12**, L167 (2000).→

- [54] R. Crook, C. G. Smith, M. Y. Simmons, and D. A. Ritchie, *Imaging cyclotron orbits and scattering sites in a high-mobility two-dimensional electron gas*, Physical Review B **62**, 5174–5178 (2000).→
- [55] R. Crook, C. G. Smith, A. C. Graham, I. Farrer, H. E. Beere, and D. A. Ritchie, *Imaging Fractal Conductance Fluctuations and Scarred Wave Functions in a Quantum Billiard*, Physical Review Letters **91**, 246803 (2003).→
- [56] R. Crook, A. C. Graham, C. G. Smith, I. Farrer, H. E. Beere, and D. A. Ritchie, *Erasable electrostatic lithography for quantum components*, Nature **424**, 751–754 (2003).→
- [57] R. Crook, J. Prance, K. J. Thomas, S. J. Chorley, I. Farrer, D. A. Ritchie, M. Pepper, and C. G. Smith, *Conductance Quantization at a Half-Integer Plateau in a Symmetric GaAs Quantum Wire*, Science **312**, 1359–1362 (2006).→
- [58] M. R. Connolly, K. L. Chiou, C. G. Smith, D. Anderson, G. A. C. Jones, A. Lombardo, A. Fasoli, and A. C. Ferrari, *Scanning gate microscopy of current-annealed single layer graphene*, Applied Physics Letters **96**, 113501 (2010).→
- [59] Z. Dou, S. Morikawa, A. Cresti, S.-W. Wang, C. G. Smith, C. Melios, O. Kazakova, K. Watanabe, T. Taniguchi, S. Masubuchi, T. Machida, and M. R. Connolly, *Imaging Bulk and Edge Transport near the Dirac Point in Graphene Moiré Superlattices*, Nano Letters **18**, 2530–2537 (2018).→
- [60] S. Morikawa, Z. Dou, S.-W. Wang, C. G. Smith, K. Watanabe, T. Taniguchi, S. Masubuchi, T. Machida, and M. R. Connolly, *Imaging ballistic carrier trajectories in graphene using scanning gate microscopy*, Applied Physics Letters **107**, 243102 (2015).→
- [61] A. Pioda, S. Kicin, T. Ihn, M. Sigrist, A. Fuhrer, K. Ensslin, A. Weichselbaum, S. E. Ulloa, M. Reinwald, and W. Wegscheider, *Spatially Resolved Manipulation of Single Electrons in Quantum Dots Using a Scanned Probe*, Physical Review Letters **93**, 216801 (2004).→
- [62] A. E. Gildemeister, T. Ihn, R. Schleser, K. Ensslin, D. C. Driscoll, and A. C. Gossard, *Imaging a coupled quantum dot-quantum point contact system*, Journal of Applied Physics **102**, 083703 (2007).→
- [63] A. Pioda, S. Kičín, D. Brunner, T. Ihn, M. Sigrist, K. Ensslin, M. Reinwald, and W. Wegscheider, *Discrete charging of traps visualized by scanning gate experiments on a quantum point contact*, Physical Review B **75**, 045433 (2007).→
- [64] A. E. Gildemeister, T. Ihn, M. Sigrist, K. Ensslin, D. C. Driscoll, and A. C. Gossard, *Measurement of the tip-induced potential in scanning gate experiments*, Physical Review B **75**, 195338 (2007).→

-
- [65] S. Schnez, J. Güttinger, M. Huefner, C. Stampfer, K. Ensslin, and T. Ihn, *Imaging localized states in graphene nanostructures*, Physical Review B **82**, 165445 (2010).→
- [66] S. Schnez, C. Rössler, T. Ihn, K. Ensslin, C. Reichl, and W. Wegscheider, *Imaging the lateral shift of a quantum point contact using scanning gate microscopy*, Physical Review B **84**, 195322 (2011).→
- [67] A. A. Kozikov, D. Weinmann, C. Rössler, T. Ihn, K. Ensslin, C. Reichl, and W. Wegscheider, *Imaging magnetoelectric subbands in ballistic constrictions*, New Journal of Physics **15**, 083005 (2013).→
- [68] A. A. Kozikov, R. Steinacher, C. Rössler, T. Ihn, K. Ensslin, C. Reichl, and W. Wegscheider, *Locally induced quantum interference in scanning gate experiments*, New Journal of Physics **16**, 053031 (2014).→
- [69] A. A. Kozikov, C. Rössler, T. Ihn, K. Ensslin, C. Reichl, and W. Wegscheider, *Interference of electrons in backscattering through a quantum point contact*, New Journal of Physics **15**, 013056 (2013).→
- [70] A. A. Kozikov, R. Steinacher, C. Rössler, T. Ihn, K. Ensslin, C. Reichl, and W. Wegscheider, *Mode Specific Backscattering in a Quantum Point Contact*, Nano Letters **15**, 7994–7999 (2015).→
- [71] R. Steinacher, A. A. Kozikov, C. Rössler, C. Reichl, W. Wegscheider, K. Ensslin, and T. Ihn, *Scanning gate imaging in confined geometries*, Physical Review B **93**, 085303 (2016).→
- [72] R. Steinacher, C. Pörtl, T. Krähenmann, A. Hofmann, C. Reichl, W. Zwerger, W. Wegscheider, R. A. Jalabert, K. Ensslin, D. Weinmann, and T. Ihn, *Scanning gate experiments: From strongly to weakly invasive probes*, Phys. Rev. B **98**, 075426 (2018).→
- [73] C. Gold, A. Kurzmann, K. Watanabe, T. Taniguchi, K. Ensslin, and T. Ihn, *Scanning gate microscopy of localized states in a gate-defined bilayer graphene channel*, Phys. Rev. Research **2**, 043380 (2020).→
- [74] A. Baumgartner, T. Ihn, K. Ensslin, K. Maranowski, and A. C. Gossard, *Quantum Hall effect transition in scanning gate experiments*, Physical Review B **76**, 085316 (2007).→
- [75] N. Pascher, F. Timpu, C. Rössler, T. Ihn, K. Ensslin, C. Reichl, and W. Wegscheider, *Resonant electron tunneling in a tip-controlled potential landscape*, Physical Review B **89**, 245408 (2014).→
- [76] N. Pascher, C. Rössler, T. Ihn, K. Ensslin, C. Reichl, and W. Wegscheider, *Imaging the Conductance of Integer and Fractional Quantum Hall Edge States*, Physical Review X **4**, 011014 (2014).→

- [77] B. A. Braem, F. M. D. Pellegrino, A. Principi, M. Rössli, C. Gold, S. Hennel, J. V. Koski, M. Berl, W. Dietsche, W. Wegscheider, M. Polini, T. Ihn, and K. Ensslin, *Scanning gate microscopy in a viscous electron fluid*, Phys. Rev. B **98**, 241304 (2018).→
- [78] N. Paradiso, S. Heun, S. Roddaro, D. Venturelli, F. Taddei, V. Giovannetti, R. Fazio, G. Biasiol, L. Sorba, and F. Beltram, *Spatially resolved analysis of edge-channel equilibration in quantum Hall circuits*, Physical Review B **83**, 155305 (2011).→
- [79] N. Paradiso, S. Heun, S. Roddaro, L. Sorba, F. Beltram, G. Biasiol, L. N. Pfeiffer, and K. W. West, *Imaging Fractional Incompressible Stripes in Integer Quantum Hall Systems*, Physical Review Letters **108**, 246801 (2012).→
- [80] A. Iagallo, N. Paradiso, S. Roddaro, C. Reichl, W. Wegscheider, G. Biasiol, L. Sorba, F. Beltram, and S. Heun, *Scanning gate imaging of quantum point contacts and the origin of the 0.7 anomaly*, Nano Research **8**, 948–956 (2015).→
- [81] L. Bours, S. Guiducci, A. Mreńca-Kolasińska, B. Szafran, J. C. Maan, and S. Heun, *Manipulating quantum Hall edge channels in graphene through scanning gate microscopy*, Phys. Rev. B **96**, 195423 (2017).→
- [82] N. Aoki, C. R. D. Cunha, R. Akis, D. K. Ferry, and Y. Ochiai, *Scanning gate microscopy investigations on an InGaAs quantum point contact*, Applied Physics Letters **87**, 223501 (2005).→
- [83] N. Aoki, C. R. da Cunha, R. Akis, D. K. Ferry, and Y. Ochiai, *Imaging of integer quantum Hall edge state in a quantum point contact via scanning gate microscopy*, Physical Review B **72**, 155327 (2005).→
- [84] C. R. da Cunha, N. Aoki, T. Morimoto, Y. Ochiai, R. Akis, and D. K. Ferry, *Imaging of quantum interference patterns within a quantum point contact*, Applied Physics Letters **89**, 242109 (2006).→
- [85] N. Aoki, R. Brunner, A. M. Burke, R. Akis, R. Meisels, D. K. Ferry, and Y. Ochiai, *Direct Imaging of Electron States in Open Quantum Dots*, Physical Review Letters **108**, 136804 (2012).→
- [86] C. Chuang, M. Matsunaga, F.-H. Liu, T.-P. Woo, N. Aoki, L.-H. Lin, B.-Y. Wu, Y. Ochiai, and C.-T. Liang, *Probing weak localization in chemical vapor deposition graphene wide constriction using scanning gate microscopy*, Nanotechnology **27**, 075601 (2016).→
- [87] T. Tomimatsu, K. Hashimoto, S. Taninaka, S. Nomura, and Y. Hirayama, *Probing the breakdown of topological protection: Filling-factor-dependent evolution of robust quantum Hall incompressible phases*, Phys. Rev. Research **2**, 013128 (2020).→

-
- [88] M. T. Woodside, C. Vale, P. L. McEuen, C. Kadow, K. D. Maranowski, and A. C. Gosard, *Imaging interedge-state scattering centers in the quantum Hall regime*, Physical Review B **64**, 041310 (2001).→
- [89] M. T. Woodside and P. L. McEuen, *Scanned Probe Imaging of Single-Electron Charge States in Nanotube Quantum Dots*, Science **296**, 1098–1101 (2002).→
- [90] D. Cabosart, S. Faniel, F. Martins, B. Brun, A. Felten, V. Bayot, and B. Hackens, *Imaging coherent transport in a mesoscopic graphene ring*, Physical Review B **90**, 205433 (2014).→
- [91] B. Brun, N. Moreau, S. Somanchi, V.-H. Nguyen, K. Watanabe, T. Taniguchi, J.-C. Charlier, C. Stampfer, and B. Hackens, *Imaging Dirac fermions flow through a circular Veselago lens*, Phys. Rev. B **100**, 041401 (2019).→
- [92] S. E. J. Shaw, R. Fleischmann, and E. J. Heller, *Quantum Coherence Beyond the Thermal Length*, arXiv:cond-mat/0105354, 2001.→
- [93] B. Liu and E. J. Heller, *Stability of Branched Flow from a Quantum Point Contact*, Physical Review Letters **111**, 236804 (2013).→
- [94] E. Heller, *Physics of waves: Warning from the deep*, Nature Physics **12**, 824–825 (2016).→
- [95] A. Freyn, I. Kleftogiannis, and J.-L. Pichard, *Scanning Gate Microscopy of a Nanostructure Where Electrons Interact*, Physical Review Letters **100**, 226802 (2008).→
- [96] A. About, G. Lemarié, and J.-L. Pichard, *Thermal Enhancement of Interference Effects in Quantum Point Contacts*, Physical Review Letters **106**, 156810 (2011).→
- [97] A. Kleshchonok, G. Fleury, J.-L. Pichard, and G. Lemarié, *Scanning gate microscopy of quantum contacts under parallel magnetic field: Beating patterns between spin-split transmission peaks or channel openings*, Physical Review B **91**, 125416 (2015).→
- [98] R. A. Jalabert, W. Szewc, S. Tomsovic, and D. Weinmann, *What Is Measured in the Scanning Gate Microscopy of a Quantum Point Contact?*, Physical Review Letters **105**, 166802 (2010).→
- [99] C. Gorini, R. A. Jalabert, W. Szewc, S. Tomsovic, and D. Weinmann, *Theory of scanning gate microscopy*, Physical Review B **88**, 035406 (2013).→
- [100] C. Gorini, D. Weinmann, and R. A. Jalabert, *Scanning-gate-induced effects in nonlinear transport through nanostructures*, Physical Review B **89**, 115414 (2014).→

- [101] C. Pörtl, A. Kozikov, K. Ensslin, T. Ihn, R. A. Jalabert, C. Reichl, W. Wegscheider, and D. Weinmann, *Classical origin of conductance oscillations in an integrable cavity*, Physical Review B **94**, 195304 (2016).→
- [102] B. Szafran, *Scanning gate microscopy simulations for quantum rings: Effective potential of the tip and conductance maps*, Physical Review B **84**, 075336 (2011).→
- [103] T. Chwiej and B. Szafran, *Schrödinger-Poisson calculations for scanning gate microscopy of quantum rings based on etched two-dimensional electron gas*, Physical Review B **87**, 085302 (2013).→
- [104] E. Wach, D. P. Zebrowski, and B. Szafran, *Charge density mapping of strongly-correlated few-electron two-dimensional quantum dots by the scanning probe technique*, Journal of Physics: Condensed Matter **25**, 335801 (2013).→
- [105] K. Kolasinski and B. Szafran, *Wave-function description of conductance mapping for a quantum Hall electron interferometer*, Physical Review B **89**, 165306 (2014).→
- [106] K. Kolasinski, B. Szafran, and M. P. Nowak, *Imaging of double slit interference by scanning gate microscopy*, Physical Review B **90**, 165303 (2014).→
- [107] A. Mrenca-Kolasinska, S. Heun, and B. Szafran, *Aharonov-Bohm interferometer based on $n - p$ junctions in graphene nanoribbons*, Physical Review B **93**, 125411 (2016).→
- [108] K. Kolasinski, A. Mrenca-Kolasinska, and B. Szafran, *Imaging snake orbits at graphene $n-p$ junctions*, arXiv:1610.07566, 2016.→
- [109] M. D. Petrović, F. M. Peeters, A. Chaves, and G. A. Farias, *Conductance maps of quantum rings due to a local potential perturbation*, Journal of Physics: Condensed Matter **25**, 495301 (2013).→
- [110] M. D. Petrović, S. P. Milovanović, and F. M. Peeters, *Scanning gate microscopy of magnetic focusing in graphene devices: quantum versus classical simulation*, Nanotechnology **28**, 185202 (2017).→
- [111] J. Rychen, T. Ihn, P. Studerus, A. Herrmann, and K. Ensslin, *A low-temperature dynamic mode scanning force microscope operating in high magnetic fields*, Review of Scientific Instruments **70**, 2765 (1999).→
- [112] T. Vancura, S. Kicin, T. Ihn, K. Ensslin, M. Bichler, and W. Wegscheider, *Kelvin probe spectroscopy of a two-dimensional electron gas below 300 mK*, Applied Physics Letters **83**, 2602-2604 (2003).→
- [113] C. Schönberger and S. F. Alvarado, *Observation of single charge carriers by force microscopy*, Physical Review Letters **65**, 3162-3164 (1990).→

-
- [114] L. Cockins, Y. Miyahara, S. D. Bennett, A. A. Clerk, S. Studenikin, P. Poole, A. Sachrajda, and P. Grutter, *Energy levels of few-electron quantum dots imaged and characterized by atomic force microscopy*, Proceedings of the National Academy of Sciences **107**, 9496–9501 (2010).→
- [115] S. H. Tessmer, P. I. Glicofridis, R. C. Ashoori, L. S. Levitov, and M. R. Melloch, *Subsurface charge accumulation imaging of a quantum Hall liquid*, Nature **392**, 51–54 (1998).→
- [116] G. Finkelstein, P. I. Glicofridis, R. C. Ashoori, and M. Shayegan, *Topographic Mapping of the Quantum Hall Liquid Using a Few-Electron Bubble*, Science **289**, 90–94 (2000).→
- [117] P. I. Glicofridis, G. Finkelstein, R. C. Ashoori, and M. Shayegan, *Determination of the resistance across incompressible strips through imaging of charge motion*, Physical Review B **65**, 121312 (2002).→
- [118] G. A. Steele, R. C. Ashoori, L. N. Pfeiffer, and K. W. West, *Imaging Transport Resonances in the Quantum Hall Effect*, Physical Review Letters **95**, 136804 (2005).→
- [119] S. Chakraborty, I. J. Maasilta, S. H. Tessmer, and M. R. Melloch, *Imaging a two-dimensional electron system with a scanning charged probe*, Physical Review B **69**, 073308 (2004).→
- [120] I. Kuljanishvili, C. Kayis, J. F. Harrison, C. Piermarocchi, T. A. Kaplan, S. H. Tessmer, L. N. Pfeiffer, and K. W. West, *Scanning-probe spectroscopy of semiconductor donor molecules*, Nature Physics **4**, 227–233 (2008).→
- [121] M. Gasseller, M. DeNinno, R. Loo, J. F. Harrison, M. Caymax, S. Rogge, and S. H. Tessmer, *Single-Electron Capacitance Spectroscopy of Individual Dopants in Silicon*, Nano Letters **11**, 5208–5212 (2011).→
- [122] A. Baumgartner, M. E. Suddards, and C. J. Mellor, *Low-temperature and high magnetic field dynamic scanning capacitance microscope*, Review of Scientific Instruments **80**, 013704 (2009).→
- [123] M. E. Suddards, A. Baumgartner, M. Henini, and C. J. Mellor, *Scanning capacitance imaging of compressible and incompressible quantum Hall effect edge strips*, New Journal of Physics **14**, 083015 (2012).→
- [124] M. J. Yoo, T. A. Fulton, H. F. Hess, R. L. Willett, L. N. Dunkleberger, R. J. Chichester, L. N. Pfeiffer, and K. W. West, *Scanning Single-Electron Transistor Microscopy: Imaging Individual Charges*, Science **276**, 579–582 (1997).→
- [125] N. B. Zhitenev, T. A. Fulton, A. Yacoby, H. F. Hess, L. N. Pfeiffer, and K. W. West, *Imaging of localized electronic states in the quantum Hall regime*, Nature **404**, 473–476 (2000).→

Bibliography

- [126] S. Ilani, J. Martin, E. Teitelbaum, J. H. Smet, D. Mahalu, V. Umansky, and A. Yacoby, *The microscopic nature of localization in the quantum Hall effect*, Nature **427**, 328–332 (2004).→
- [127] J. Martin, S. Ilani, B. Verdene, J. Smet, V. Umansky, D. Mahalu, D. Schuh, G. Abstreiter, and A. Yacoby, *Localization of Fractionally Charged Quasi-Particles*, Science **305**, 980–983 (2004).→
- [128] J. Martin, N. Akerman, G. Ulbricht, T. Lohmann, J. H. Smet, K. von Klitzing, and A. Yacoby, *Observation of electron–hole puddles in graphene using a scanning single-electron transistor*, Nature Physics **4**, 144–148 (2008).→
- [129] J. Martin, N. Akerman, G. Ulbricht, T. Lohmann, K. von Klitzing, J. H. Smet, and A. Yacoby, *The nature of localization in graphene under quantum Hall conditions*, Nature Physics **5**, 669–674 (2009).→
- [130] F. Stern, *Polarizability of a Two-Dimensional Electron Gas*, Physical Review Letters **18**, 546–548 (1967).→
- [131] A. D. Karsono and D. R. Tilley, *Electron gas in one and two dimensions*, Journal of Physics C: Solid State Physics **10**, 2123–2129 (1977).→
- [132] M. R. Krcmar and W. M. Saslow, *Model for electrostatic screening by a semiconductor with free surface carriers*, Physical Review B **66**, 235310 (2002).→
- [133] S. Belaidi, P. Girard, and G. Leveque, *Electrostatic forces acting on the tip in atomic force microscopy: Modelization and comparison with analytic expressions*, Journal of Applied Physics **81**, 1023–1030 (1997).→
- [134] Y. Oyama, Y. Majima, and M. Iwamoto, *Analysis of scanning probe used for simultaneous measurement of tunneling current and surface potential*, Journal of Applied Physics **86**, 7087–7093 (1999).→
- [135] S. Hudlet, M. S. Jean, C. Guthmann, and J. Berger, *Evaluation of the capacitive force between an atomic force microscopy tip and a metallic surface*, The European Physical Journal B **2**, 5–10 (1998).→
- [136] H. Sim, M. Kataoka, and C. Ford, *Electron interactions in an antidot in the integer quantum Hall regime*, Physics Reports **456**, 127–165 (2008).→
- [137] M. Kataoka, C. J. B. Ford, G. Faini, D. Mailly, M. Y. Simmons, D. R. Mace, C.-T. Liang, and D. A. Ritchie, *Detection of Coulomb Charging around an Antidot in the Quantum Hall Regime*, Phys. Rev. Lett. **83**, 160–163 (1999).→
- [138] B. Rosenow and B. I. Halperin, *Influence of interactions on flux and back-gate period of quantum Hall interferometers*, Physical Review Letters **98**, 106801 (2007).→

-
- [139] K. J. Thomas, J. T. Nicholls, M. Y. Simmons, M. Pepper, D. R. Mace, and D. A. Ritchie, *Possible Spin Polarization in a One-Dimensional Electron Gas*, Phys. Rev. Lett. **77**, 135–138 (1996).→
- [140] S. M. Cronenwett, H. J. Lynch, D. Goldhaber-Gordon, L. P. Kouwenhoven, C. M. Marcus, K. Hirose, N. S. Wingreen, and V. Umansky, *Low-Temperature Fate of the 0.7 Structure in a Point Contact: A Kondo-like Correlated State in an Open System*, Phys. Rev. Lett. **88**, 226805 (2002).→
- [141] L. P. Kouwenhoven, C. M. Marcus, P. L. McEuen, S. Tarucha, R. M. Westervelt, and N. S. Wingreen, *Electron Transport in Quantum Dots*, Mesoscopic Electron Transport, Springer Netherlands, 1997, pp. 105–214.→
- [142] J. J. Heremans, S. von Molnár, D. D. Awschalom, and A. C. Gossard, *Ballistic electron focusing by elliptic reflecting barriers*, Applied Physics Letters **74**, 1281–1283 (1999).→
- [143] I. Neder, N. Ofek, Y. Chung, M. Heiblum, D. Mahalu, and V. Umansky, *Interference between two indistinguishable electrons from independent sources*, Nature **448**, 333–337 (2007).→
- [144] P. Roulleau, F. Portier, P. Roche, A. Cavanna, G. Faini, U. Gennser, and D. Mailly, *Direct Measurement of the Coherence Length of Edge States in the Integer Quantum Hall Regime*, Phys. Rev. Lett. **100**, 126802 (2008).→
- [145] R. Danneau, O. Klochan, W. R. Clarke, L. H. Ho, A. P. Micolich, M. Y. Simmons, A. R. Hamilton, M. Pepper, and D. A. Ritchie, *0.7 Structure and Zero Bias Anomaly in Ballistic Hole Quantum Wires*, Phys. Rev. Lett. **100**, 016403 (2008).→
- [146] W. K. Hew, K. J. Thomas, M. Pepper, I. Farrer, D. Anderson, G. A. C. Jones, and D. A. Ritchie, *Spin-Incoherent Transport in Quantum Wires*, Phys. Rev. Lett. **101**, 036801 (2008).→
- [147] A. Kristensen, H. Bruus, A. E. Hansen, J. B. Jensen, P. E. Lindelof, C. J. Marckmann, J. Nygård, C. B. Sørensen, F. Beuscher, A. Forchel, and M. Michel, *Bias and temperature dependence of the 0.7 conductance anomaly in quantum point contacts*, Phys. Rev. B **62**, 10950–10957 (2000).→
- [148] D. J. Reilly, G. R. Facer, A. S. Dzurak, B. E. Kane, R. G. Clark, P. J. Stiles, R. G. Clark, A. R. Hamilton, J. L. O’Brien, N. E. Lumpkin, L. N. Pfeiffer, and K. W. West, *Many-body spin-related phenomena in ultra low-disorder quantum wires*, Phys. Rev. B **63**, 121311 (2001).→
- [149] P. Roche, J. Ségala, D. C. Glattli, J. T. Nicholls, M. Pepper, A. C. Graham, K. J. Thomas, M. Y. Simmons, and D. A. Ritchie, *Fano Factor Reduction on the 0.7 Conductance Structure of a Ballistic One-Dimensional Wire*, Phys. Rev. Lett. **93**, 116602 (2004).→

Bibliography

- [150] F. Sfigakis, C. J. B. Ford, M. Pepper, M. Kataoka, D. A. Ritchie, and M. Y. Simmons, *Kondo Effect from a Tunable Bound State within a Quantum Wire*, Phys. Rev. Lett. **100**, 026807 (2008).→
- [151] L. W. Smith, A. R. Hamilton, K. J. Thomas, M. Pepper, I. Farrer, J. P. Griffiths, G. A. C. Jones, and D. A. Ritchie, *Compressibility Measurements of Quasi-One-Dimensional Quantum Wires*, Phys. Rev. Lett. **107**, 126801 (2011).→
- [152] R. Fitzgerald, *Quantum Point Contact Mysteries Reexamined*, Physics Today **55**, 21–23 (2002).→
- [153] K. A. Matveev, *Conductance of a Quantum Wire in the Wigner-Crystal Regime*, Phys. Rev. Lett. **92**, 106801 (2004).→
- [154] Y. Meir, K. Hirose, and N. S. Wingreen, *Kondo Model for the 0.7 Anomaly in Transport through a Quantum Point Contact*, Phys. Rev. Lett. **89**, 196802 (2002).→
- [155] D. J. Reilly, *Phenomenological model for the 0.7 conductance feature in quantum wires*, Phys. Rev. B **72**, 033309 (2005).→
- [156] D. Schmeltzer, A. Saxena, A. R. Bishop, and D. L. Smith, *Electron transmission through a short interacting wire: 0.7 conductance anomaly*, Phys. Rev. B **71**, 045429 (2005).→
- [157] C. Sloggett, A. I. Milstein, and O. P. Sushkov, *Correlated electron current and temperature dependence of the conductance of a quantum point contact*, The European Physical Journal B **61**, 427–432 (2008).→
- [158] B. Spivak and F. Zhou, *Ferromagnetic correlations in quasi-one-dimensional conducting channels*, Phys. Rev. B **61**, 16730–16735 (2000).→
- [159] O. P. Sushkov, *Restricted and unrestricted Hartree-Fock calculations of conductance for a quantum point contact*, Phys. Rev. B **67**, 195318 (2003).→
- [160] A. P. Micolich, *What lurks below the last plateau: experimental studies of the $0.7 \times 2e^2/h$ conductance anomaly in one-dimensional systems*, Journal of Physics: Condensed Matter **23**, 443201 (2011).→
- [161] A. D. Güçlü, C. J. Umrigar, H. Jiang, and H. U. Baranger, *Localization in an inhomogeneous quantum wire*, Phys. Rev. B **80**, 201302 (2009).→
- [162] D. Weinmann, R. A. Jalabert, A. Freyn, G.-L. Ingold, and J.-L. Pichard, *Detection of interaction-induced nonlocal effects using perfectly transmitting nanostructures*, The European Physical Journal B **66**, 239–244 (2008).→

-
- [163] N. Aoki, A. Burke, C. R. da Cunha, R. Akis, D. K. Ferry, and Y. Ochiai, *Study of quantum point contact via low temperature scanning gate microscopy*, Journal of Physics: Conference Series **38**, 79–82 (2006).→
- [164] M. N. Kiselev, K. Kikoin, and L. W. Molenkamp, *Resonance Kondo tunneling through a double quantum dot at finite bias*, Phys. Rev. B **68**, 155323 (2003).→
- [165] M. J. Iqbal, R. Levy, E. J. Koop, J. B. Dekker, J. P. de Jong, J. H. M. van der Velde, D. Reuter, A. D. Wieck, R. Aguado, Y. Meir, and C. H. van der Wal, *Odd and even Kondo effects from emergent localization in quantum point contacts*, Nature **501**, 79–83 (2013).→
- [166] M. Zaffalon, A. Bid, M. Heiblum, D. Mahalu, and V. Umansky, *Transmission Phase of a Singly Occupied Quantum Dot in the Kondo Regime*, Phys. Rev. Lett. **100**, 226601 (2008).→
- [167] S. Takada, C. Bäuerle, M. Yamamoto, K. Watanabe, S. Hermelin, T. Meunier, A. Alex, A. Weichselbaum, J. von Delft, A. Ludwig, D. Wieck, A. and S. Tarucha, *Transmission Phase in the Kondo Regime Revealed in a Two-Path Interferometer*, Phys. Rev. Lett. **113**, 126601 (2014).→
- [168] N. J. Appleyard, J. T. Nicholls, M. Pepper, W. R. Tribe, M. Y. Simmons, and D. A. Ritchie, *Direction-resolved transport and possible many-body effects in one-dimensional thermopower*, Phys. Rev. B **62**, R16275–R16278 (2000).→
- [169] B. J. van Wees, H. van Houten, C. W. J. Beenakker, J. G. Williamson, L. P. Kouwenhoven, D. van der Marel, and C. T. Foxon, *Quantized conductance of point contacts in a two-dimensional electron gas*, Phys. Rev. Lett. **60**, 848–850 (1988).→
- [170] T. Rejec and Y. Meir, *Magnetic impurity formation in quantum point contacts*, Nature **442**, 900–903 (2006).→
- [171] C.-K. Wang and K.-F. Berggren, *Local spin polarization in ballistic quantum point contacts*, Phys. Rev. B **57**, 4552–4556 (1998).→
- [172] F. Bauer, J. Heyder, E. Schubert, D. Borowsky, D. Taubert, B. Bruognolo, D. Schuh, W. Wegscheider, J. von Delft, and S. Ludwig, *Microscopic origin of the 0.7 anomaly in quantum point contacts*, Nature **501**, 73–78 (2013).→
- [173] J. M. Elzerman, R. Hanson, J. S. Greidanus, L. H. Willems van Beveren, S. De Franceschi, L. M. K. Vandersypen, S. Tarucha, and L. P. Kouwenhoven, *Few-electron quantum dot circuit with integrated charge read out*, Phys. Rev. B **67**, 161308 (2003).→

Bibliography

- [174] K. D. Petersson, C. G. Smith, D. Anderson, P. Atkinson, G. A. C. Jones, and D. A. Ritchie, *Charge and Spin State Readout of a Double Quantum Dot Coupled to a Resonator*, Nano Letters **10**, 2789–2793 (2010).→
- [175] R. D. Grober, J. Acimovic, J. Schuck, D. Hessman, P. J. Kindlemann, J. Hespanha, A. S. Morse, K. Karrai, I. Tiemann, and S. Manus, *Fundamental limits to force detection using quartz tuning forks*, Review of Scientific Instruments **71**, 2776–2780 (2000).→
- [176] F. J. Giessibl, *Atomic resolution on Si(111)-(7×7) by noncontact atomic force microscopy with a force sensor based on a quartz tuning fork*, Applied Physics Letters **76**, 1470–1472 (2000).→
- [177] E. Y. Andrei, G. Deville, D. C. Glattli, F. I. B. Williams, E. Paris, and B. Etienne, *Observation of a Magnetically Induced Wigner Solid*, Phys. Rev. Lett. **60**, 2765–2768 (1988).→
- [178] E. Wigner, *On the Interaction of Electrons in Metals*, Phys. Rev. **46**, 1002–1011 (1934).→
- [179] F. I. B. Williams, P. A. Wright, R. G. Clark, E. Y. Andrei, G. Deville, D. C. Glattli, O. Probst, B. Etienne, C. Dorin, C. T. Foxon, and J. J. Harris, *Conduction threshold and pinning frequency of magnetically induced Wigner solid*, Phys. Rev. Lett. **66**, 3285–3288 (1991).→
- [180] T.-M. Chen, M. Pepper, I. Farrer, G. A. C. Jones, and D. A. Ritchie, *All-Electrical Injection and Detection of a Spin-Polarized Current Using 1D Conductors*, Phys. Rev. Lett. **109**, 177202 (2012).→
- [181] R. M. Potok, J. A. Folk, C. M. Marcus, and V. Umansky, *Detecting Spin-Polarized Currents in Ballistic Nanostructures*, Phys. Rev. Lett. **89**, 266602 (2002).→
- [182] L. Kouwenhoven and L. Glazman, *Revival of the Kondo effect*, Physics World **14**, 33–38 (2001).→
- [183] S. M. Cronenwett, T. H. Oosterkamp, and L. P. Kouwenhoven, *A Tunable Kondo Effect in Quantum Dots*, Science **281**, 540–544 (1998).→
- [184] D. Goldhaber-Gordon, H. Shtrikman, D. Mahalu, D. Abusch-Magder, U. Meirav, and M. A. Kastner, *Kondo effect in a single-electron transistor*, Nature **391**, 156–159 (1998).→
- [185] M. Pustilnik and L. Glazman, *Kondo effect in quantum dots*, Journal of Physics: Condensed Matter **16**, R513 (2004).→

-
- [186] E. S. Sørensen and I. Affleck, *Scaling theory of the Kondo screening cloud*, Phys. Rev. B **53**, 9153–9167 (1996).→
- [187] I. Affleck, *The Kondo screening cloud: what it is and how to observe it*, arXiv:0911.2209 (2009).→
- [188] I. V. Borzenets, J. Shim, J. C. H. Chen, A. Ludwig, A. D. Wieck, S. Tarucha, H.-S. Sim, and M. Yamamoto, *Observation of the Kondo screening cloud*, Nature **579**, 210–213 (2020).→
- [189] P. Coleman, *Heavy Fermions and the Kondo Lattice: a 21st Century Perspective*, arXiv:1509.05769 (2015).→
- [190] S.-S. B. Lee, J. Park, and H.-S. Sim, *Macroscopic Quantum Entanglement of a Kondo Cloud at Finite Temperature*, Phys. Rev. Lett. **114**, 057203 (2015).→
- [191] P. Sodano, A. Bayat, and S. Bose, *Kondo cloud mediated long-range entanglement after local quench in a spin chain*, Phys. Rev. B **81**, 100412 (2010).→
- [192] G. Nicolí, M. S. Ferguson, C. RöSSLer, A. Wolfertz, G. Blatter, T. Ihn, K. Ensslin, C. Reichl, W. Wegscheider, and O. Zilberberg, *Cavity-Mediated Coherent Coupling between Distant Quantum Dots*, Phys. Rev. Lett. **120**, 236801 (2018).→
- [193] H. C. Manoharan, C. P. Lutz, and D. M. Eigler, *Quantum mirages formed by coherent projection of electronic structure*, Nature **403**, 512–515 (2000).→
- [194] H. Prüser, M. Wenderoth, P. E. Dargel, A. Weismann, R. Peters, T. Pruschke, and R. G. Ulbrich, *Long-range Kondo signature of a single magnetic impurity*, Nature Physics **7**, 203–206 (2011).→
- [195] P. Simon and I. Affleck, *Finite-Size Effects in Conductance Measurements on Quantum Dots*, Phys. Rev. Lett. **89**, 206602 (2002).→
- [196] J. Park, S.-S. B. Lee, Y. Oreg, and H.-S. Sim, *How to Directly Measure a Kondo Cloud’s Length*, Phys. Rev. Lett. **110**, 246603 (2013).→
- [197] C. RöSSLer, D. Oehri, O. Zilberberg, G. Blatter, M. Karalic, J. Pijenburg, A. Hofmann, T. Ihn, K. Ensslin, C. Reichl, and W. Wegscheider, *Transport Spectroscopy of a Spin-Coherent Dot-Cavity System*, Phys. Rev. Lett. **115**, 166603 (2015).→
- [198] P. Simon, J. Salomez, and D. Feinberg, *Transport spectroscopy of a Kondo quantum dot coupled to a finite size grain*, Phys. Rev. B **73**, 205325 (2006).→
- [199] N. J. Craig, J. M. Taylor, E. A. Lester, C. M. Marcus, M. P. Hanson, and A. C. Gossard, *Tunable Nonlocal Spin Control in a Coupled-Quantum Dot System*, Science **304**, 565–567 (2004).→

Bibliography

- [200] M. G. Vavilov and L. I. Glazman, *Transport Spectroscopy of Kondo Quantum Dots Coupled by RKKY Interaction*, Phys. Rev. Lett. **94**, 086805 (2005).→
- [201] A. Bayat, P. Sodano, and S. Bose, *Negativity as the entanglement measure to probe the Kondo regime in the spin-chain Kondo model*, Phys. Rev. B **81**, 064429 (2010).→
- [202] A. C. Johnson, J. R. Petta, C. M. Marcus, M. P. Hanson, and A. C. Gossard, *Singlet-triplet spin blockade and charge sensing in a few-electron double quantum dot*, Phys. Rev. B **72**, 165308 (2005).→
- [203] H. Bluhm, S. Foletti, I. Neder, M. Rudner, D. Mahalu, V. Umansky, and A. Yacoby, *Dephasing time of GaAs electron-spin qubits coupled to a nuclear bath exceeding 200 μ s*, Nature Physics **7**, 109–113 (2011).→
- [204] D. Goldhaber-Gordon, J. Göres, M. A. Kastner, H. Shtrikman, D. Mahalu, and U. Meirav, *From the Kondo Regime to the Mixed-Valence Regime in a Single-Electron Transistor*, Phys. Rev. Lett. **81**, 5225–5228 (1998).→
- [205] S. Hershfield, J. H. Davies, and J. W. Wilkins, *Probing the Kondo resonance by resonant tunneling through an Anderson impurity*, Phys. Rev. Lett. **67**, 3720–3723 (1991).→
- [206] Y. Meir, N. S. Wingreen, and P. A. Lee, *Low-temperature transport through a quantum dot: The Anderson model out of equilibrium*, Phys. Rev. Lett. **70**, 2601–2604 (1993).→
- [207] S. Florens and I. Snyman, *Universal spatial correlations in the anisotropic Kondo screening cloud: Analytical insights and numerically exact results from a coherent state expansion*, Phys. Rev. B **92**, 195106 (2015).→
- [208] T. Hand, J. Kroha, and H. Monien, *Spin Correlations and Finite-Size Effects in the One-Dimensional Kondo Box*, Phys. Rev. Lett. **97**, 136604 (2006).→
- [209] R. K. Kaul, G. Zaránd, S. Chandrasekharan, D. Ullmo, and H. U. Baranger, *Spectroscopy of the Kondo Problem in a Box*, Phys. Rev. Lett. **96**, 176802 (2006).→
- [210] H. Jeong, A. M. Chang, and M. R. Melloch, *The Kondo Effect in an Artificial Quantum Dot Molecule*, Science **293**, 2221–2223 (2001).→
- [211] J. C. Chen, A. M. Chang, and M. R. Melloch, *Transition between Quantum States in a Parallel-Coupled Double Quantum Dot*, Phys. Rev. Lett. **92**, 176801 (2004).→
- [212] A. Georges and Y. Meir, *Electronic Correlations in Transport through Coupled Quantum Dots*, Phys. Rev. Lett. **82**, 3508–3511 (1999).→

-
- [213] R. López, R. Aguado, and G. Platero, *Nonequilibrium Transport through Double Quantum Dots: Kondo Effect versus Antiferromagnetic Coupling*, Phys. Rev. Lett. **89**, 136802 (2002).→
- [214] P. Simon, *Kondo screening cloud in a double quantum dot system*, Phys. Rev. B **71**, 155319 (2005).→
- [215] L. C. Ribeiro, I. J. Hamad, G. Chiappe, and E. V. Anda, *Transport across two interacting quantum dots: Bulk Kondo, Kondo box, and molecular regimes*, Phys. Rev. B **89**, 045412 (2014).→
- [216] M. D. Shulman, O. E. Dial, S. P. Harvey, H. Bluhm, V. Umansky, and A. Yacoby, *Demonstration of Entanglement of Electrostatically Coupled Singlet-Triplet Qubits*, Science **336**, 202–205 (2012).→
- [217] R. Maurand, X. Jehl, D. Kotekar-Patil, A. Corna, H. Bohuslavskyi, R. Laviéville, L. Hutin, S. Barraud, M. Vinet, M. Sanquer, and S. D. Franceschi, *A CMOS silicon spin qubit*, Nature Communications **7**, 13575 (2016).→
- [218] A. Crippa, R. Maurand, D. Kotekar-Patil, A. Corna, H. Bohuslavskyi, A. O. Orlov, P. Fay, R. Laviéville, S. Barraud, M. Vinet, M. Sanquer, S. D. Franceschi, and X. Jehl, *Level Spectrum and Charge Relaxation in a Silicon Double Quantum Dot Probed by Dual-Gate Reflectometry*, Nano Letters **17**, 1001–1006 (2017).→
- [219] B. Lechtenberg and F. B. Anders, *Spatial and temporal propagation of Kondo correlations*, Phys. Rev. B **90**, 045117 (2014).→
- [220] M. Nuss, M. Ganahl, E. Arrigoni, W. von der Linden, and H. G. Evertz, *Nonequilibrium spatiotemporal formation of the Kondo screening cloud on a lattice*, Phys. Rev. B **91**, 085127 (2015).→